공학박사학위논문

수직 이착륙기 고정확도 유동 해석과 효율적인 설계를 위한 수치 기법 개발 및 적용

Accurate and Efficient High-Order Spatial Scheme for Rotorcraft Flow Analysis

2023 년 2 월

서울대학교 대학원

항공우주공학과

홍 윤 표

수직 이착륙기 고정확도 유동 해석과 효율적인 설계를 위한 수치 기법 개발 및 적용

Accurate and Efficient High-Order Spatial Scheme for Rotorcraft Flow Analysis

지도교수 이 관 중

이 논문을 공학박사 학위논문으로 제출함

2022 년 11 월

서울대학교 대학원

항공우주공학과

홍 윤 표

홍윤표의 공학박사 학위논문을 인준함

2022 년 12 월

위 원 장 : 김 규 홍

부위원장 : 이 관 중

위 원 : 박 수 형

위 원 : 박 동 훈

위 원 : 강 희 정

This dissertation contains contents of
the following journal publications and conference papers:

[1] Hong, Y., Lee, D., Yee, K., and Park, S. H. "Enhanced High-Order Scheme for High-Resolution Rotorcraft Flowfield Analysis." *AIAA Journal*, Vol. 60, No. 1, 2022, pp. 144–159. https://doi.org/10.2514/1.J060803.

[2] Hong, Y., Park, S. H., and Yee, K. "Comparative Assessment of Local Accuracy of High-Order Spatial Schemes for Rotorcraft Aeroacoustics." *AIAA Journal*, Vol. 61, No. 1, 2023, pp. 355–377. https://doi.org/10.2514/1.J062008.

[3] Hong, Y., Lee, D., Yang, S., and Yee, K. "Numerical Investigation and Design Exploration on Aerodynamic Performance for Stacked Rotor." 48th European Rotorcraft Forum, Swiss, Winterthur, Oct. 2022.

To view the author's profile, please visit

https://sites.google.com/view/flyoon/home

Thesis Advisory Committee

Kwanjung Yee, Ph. D. *Advisor*	Department of Aerospace Engineering, Seoul National University
Kyu Hong Kim, Ph. D. *Chair*	Department of Aerospace Engineering, Seoul National University
Soo Hyung Park, Ph. D.	Department of Mechanical and Aerospace Engineering, Konkuk University
Donghun Park, Ph. D.	Department of Aerospace Engineering, Pusan National University
Hee Jung Kang, Ph. D.	UAM Research Division, Korea Aerospace Research Institute

Abstract

Accurate and Efficient High-Order Spatial Scheme for Rotorcraft Flow Analysis

Yoonpyo Hong
Department of Aerospace Engineering
The Graduate School
Seoul National University

As a growing number of next-generation rotorcraft are being newly developed for urban air mobility these days, demands for accurate aerodynamic and aeroacoustic performance analysis of the new configurations are increasing. Higher-fidelity analyses require advanced numerical techniques, among which high-order accurate spatial discretization schemes are the most critical. Several concepts of spatial schemes previously presented have been applied for a relatively simple type of helicopter performance analysis and have produced satisfactory results when a large number of grids are involved. However, since the newly developed rotorcraft commonly adopt multiple propulsors which require a grid level several times higher

than the grid level used for single helicopter analysis, the accuracy of the spatial discretization method must be enhanced. In addition, it is necessary to determine which numerical characteristics are essential to the accurate analysis of the rotorcraft flowfield. The doctoral research was initiated in light of the aforementioned background, and the core results are as follows.

First, an improved high-order accurate spatial discretization scheme, eMLP-VC, was developed based on the characteristics of the rotorcraft flow field, such as vortex-dominated, subsonic to supersonic flow speed, and highly unsteady. The accuracy, robustness, and efficiency were improved compared to the baseline scheme, eMLP. Through one- and two-dimensional benchmark tests, eMLP-VC was demonstrated to be superior, specifically in vortex-dominated and compressible flow fields. Moreover, eMLP-VC can maintain its robustness in the hypersonic flow dominated by strong shock waves.

Second, a local-order-of-accuracy index (LAI) was suggested which allows quantitative comparison between the developed eMLP-VC and conventional high-order accurate spatial discretization schemes. High-order accurate spatial discretization schemes used in compressible flows usually produce reduced accuracies locally in the continuous flow because of the shock-sensing algorithm. As the local reduction in accuracy in the discretized domain reduces the fidelity of the flow solver, it is necessary to quantify the amount of accuracy reduction and investigate the numerical techniques that minimize the decrease in accuracy. The LAI newly suggested in this thesis can show the region where the order-of-accuracy

decreases, and it can be applied to any type of spatial discretization method that uses explicit reconstruction. Several high-order accurate spatial discretization schemes, including the one presented in this thesis, were compared through the LAI analyses in the one- and two-dimensional benchmark tests. Two numerical characteristics essential for high-fidelity rotorcraft aerodynamic analysis could be identified: advanced shock-sensing algorithm and hybrid central-upwind characteristics.

Third, eMLP-VC was applied to actual three-dimensional complicated flow field analysis of rotorcraft. Even with a coarse grid system, the unsteady vortex dynamics of PROWIM model and the HART-II rotor can be captured. In particular, the aeroacoustic noise generated by blade-vortex interaction in HART-II rotor could be predicted with high accuracy. Design exploration and optimization of co-rotating coaxial rotor, applicable to the urban air mobility aircraft, were also conducted using the high-fidelity solver with eMLP-VC. It has been demonstrated that eMLP-VC can be sufficiently useful for the development of a new type of next-generation rotorcraft.

Keywords: High-Order Spatial Discretization Scheme, Local-order-of-accuracy index, Vertical Take-Off and Landing aircraft, Rotorcraft, Urban Air Mobility, Aerodynamic interaction, Aeroacoustics, Design Exploration, Design Optimization

Student Number: 2019-31839

Table of Contents

Abstract I

Table of Contents IV

Nomenclature VII

List of Figures XIII

List of Tables XVI

Chapter 1. Introduction 1

1.1 Recent developments of newly designed UAM aircraft 1

1.2 Numerical characteristics of rotorcraft flowfield 5

1.3 Overview of high-order spatial discretization schemes 6

1.4 Research Questions 10

1.4.1 Question 1: Is it possible to accurately predict the aerodynamic and noise performance of UAM eVTOL aircraft with the schemes that have been developed so far? 10

1.4.2 Question 2: What characteristics of the scheme will allow accurate prediction of the rotorcraft flow field? / Is there a standard for evaluating schemes that use different types of concepts? 11

1.5 Objective of the dissertation 12

Chapter 2. Numerical Approach for Rotorcraft Performance Analysis 14

2.1 Brief Review of Rotorcraft Aerodynamic Solvers 14

2.1.1 Reynolds-Averaged Navier-Stokes Equations 16

2.1.2 Turbulent Equations 18

2.2 Spatial Discretization Methods 20

2.2.1 Reconstruction Methods 20

2.2.2 Flux Functions for convective fluxes 21

2.3 Temporal Integration Methods 22

Chapter 3. Development of Advanced Spatial Discretization Scheme for High-Resolution Rotorcraft Flowfield..24

3.1 Review of eMLP scheme..24

3.1.1 Flow Distinguishing Step 25

3.1.2 Higher-order Interpolation..27

3.2 Modifications of eMLP scheme (eMLP-VC) 30

3.2.1 Accuracy Enhancements 30

3.2.2 Robustness Enhancement 36

3.3 Advanced performance of eMLP-VC..39

3.3.1 Linear wave propagation problem..40

3.3.2 Nonlinear wave propagation problem 44

3.3.3 Double Mach Reflection..47

Chapter 4. Comparative Assessment of High-Order Spatial Schemes in Terms of Local Accuracy..50

4.1 Computational costs of high-order spatial schemes..53

4.2 Analysis of Local truncation error 54

4.2.1 Local truncation error analysis using taylor series expansion 54

4.2.2 Local-Order-of-Accuracy Index (LAI)..59

4.3 Assessment of high-order spatial schemes through benchmark tests 62

4.3.1 1D Sine Wave Advection 64

4.3.2 1D Gaussian Pulse Advection 68

4.3.3 2D Acoustic Pulse Propagation 72

4.3.4 2D Isentropic Vortex Advection..77

4.4 Main characteristics essential for high-resolution rotorcraft flowfield.....84
Chapter 5. Applications: Numerical Investigation and Design Exploration of Rotorcraft.....86
5.1 Propeller-Wing Interaction (PROWIM).....87
5.2 Numerical investigation: Descent flight (BVI, HART-II).....98
5.2.1 CFD-CSD Loose Coupling.....98
5.2.2 Acoustic Analogy.....102
5.2.3 Aerodynamic Results.....102
5.2.4 Aeroacoustic Results.....112
5.3 Design exploration of co-rotating coaxial rotor.....118
5.3.1 Design Problem.....119
5.3.2 Overall Results.....121
5.3.3 Underlying Physics.....124
5.3.4 Detail analysis of best DOE configuration.....133
Chapter 6. Conclusions.....137
6.1 Summary and originality of the thesis.....137
6.2 Recommendations for the future work.....142
Appendix.....146
A. Concepts of WENO-type schemes.....146
B. Global-order-of-accuracy of spatial schemes on benchmark tests.....150
References.....157
국문 초록.....167

Nomenclature

English Symbols

a	function of Mach number in low Mach number adjustment
a_{SCL}	advection velocity for scalar conservation equation
b^r	r^{th}-order local polynomial
	in $(2r-1)^{th}$-order WENO-type scheme
$\boldsymbol{c}$	weight vector of stencil
C_M	pitching moment coefficient
C_N	normal force coefficient
$C_{P,sec}$	sectional pressure coefficient
C_P	power coefficient
C_T	thrust coefficient
d	distinguishing function
d_1	distance from propeller front (PROWIM)
d_2	distance from wing trailing edge (PROWIM)
D	blade diameter
e	total energy
$\boldsymbol{e_i}$	i^{th}-order truncation error coefficients
$\bar{F}, \bar{G}, \bar{H}$	convective flux vectors in $x, y,$ and z directions
$\bar{F}_v, \bar{G}_v, \bar{H}_v$	viscous flux vectors in $x, y,$ and z directions
h	grid spacing of double Mach reflection problem
H	enthalpy
k	turbulent kinetic energy
k_{tc}	thermal conductivity
l_i	polynomial constant
M	Mach number
$\bar{M}^{\pm}_{L,R}$	split Mach number in AUSMPW+ flux scheme

p	pressure
$\bar{P}_{L,R}^{\pm}$	split pressure in AUSMPW+ flux scheme
Pr	Prandtl number
q	cell quantity
$\bar{q}$	cell-averaged quantity
q_0	initial condition for benchmark tests
Q	vortex identification method
$\bar{Q}$	conservative variable vector
r_{TVD}	local smoothness measure function in TVD
r_v	distance from vortex core
R	radius of propeller and rotor
$\bar{R}$	residual term
R_{ij}	Reynolds-stress
Re	Reynolds number
s^r	coefficients in $(2r-1)^{th}$-order WENO-type scheme
t	nondimensional time
T	Temperature
u, v, w	velocity components in $x, y,$ and z directions
u_i', u_j'	fluctuating part of velocity
$\overline{u_i}, \overline{u_j}$	mean part of velocity
$u_{\theta,0}$	initial tangential velocity
$u_{r,0}$	initial radial velocity
w^r	local polynomial weight
	in $(2r-1)^{th}$-order WENO-type scheme
x, y, z	Cartesian coordinates

Greek Symbols

α	coefficient for multidimensional limiting process

α_{wing}	wing incident angle
α^r	coefficients in $(2r-1)^{th}$-order WENO-type scheme
α_{eff}	effective angle of attack
β	parameter for higher-order interpolation
β_v	vortex strength
β^r	smoothness indicator of local polynomial in $(2r-1)^{th}$-order WENO-type scheme
γ	ratio of specific heats
γ_v	gas constant
γ^r	ideal weight in $(2r-1)^{th}$-order WENO-type scheme
Γ_i	normalizing constant for i^{th}-order error measure
Γ^*	vorticity magnitude normalized by initial vorticity magnitude
Γ^{**}	vorticity magnitude normalized by eMLP-VC value
$\delta\theta$	pitch angle difference
δz	vertical spacing
$\delta\phi$	index angle
$\Delta\tau$	pseudo time step
Δt	physical time step
Δx	grid point spacing
ϵ	small positive number
θ_0	collective pitch angle
θ_{1c}	lateral cyclic pitch angle
θ_{1s}	longitudinal cyclic pitch angle
λ	thermal conductivity
μ	dynamic viscosity
μ_T	turbulent eddy viscosity
ρ	density
τ	molecular stress tensor

τ_{2r-1}	global smoothness indicator
	in $(2r-1)^{th}$-order WENO-type scheme
ϕ	limiting function
Φ	Primitive value
ψ	azimuth angle
$\mathbf{\Psi}$	conservative variable vector in AUSMPW+ scheme
ω	specific dissipation rate
Ω_R	the normalized Rortex

Subscripts

LM	low-Mach-number adjustment
approximate	sensing function
sup	total variation diminishing superbee reconstruction
L,*R*	left and right state
$\frac{1}{2}$	cell interface
∞	freestream quantity
0	initial condition

Superscripts

T	transpose

Abbreviations

ADR	Approximate-Dispersion-Relation
AIAA	American Institute of Aeronautics and Astronautics
BDF	Backward Difference Formula
BET	Blade Element Theory
BVI	Blade-Vortex Interaction
CAMRAD II	Comprehensive Analytical Model of

	Rotorcraft Aerodynamics and Dynamics II
CFD	Computational Fluid Dynamics
CFL	Courant-Friedrichs-Lewy
CSD	Computational Structural Dynamics
DADI	Diagonalized Alternating Direction Implicit
DIRK	Diagonally Implicit Runge-Kutta
DNS	Direct Numerical Simulation
DOE	Design Of Experiment
DDES	Delayed Detached Eddy Simulation
DRP	Dispersion-Relation-Preserving
eVTOL	electric Vertical Take-Off and Landing
eMLP	enhanced Multi-dimensional Limiting Process
eMLP-VC	enhanced Multi-dimensional Limiting Process for Vorticity Conservation
FVM	Finite-Volume Method
FW-H	Ffowcs Williams and Hawkings
FoS	Function of Smoothness
HART-II	Second higher-Harmonic control Aeroacoustic Rotor Test
HLPW	High Lift Prediction Workshop
IRK	Implicit Runge-Kutta
KARI	Korea Aerospace Research Institute
KR-Noise	Korea Aerospace Research Institute Rotor-Noise
LAI	Local-order-of-Accuracy Index
LES	Large-Eddy Simulation
MLP	Multi-dimensional Limiting Process
MUSCL	Monotone Upstream-centered Scheme for Conservation Law
NS	Navier-Stokes
OPPAV	Optionally Piloted Personal Air Vehicle

PROWIM	PROpeller-Wing Interaction Model
RANS	Reynolds-Averaged Navier-Stokes
SA	Spalart-Allmaras
SPL	Sound Pressure Level
TVB	Total Variation Bounded
TVD	Total-Variation Diminishing
TRAM	TiltRotor Aeroacoustic Model
UAM	Urban Air Mobility
URANS	Unsteady Reynolds-Averaged Navier-Stokes
WMLES	Wall-Modeled Large-Eddy Simulation
WENO	Weighted Essentially Non-Oscillatory
1D	One-Dimensional
2D	Two-Dimensional
3D	Three-Dimensional

List of Figures

Fig. 1.1 Various concepts of UAM aircraft [2] (a. wingless, b. lift+cruise, c-d. vectored thrust) 3
Fig. 3.1 Isentropic vortex model's profile and gradient distribution 32
Fig. 3.2 Comparison of results of original/modified distinguishing mechanism and density contour 34
Fig. 3.3 Pressure distribution of cell surface $y = z = 0.725$. 38
Fig. 3.4 Linear wave propagation problem calculation results at $t = 1$. 41
Fig. 3.5 L_2 norm of error of calculation results at $t = 1$. 42
Fig. 3.6 Comparison of density contour (Up: Coarse Grids, Down: Fine grids) 45
Fig. 3.7 Comparison of density contour and numerical schlieren for double Mach reflection problem $h = 1512$, $t = 0.2$. 49
Fig. 4.1 Physical distribution and cell-centered quantities. 56
Fig. 4.2 Results of low amplitude sine wave advection problem. 65
Fig. 4.3 Results of high amplitude sine wave advection problem. 67
Fig. 4.4 Results of gaussian pulse advection problem (subsonic, M=0.1). 69
Fig. 4.5 Results of gaussian pulse advection problem (supersonic, M=1.0). 71
Fig. 4.6 Pressure contours and physical quantity distributions of the 2D acoustic pulse test (Grids = [161×161], eMLP-VC). 72
Fig. 4.7 Gaussian acoustic pulse test results {a) pressure distribution, b) u-velocity distribution} 73
Fig. 4.8 LAI contours of five different schemes (Non-dimensionalized time, $t = 1.0$, LAI of pressure quantity). 75
Fig. 4.9 Gaussian acoustic pulse test results with different grid resolutions using WENO-Z scheme. 76
Fig. 4.10 Results of 2D isentropic vortex advection problem at advection Mach number, M=0.25 (grid resolution test, global-order-of-accuracy, and density contours). 79
Fig. 4.11 Comparison of the LAI and density in three different grid systems at $M\infty = 0.25$. 81
Fig. 4.12 Local-order-of-accuracy index (LAI) of eMLP-VC for four different Mach numbers. 83

Fig. 5.1 Experimental and computational configuration for PROWIM (propeller grids: 241×165×81, background grids: 48 million). 89
Fig. 5.2 Sectional normal force and sectional pressure coefficient of PROWIM ($\alpha wing = 4°, \mathrm{M} = 0.14, \mathrm{Re} = 0.8 \times 106$). 91
Fig. 5.3 Vorticity contour of wake and wing tip vortices. 93
Fig. 5.4 Flowfield of PROWIM using iso-surface visualization method (rortex, $\Omega\mathrm{R} = 0.75$). 95
Fig. 5.5 Smoothness contour of front plane of the propeller classified according to the distinguishing criterion. 97
Fig. 5.6 CFD-CSD loose coupling algorithm and iteration history. 100
Fig. 5.7 Overset grid system of HART II. 101
Fig. 5.8 Local-order-of-accuracy index and vorticity contour at 1.0c above the rotor disk plane {a)WENO-JS, b)WENO-M, c)WENO-Z d) eMLP, e) eMLP-VC}. 103
Fig. 5.9 Local-order-of-accuracy index and q-criterion contour at $\psi = 90°$ plane. 105
Fig. 5.10 Comparison of the local-order-of-accuracy indexes (HART-II). 107
Fig. 5.11 Comparison of the HART-II flowfields using the iso-surface method (Q-criterion). 109
Fig. 5.12 Comparison of load predictions in the 87% radial section. 111
Fig. 5.13 Derivative of the normal force in the 87% radial section. 112
Fig. 5.14 Comparison of the azimuthal derivatives of the normal force (counter-clockwise). 113
Fig. 5.15 Comparison of the noise maps at 2.215 m below the rotor plane (mid-frequency sound pressure level contours). 115
Fig. 5.16 Schematic of design variables. 120
Fig. 5.17 Flowfields of a stacked rotor configuration. 122
Fig. 5.18 Non-dimensional power loading of DOE cases. 123
Fig. 5.19 Effective angle of attack distribution along the blade ($\delta z = 0.1, \delta\theta = 0°, \delta\phi = 90°$) 125
Fig. 5.20 Flowfields comparison of single-rotor and stacked-rotor. 126
Fig. 5.21 Non-dimensional power loading along the vertical spacing (δz). 127
Fig. 5.22 Non-dimensional power loading along the phase angle ($\delta\phi$). 129
Fig. 5.23 Flowfields of BVI cases (Iso-surface using Q-criterion, colored by vorticity magnitude). 130

Fig. 5.24 Effective angle of attack distribution of stacked rotors ($\delta\theta = 2°, \delta z = 0.3D, \delta\phi = -90{\sim}90°$). 132

Fig. 5.25 Non-dimensional coefficients distribution of stacked rotors ($\delta\theta = 2°, \delta z = 0.3D, \delta\phi = -90{\sim}90°$). 132

Fig. 5.26 Flowfield of best DOE configuration. 135

Fig. A1 Schematic of fifth order upwind WENO-type reconstruction. 148

List of Tables

Table 3.1 Characteristics of various limiting functions [19] 24
Table 3.2 Reconstruction methods of enhanced MLP 29
Table 3.3 Modified distinguishing criterion for rotorcraft flowfield 33
Table 3.4 Modified sensing function for robust calculation... 37
Table 3.5 Grid refinement test for linear wave propagation problem.. 43
Table 4.1 Relative computational cost (reference: TVD minmod limiter) 54
Table 4.2 Summary of 1D and 2D benchmark tests 63
Table 5.1 Definitions and ranges of design variables. 121
Table 5.2 Comparison of computational setting information 133
Table B1 Error and global-order-of-accuracy of low amplitude sine wave advection problem (1D) 150
Table B2 Error and global-order-of-accuracy of high amplitude sine wave advection problem (1D) 151
Table B3 Error and global-order-of-accuracy of subsonic gaussian pulse advection problem (1D) 153
Table B4 Error and global-order-of-accuracy of supersonic gaussian pulse advection problem (1D) 154
Table B5 Error and global-order-of-accuracy of isentropic vortex advection problem (2D) 155

Chapter 1. Introduction

1.1 Recent developments of newly designed UAM aircraft

Uber, one of the most popular ridesharing companies in the United States, released a white paper in October 2016 that caused an uproar within the aviation industry [1]. Along with the declaration of starting the service of the so-called ‘air taxi’, which mankind had only dreamed of, Uber presented various requirements that the ‘air taxi’ should have such as vehicle efficiency, noise, and emissions. Urban air mobility (UAM) aircraft, which are another expression of ‘air taxis’, have generated a great deal of interest in aviation-related organizations, research institutes, and universities around the globe. A number of configurations and concepts are being investigated from the conceptual design stage in order to satisfy Uber's requirements. Currently, there are over 700 concepts for UAM aircraft in development or in flight testing [2]. Given that there were only half a dozen configurations at the time the white paper was released, a substantial amount of research is being conducted. Also, in South Korea, several organizations such as Korea Aerospace Research Institute (KARI), Hyundai, Hanwha, and KAI are conducting research on UAM aircraft. In particular, the optionally piloted personal air vehicle (OPPAV), which is an electric vertical take-off and landing (eVTOL) aircraft under development by KARI, is currently in the flight test stage with the goal of completing development in 2023 [3].

The configurations being actively developed as UAM aircraft are new concepts that have not been tried before. Representatively, the wingless-type aircraft generates thrust and lift only with multiple rotors without an additional lifting surface. Fig. 1.1a is representative wingless concept aircraft, VoloCity developed by Volocopter. Since the thrust source does not change depending on the flight mode, the wingless-type aircraft is efficient in that all rotors can be used for the entire flight. It is easy to control using several propulsors, so research and development were conducted extensively in the initial stages. However, the wake generated by each rotor is highly unsteady, which reduces aerodynamic efficiency and at the same time causes blade wake interaction noise and blade vortex interaction noise. Also, unsteady wakes can cause aircraft vibration, decreasing the aircraft's robustness. Another representative concept of UAM aircraft is a lift+cruise-type aircraft. Wisk Aero Cora is an exemplary lift+cruise-type aircraft as shown in Fig. 1.1b. This type of aircraft varies the lift and thrust sources according to the flight mode. It uses rotors for climbing flight and wings and propellers for forward flight. It has the advantage of being able to conduct high speed forward flight. However, due to the parts that are not used in each mode, there are losses in payloads, which can bring reduced range and endurance. Lastly, a vectored thrust-type aircraft similar to the tilt-rotor-type aircraft, such as Bell Boeing's V-22 Osprey, is also being actively studied. With tilting technology, both rotors can be used during hover and forward flight, and the rotor does not need to conduct the edgewise flight during forward flight. However, since the aircraft is very unstable during the tilting operation, it is very challenging to design the aircraft robustly. Bell's Nexus and KARI's OPPAV are the representative vectored thrust-type aircraft, which are shown in Fig. 1.1c and 1.1d.

a) wingless-type, VoloCity

b) lift+cruise-type, Wisk Aero Cora

c) vectored thrust-type, Bell’s Nexus

d) vectored thrust-type, KARI’s OPPAV

Fig. 1.1 Various concepts of UAM aircraft [2]

(a. wingless, b. lift+cruise, c-d. vectored thrust)

Therefore, each type has its own advantages and disadvantages based on the configuration of the aircraft. To ensure successful development, it is necessary to analyze each configuration in depth. These UAM eVTOL aircraft use multiple propulsors in common regardless of their type. Whereas conventional helicopters use one or two large propulsors, UAM eVTOL aircraft adopt multiple and smaller propulsors. By sharing the total thrust required, UAM eVTOL aircraft compensate for the shortcomings of conventional helicopters and offers the following advantages: reduced aeroacoustic noise, robustness against failure, and ease of controllability.

At the same time, however, multiple propulsors yield a much more complicated flow field aerodynamically. Numerous tip vortices generated from the blades are the main cause of its complexity. These vortices stay around the aircraft for a long time and interact directly with the aircraft [4]. Tip vortices interact with the surfaces of the aircraft including the blade and body, and strongly affect not only the aerodynamic performance but also the noise and vibration performance. In fact, the interaction between the blade and the vortex creates strong airloads fluctuations. At the same time, the aerodynamic noise caused by the interaction is propagated downward, which limits the urban operation of the aircraft. Also, the flow field of the UAM eVTOL aircraft has highly unsteady characteristic because of the instability of vortex such as pairing or breakdown. The successful development of UAM eVTOL aircraft will require an accurate and time-accurate prediction of a flow field with these characteristics, as well as a detailed analysis of the flow field.

1.2 Numerical characteristics of rotorcraft flowfield

Because rotorcraft including UAM eVTOL aircraft rotate their blades to obtain lift and thrust, strong tip vortices generated by the blades remain around the aircraft for a long time, creating complicated flow characteristics. As mentioned in the previous section, not only do tip vortices influence aerodynamic performance, but they are also associated with noise and vibration. For this reason, it is most essential to capture the behavior of the vortex and the interaction with lifting surfaces in order to accurately predict the aerodynamic and noise performance of the rotorcraft. However, due to their numerically highly dissipative characteristics and unsteady behavior, such as leap-frog instability and breakdown, tip vortices can be difficult to predict and computationally expensive to compute.

Primitive variables, which are density, velocity, and pressure, have local minima, maxima and stiff gradient around the vortex core. These properties are highly dissipative to deal with numerically. Because the numerical characteristics of vortex core, local minima and maxima, and stiff gradients, are similar to that of the discontinuity, the spatial discretization scheme for compressible flow field activates the limiting process at vortex core region. Artificial dissipation from the limiting process guarantees the robustness of the solver, but at the same time excessively degrades the accuracy of the solver. As a result, the artificial dissipation blurs the behavior of the vortex.

Therefore, the rotorcraft flow field requires a fairly high level of numerical accuracy, and at the same time, computational efficiency is also required in consideration of unsteadiness. In addition, shock discontinuity may occur in the advancing side of rotorcrafts with edgewise flight or rotorcraft capable of advancing at high speed. Although, there will not be a strong shock wave which usually occurs in supersonic fighters or scramjet-type aircraft, but there can be a weak discontinuity, which can cause the instability of the solver. An appropriate shock sensing algorithm is also unavoidable to flow solver.

1.3 Overview of high-order spatial discretization schemes

Due to the aforementioned characteristics in previous chapter 1.2, early rotorcraft aerodynamicists developed and applied various numerical techniques that were robust and could maintain high accuracy. Methods such as mesh adaptation technique, high-order spatial schemes, and additional modeling for rotating machines successfully suppressed the high-dissipative properties of the vortex while maintaining the robustness and efficiency of the solver.

Among the advanced numerical techniques to address dissipative characteristics of vortex, there has been significant interest in high-order spatial schemes because they are cost-effective and can be easily incorporated into existing solvers. Various concepts of high-order spatial schemes have been developed such as compact scheme [5], dispersion-relation-preserving (DRP) scheme [6], weighted essentially non-oscillatory (WENO) scheme [7], central differencing with artificial dissipation scheme [8], total-variation diminishing (TVD) scheme [9], and multi-dimensional limiting process (MLP) scheme [10]. Since each was developed for a different flow field, a spatial discretization scheme suitable for the rotorcraft flow field should be appropriately selected. As the spatial discretization scheme has a significant impact on the accuracy of the solver as well as the robustness and computational efficiency, all of these factors should be considered in the selection process.

The scheme that can achieve the highest accuracy with the same number of stencils is the compact scheme [5,11,12]. Compact schemes, which reconstruct cell interface quantity implicitly, are representative of such schemes. With a relatively small number of stencils, compact schemes produce high order-of-accuracy and satisfactory results in various flowfields such as vortex-dominated [5] and turbulent flows [11]. Weighted compact non-linear scheme, developed for compressible flow, is also a representative low dissipative scheme which is a combination of WENO algorithm and compact scheme [12]. However, compact-type schemes require high computing costs to obtain the cell interface quantity because of the implicit way of reconstruction. In addition, the accuracy is reduced at the overset mesh or parallel boundaries, which are essential for solving the rotorcraft flowfield. These shortcomings limit to being easily used in the existing CFD solver.

Dispersion-Relation-Preservation (DRP) scheme, which considers the dispersion and dissipation error in the frequency domain, also shows notable performances in the aeroacoustics field [6]. Schemes combined with the concepts of WENO-type [13] and TVD-type [14] for stability in compressible flow have also produced highly accurate results in compressible aeroacoustics flowfield. However, DRP-type schemes have a disadvantage in that the optimized stencil weight varies depending on the grid distribution, which impairs the accuracy of the solver in a complex grid system. In addition, since the DRP scheme is designed to maintain a low level of error even at high wavenumbers, the robustness of the solver decreases.

Consequently, the schemes mainly used in rotor flow fields must ensure a certain level of robustness and efficiency while maintaining high accuracy. Scheme mainly used for solvers of rotorcraft-related research institutes, such as NASA's OVERFLOW, DLR's TAU, and ONERA's elsA, satisfy the above requirements. Representative high-order accuracy scheme is the central differencing with artificial dissipation scheme mainly used in NASA OVERFLOW. This scheme only requires an additional computational cost of 10% compared to the 2nd order scheme. On the other hand, the accuracy has the level of 5th order accuracy WENO-JS. Oscillation occurring in a weak shock, not in the hypersonic region, can be sufficiently captured and robustness is guaranteed. However, central-type schemes cannot handle the strong discontinuity occur in hypersonic flow. Also, they do not have unified version of artificial dissipation that vary according to the flow type, so adjusting step is necessary to set the numerical dissipation properly[15].

Another representative scheme is WENO-type scheme. The WENO-type method is a total variation bounded (TVB)-based method. The (*2r-1*)-order accurate WENO [7], first developed by Shu in 1996, is designed to maintain *r*-order accuracy even near discontinuities. In WENO-type schemes, the cell interface quantities are reconstructed using the smoothness of local polynomials. The smoothness indicator decides the weight of a local polynomial. There are some limitations to local extrema in terms of accuracy, but many researchers are developing enhanced WENO-type schemes to counter those limitations. Particularly, advanced WENO schemes such as WENO-M [16], WENO-Z [17], and ESWENO-P [18], which further improved the accuracy near discontinuities, were successfully applied to vortex-dominated rotorcraft flowfields.

TVD-type scheme, also, is representative scheme for compressible flow. TVD-type scheme perfectly deals shock and guarantees robustness. However, this type has a mathematically simple shock sensing function, so it senses not only the shock but also other similar flows with the shock. In particular, in the case of a vortex flow with local extrema, the TVD sensing function cannot unconditionally catch it, which results in a decrease in the accuracy of the vortex flow. In order to take advantage of the robustness of the TVD type scheme and to compensate for its shortcomings, the researchers conducted research aimed at complementing the sensing process. Representatively, in the case of the enhanced MLP (eMLP)-type scheme [14,19–21], a shock-sensing mechanism using the Gibbs phenomena was introduced. The continuous property of the flow field is judged by the criteria using the Gibbs phenomena. Different reconstruction methods are applied on flow field according to the continuous property. Advanced shock-sensing process has the advantage of maximizing accuracy by not applying limiting in continuous flow. eMLP-type schemes have been applied not only to flow fields such as coaxial hovering rotors [22], but also to much more complex flow fields such as turbulent combustion [23] or magnetohydrodynamic [19].

1.4 Research Questions

1.4.1 Question 1: Is it possible to accurately predict the aerodynamic and noise performance of UAM eVTOL aircraft with the schemes that have been developed so far?

The various types of high-order accurate spatial discretization schemes introduced in previous section produce reasonable results for predicting the aerodynamic performance of conventional helicopters. It was possible to accurately predict the blade-vortex interaction (BVI) by applying the developed schemes, and the resulting noise prediction was conducted precisely [24–26]. The prediction performance of the hovering rotor also showed accurate prediction to the extent that the Figure of Merit prediction error came within the experimental error [27]. However, such prediction performance is possible when a large number of grids are constructed. According to the second higher-harmonic control aeroacoustic rotor test (HART-II) experimental study for BVI prediction, at least 50 million grids are required [28]. This is the minimum number of grids generated when a grid spacing at near wake region is 0.1 times the length of the rotor tip chord. In a study on the tiltrotor aeroacoustic model (TRAM), Neal Chaderjian [27] suggests that a grid spacing of 5% chord length is required for accurate prediction of Figure of Merit. It is suggested that a grid of a higher level, that is, a grid spacing of 2.5% tip chord length, is required to investigate vortex dynamics, which resultantly requires more than 1 billion grid points. As such, in order to accurately predict the rotorcraft flow field using the schemes presented so far, it is only possible when a very large number of grids are accompanied. The problem is that the flow field of UAM eVTOL aircraft is much more difficult to predict than conventional helicopters. With an increase in rotors, there is also an increase in the number of vortices that must be preserved. The generated vortex of UAM eVTOL aircraft has a smaller intensity and smaller vortex size than that of conventional helicopter because the disk loading of each propulsor is low. It is necessary to use more grids in order to predict the aerodynamic performance at the same level as for conventional helicopters. At the same time, the prediction difficulty is extremely high because both the interaction between the vortices and the interaction between the vortex and the additional lifting surface must be accurately predicted. As such, an accurate and efficient spatial discretization scheme with much less numerical dissipation than existing schemes is required.

1.4.2 Question 2: What characteristics of the scheme will allow accurate prediction of the rotorcraft flow field? / Is there a standard for evaluating schemes that use different types of concepts?

The development of various high-order accurate schemes has taken place in various ways, and each scheme has its own characteristics. Before applying the schemes to rotorcraft flowfield, the evaluation process should be conducted. Since the rotorcraft flowfield is compressible flow, the nonlinear effect of the scheme must be considered. In addition, the scheme should be evaluated whether it is suitable for rotorcraft flow field with vortex-dominated characteristic rather than a simple flow field such as sine wave advection problem. Among the conventional evaluation methods, the approximate-dispersion-relation (ADR) method can evaluate the non-linear effects of schemes [29]. However, these methods are simplified analyzes based on the linear advection equation which has the exact solution. In a real flowfield without an exact solution, numerical errors can be calculated assuming the experiment value as the ground truth, but this method has a fatal limit that only can be applied when the experiment value exists [30]. As such, it is difficult to evaluate the scheme accuracy in the rotorcraft flow using the conventional method. Therefore, in this study, new index for quantitative assessment of numerical accuracy is suggested. The newly suggested index can help to understand the characteristics of each spatial difference scheme in the local domain. As a result, the essential characteristics of spatial discretization scheme can be identified for high-accuracy prediction of the rotor flow field.

1.5 Objective of the dissertation

Based on the research questions outlined above, this study was constructed as follows: 1) the development of advanced spatial discretization scheme with high accuracy, 2) the suggestion of new standard for evaluating the accuracy of high-order spatial schemes and its applications to assessment of schemes, 3) analyzing the complicated rotorcraft flow fields using suggested scheme.

1) Through the analysis of characteristics of the rotorcraft flow field, a robust, efficient, and high-accurate spatial discretization scheme was developed. Based on the enhanced MLP scheme developed for high accuracy of all flows,

including magnetohydrodynamic flow, three modifications were conducted. To improve accuracy, the flow distinguishing mechanism was modified and a Low Mach number adjustment was adopted. To supplement the robustness, the sensing function is used adaptively.

2) The developed high-order accurate scheme and the schemes widely used in the rotorcraft flow analysis field were compared and analyzed. For quantitative comparative analysis of local accuracy in the discretized domain, a new local-order-of-accuracy index was proposed. Using the suggested index, the properties of spatial discretization schemes suitable for the rotor flow field and the characteristics they should have for precise prediction were discussed.

3) By applying the scheme developed through this study, the complicated rotorcraft flow field was analyzed. Detailed analyses of propeller-wing interaction and BVI were conducted. BVI induced noise prediction was also conducted. Secondly, the design of the co-rotating coaxial rotor for UAM eVTOL aircraft was carried out. Through a parameter study, underlying physics of co-rotating rotor system were identified. Detail flow analysis was performed for the optimal configuration.

Chapter 2. Numerical Approach for Rotorcraft Performance Analysis

2.1 Brief Review of Rotorcraft Aerodynamic Solvers

For the analysis of the aerodynamic performance of rotorcraft, various methods are available: from low-fidelity solvers that are efficient enough to get the results in few seconds to high-fidelity solvers that are highly accurate enough to get whole complicated flow field. The low-fidelity solvers commonly use a simple algebraic expression with several assumptions. Momentum theory solver, which is the simplest solver for rotorcraft aerodynamics, assumes the lifting source as an infinitesimal disk [4]. Blade element theory (BET) solver provides slightly higher fidelity results, which conducts quasi three-dimensional (3D) computations by dividing the blade into spanwise elements [4]. The BET solver usually uses the wake or inflow modeling technique to consider the 3D effect. Also, it uses airfoil table to consider the viscous effect. Mid-fidelity solvers use panel method or the vortex lattice method to get the aerodynamic performance of lifting surfaces. These solvers also use wake or inflow modeling techniques like BET. Because the wake has dominant effect on rotorcraft aerodynamic performance, the vorticity transport model [31,32] that calculates wake effects by transforming the Navier-Stokes (NS) equations into velocity-vorticity form, rather than simple modeling, also widely used for rotorcraft flow fields. Overall, low and mid fidelity solvers are mainly used in the conceptual design phase because their computational costs are cheap and if properly calibrated, fairly reasonable results can be produced. However, it is not universal because it requires new modeling whenever the configuration or airframe concept changes, and the finding proper correction factor requires a lot of time and costs.

Solvers with high-fidelity are commonly based on Reynolds-averaged Navier-Stokes (RANS) or unsteady RANS (URANS) equations. Historically, analyzing the entire domain including the wake region with RANS had limitations because of high numerical dissipation, but with the development of low dissipation numerical techniques, the method is becoming more popular. By using this high-fidelity method, it is possible to perform a physical analysis, since it provides information about the surrounding flow field as well as the aerodynamic performance of the rotor. Also, recently, as computing power has improved, attempts to calculate the rotorcraft using LES or DNS are increasing [33,34]. However, due to extremely heavy computational cost, it is unrealistic to calculate the aerodynamic performance of a UAM eVTOL aircraft or conventional helicopter using LES or DNS, even with increased computing power. Since the Reynolds number is in the order of a million, the grid required to produce well-resolved results is over trillions.

Therefore, in this study, the research was conducted using the URANS solver. KFLOW solver previously developed at KAIST/Konkuk University was used. KFLOW is Cartesian grid-based, compressible, viscous, URANS solver. KFLOW adopts overset grid technique to handle the complicated configuration of aircraft [35]. A number of cases including rotorcraft with highly unsteady flow fields were validated through KFLOW [20,36–41]. Governing equations and discretization methods used in KFLOW will be described in detail in this chapter.

2.1.1 Reynolds-Averaged Navier-Stokes Equations

As the governing equations for rotorcraft flow analysis, URANS equations are used in this study. URANS equations alter the NS equations to model the turbulent flow near walls on a small scale. To accurately predict the aerodynamic performance of aircraft, particularly drag, turbulent flow must be simulated. To well resolve the turbulence near the wall, NS equations requires extensively large number of grids. Therefore, Reynolds suggested a method to calculate the conservative variables by dividing them into mean and fluctuating parts.

First, Navier-Stokes equations can be written as follows:

$$\frac{\partial \bar{Q}}{\partial t}+\frac{\partial \bar{F}}{\partial x}+\frac{\partial \bar{G}}{\partial y}+\frac{\partial \bar{H}}{\partial z}=\frac{\partial \overline{F_v}}{\partial x}+\frac{\partial \overline{G_v}}{\partial y}+\frac{\partial \overline{H_v}}{\partial z} \tag{2.1}$$

where $\bar{Q}$ represents the conservative variables as can be presented as follow:

$$\bar{Q}=\begin{Bmatrix} \rho \\ \rho u \\ \rho v \\ \rho w \\ e \end{Bmatrix} \tag{2.2}$$

where ρ, u, v, w, e represents density, velocity in $x, y,$ and z directions, and total energy, respectively. Through the calorically perfect gas assumption, total energy, e can be expressed as eq. (2.3).

$$e=\frac{p}{\gamma-1}+\frac{1}{2}\rho(u^2+v^2+w^2) \tag{2.3}$$

where p represents pressure. The specific heat ratio, γ is 1.4 in air. $\bar{F}, \bar{G}, \bar{H}$ in eq. (2.1) are convective flux vectors in $x, y,$ and z direction, respectively. $\bar{F}_v, \bar{G}_v, \bar{H}_v$ in eq. (2.1) are viscous flux vectors in $x, y,$ and z direction, respectively.

$$\bar{F} = \begin{Bmatrix} \rho u \\ \rho u^2 + p \\ \rho uv \\ \rho uw \\ u(e+p) \end{Bmatrix}, \quad \bar{G} = \begin{Bmatrix} \rho v \\ \rho uv \\ \rho v^2 + p \\ \rho vw \\ v(e+p) \end{Bmatrix}, \quad \bar{H} = \begin{Bmatrix} \rho w \\ \rho uw \\ \rho vw \\ \rho w^2 + p \\ w(e+p) \end{Bmatrix} \tag{2.4}$$

$$\bar{F}_v = \begin{Bmatrix} 0 \\ \tau_{xx} \\ \tau_{yx} \\ \tau_{zx} \\ u\tau_{xx} + v\tau_{xy} + w\tau_{xz} + k_{tc}\frac{\partial T}{\partial x} \end{Bmatrix},$$

$$\bar{G}_v = \begin{Bmatrix} 0 \\ \tau_{xy} \\ \tau_{yy} \\ \tau_{zy} \\ u\tau_{xy} + v\tau_{yy} + w\tau_{zy} + k_{tc}\frac{\partial T}{\partial y} \end{Bmatrix}, \tag{2.5}$$

$$\bar{H}_v = \begin{Bmatrix} 0 \\ \tau_{xz} \\ \tau_{yz} \\ \tau_{zz} \\ u\tau_{xz} + v\tau_{yz} + w\tau_{zz} + k_{tc}\frac{\partial T}{\partial z} \end{Bmatrix}$$

where τ can be expressed as followings with Newtonian fluid assumption:

$$\lambda = -\frac{2}{3}\mu \tag{2.6}$$

$$\tau_{xx} = \frac{2}{3}\mu\left(2\frac{\partial u}{\partial x} - \frac{\partial v}{\partial y} - \frac{\partial w}{\partial z}\right)$$

$$\tau_{xy} = \mu\left(\frac{\partial u}{\partial y} + \frac{\partial v}{\partial x}\right)$$

$$\tau_{yy} = \frac{2}{3}\mu\left(2\frac{\partial v}{\partial y} - \frac{\partial u}{\partial x} - \frac{\partial w}{\partial z}\right) \quad (2.7)$$

$$\tau_{yz} = \mu\left(\frac{\partial v}{\partial z} + \frac{\partial w}{\partial y}\right)$$

$$\tau_{zz} = \frac{2}{3}\mu\left(2\frac{\partial w}{\partial z} - \frac{\partial u}{\partial x} - \frac{\partial v}{\partial y}\right)$$

k_{tc} in eq. (2.5) means thermal conductivity and can be expressed as follows:

$$k_{tc} = \frac{\mu\gamma R}{Pr(\gamma-1)} \quad (2.8)$$

where Prandtl number, Pr is 0.72 in air.

Reynolds-stress term, R_{ij}, is added to the source term by dividing the flow velocity vector of the governing equation into a mean part and a fluctuating part. This term can be expressed as eq. (2.9) with the Boussinesq assumption that the shear stress of turbulent flow has a linear relationship with the mean rate of strain as in laminar flow.

$$R_{ij} \equiv -\rho\overline{u_i'u_j'} = \mu_T\left[\frac{\partial\overline{u_i}}{\partial x_j} + \frac{\partial\overline{u_j}}{\partial x_i}\right] \quad (2.9)$$

where u_i', u_j' means fluctuating part of velocity, and $\overline{u_i}, \overline{u_j}$ means mean part of velocity. An additional turbulence model is needed to obtain the turbulent eddy viscosity, μ_T.

2.1.2 Turbulent Equations

Equations for simulating turbulence vary widely. There are methods ranging from modeling algebraically determined through simple assumptions to modeling for all terms of Reynolds stress [42]. Since the turbulent flow itself is a random flow, it is known that simply increasing the number of modeling equations does not increase the accuracy of the rotor aerodynamic performance analysis. According to the paper published by Smith et al. [28], which summarizes the experimental and numerical analysis results of the BVI rotor flow, the difference in the turbulence model in the prediction of rotor blade aerodynamics is insignificant. According to their findings, simulating turbulent flow is itself important. According to the results of the recently conducted hovering workshop, the accuracy of the turbulence model varies greatly depending on whether the turbulence model can simulate the laminar-turbulent transition flow [43].

However, the turbulence transition models so far are empirical and experimental-based models. Accordingly, the accuracy of the turbulence transition model varies greatly depending on the model and the object to which it is applied. In addition, an experimental value-based model of rotor blades has not been developed so far. Therefore, in this study, the consideration of transition was not carried out.

The turbulence equations mainly used in the rotor flow field are the widely used Spalart-Allmaras one-equation-type [44] and $k-\omega$ two-equations-type [45,46] models. At least within the rotorcraft flow field, the difference in prediction accuracy between the two equations is insignificant.

2.2 Spatial Discretization Methods

The governing equations are discretized using a cell-centered and finite-volume method (FVM). Determining the flux of a cell interface consists of two steps: 1) interpolation of primitive variables, 2) flux calculation using interpolated primitive variables. In order to interpolate the primitive variable on the surface, 3 cell values are used for each of the left and right sides based on the surface. If the explicit interpolation method is used, interpolation with up to 6th-order accuracy is possible. Then, the flux is calculated using the interpolated variables. Convective flux can be finally determined considering the direction of the wave. In the case of viscous flux, since there is no direction of viscous flux, the value is reconstructed through the central difference method. In this study, the viscous flux was calculated using the second-order central difference method. The 4^{th} and 6^{th}-order central difference method produce little different results compared to that of 2^{nd}-order central difference method.

2.2.1 Reconstruction Methods

KFLOW solver used in this study reconstructs the primitive variables for the determination of cell interface value. Also, to maintain the robustness in the compressible flow, upwind-biased interpolation is conducted. It is known that at least than 5^{th}-order accuracy is required to accurately capture the vortex dynamics in rotorcraft flowfields [20,27,36]. Additionally, according to the previous study by Robert Nichols et al.[47], a 5^{th}-order accurate scheme is able to save more than eight times the grid per dimension over a conventional 2nd-order accurate upwind scheme. For 3D calculations, 512 times coarser grid would be required for the 5th-order accurate scheme. Therefore, KFLOW performs 5th-order accuracy upwind-biased interpolation. Meanwhile, 6 stencils are used, the maximum 6th-order accuracy can be achieved. Upwind reconstruction with 5th-order accuracy can be expressed as follows:

$$q_{\frac{1}{2},L} = \frac{1}{60}(2\bar{q}_{-2} - 13\bar{q}_{-1} + 47\bar{q}_0 + 27\bar{q}_1 - 3\bar{q}_2) \tag{2.10}$$

Central reconstruction with 6th-order accuracy can be expressed as follows:

$$q_{\frac{1}{2},L,R} = \frac{1}{60}(\bar{q}_{-2} - 8\bar{q}_{-1} + 37\bar{q}_0 + 37\bar{q}_1 - 8\bar{q}_2 + \bar{q}_3) \tag{2.11}$$

where $q_{\frac{1}{2}}$ represents cell interface value. Subscript L, R mean left and right state, respectively. $\bar{q}_i$ represents cell averaged value of *i*. Various types of limiting techniques are made to deal with the compressibility effect. Representatively WENO-type, TVD-type, and eMLP-type methods can be used. More details on limiting techniques will be discussed in Chapters 3 and 4.

2.2.2 Flux Functions for convective fluxes

The role of the flux function is to determine the flux at cell interface for the reconstructed primitive variables. In this study, considering the flow environment, the upwind-type AUSMPW+ scheme [48] was used as the flux scheme. AUSMPW+ is one of the AUSM-type schemes, effectively dealing with shock overshoots or numerical oscillations near walls. It is possible, numerically, for the density or pressure value to be negative when the wall and vortex collide as in BVI. AUSMPW+ scheme has positivity preservation characteristics, so that the calculation can be carried out robustly. The flux, $F_{\frac{1}{2}}$ of the cell interface is determined as follows.

$$F_{\frac{1}{2}} = \bar{M}_L^{+} \mathrm{c}_{\frac{1}{2}} \boldsymbol{\Psi}_L + \bar{M}_R^{-} \mathrm{c}_{\frac{1}{2}} \boldsymbol{\Psi}_R + \left(P_L^{+}|_{\alpha=\frac{3}{16}} \boldsymbol{P}_L + P_R^{-}|_{\alpha=\frac{3}{16}} \boldsymbol{P}_R \right) \tag{2.12}$$

where $\boldsymbol{\Psi}_{L,R}$ means $(\rho, \rho u, \rho v, \rho w, \rho H)^{\mathrm{T}}$ in left and right state. $\boldsymbol{P}_{L,R}$ represents $\left(0, p_x, p_y, p_Z, 0\right)^{\mathrm{T}}$. $\mathrm{c}_{\frac{1}{2}}$ is the speed of sound in cell interface. $\bar{M}_{L,R}^{\pm}$ and $\bar{P}_{L,R}^{\pm}$ represents split Mach number and pressure, respectively. Details of each term are presented in [48].

2.3 Temporal Integration Methods

Implicit temporal integration method is used for rotorcraft flow field analysis. There is a considerable size difference between the grids within the rotorcraft flow field. In the grid near the wall, the grid spacing in the wall normal direction compared to the length of the blade tip chord is about 1.0×10^{-6}, whereas the size of the background grid is O(1). Even though the explicit temporal integration produces precise results, time step available is too small due to the stiffness of the problem. In order to perform time integration realistically in a problem with a very large difference in the level of grid spacing, the implicit method must be used.

2$^{\text{nd}}$-order accurate backward difference formula (BDF) was used for implicit temporal integration method. 2$^{\text{nd}}$-order accurate BDF is much more accurate than 1$^{\text{st}}$-

order accurate BDF and guarantees A-stable robustness. Implicit Runge-Kutta (IRK) method with higher accuracy can also be considered, but IRK methods have the disadvantage that they are not robust because they are very sensitive to nonlinear errors [49]. In addition to 2nd-order accurate BDF, a dual time stepping method was introduced to reduce nonlinear error. The overall time integration of the rotor flow field is conducted as follows:

$$\frac{\bar{Q}^{m+1}-\bar{Q}^{m}}{\Delta\tau}+\frac{3\bar{Q}^{m+1}-4\bar{Q}^{n}+\bar{Q}^{n-1}}{2\Delta t}+\bar{R}^{m+1}=0 \tag{2.13}$$

where m means a pseudo time step number, and n means a physical time step number. $\Delta\tau$ and Δt mean pseudo and physical time steps, respectively. $\bar{R}$ means the residual term, which is the sum of the convective term, the viscous term, and the source term. To inverse the matrix, the diagonalized alternating direction implicit (DADI) method developed by Pulliam and Chaussee was used [50]. A DADI approach to approximate the inverse matrix reduces the amount of computation by replacing the inverse matrix computation with a scalar computation. Details are described in [50].

Chapter 3. Development of Advanced Spatial Discretization Scheme for High-Resolution Rotorcraft Flowfield

3.1 Review of eMLP scheme

CFD solvers for compressible flow have been developed focusing on obtaining high-order accurate solutions for the stable capture of discontinuous phenomena such as shock waves. The TVD[9], WENO[7], MLP[10], and eMLP[19] reconstruction methods have generated notable results in compressible flow solvers. However, these methods also have shortcomings, as shown in Table 3.1.

Table 3.1 Characteristics of various limiting functions [19]

	TVD	WENO	MLP	eMLP
Discontinuity in one dimension	O	O	O	O
Discontinuity in multi-dimensions	X	X	O	O
Local extrema	X	O	X	O

Kang et al. proposed eMLP in 2010 [19], and it was developed to overcome the limitations that several existing schemes could not adequately handle, namely the three cases in Table 3.1. Based on MLP [10,51], which has the advantage of robustly capturing discontinuities in multi-dimensions without numerical oscillations, eMLP was developed to prevent the loss of accuracy at local extrema. The method adopted to solve the shortcomings of MLP was the addition of an independent flow distinguishing step. The whole procedure of eMLP is divided into two steps: 1) flow distinguishing and 2) higher-order interpolation. The details are as follows.

3.1.1 Flow Distinguishing Step

Shock-sensing algorithms for discontinuity are included in various forms within each scheme because highly nonlinear phenomena such as shock waves could exist in compressible flows. Local smoothness measurements using slope differences are adopted in TVD and MLP-type methods, and the form of a smoothness indicator using an undivided difference is applied in ENO/WENO-type methods. These methods, however, are simply based on mathematical scalar analyses, making it difficult to distinguish between linear and nonlinear discontinuities. In addition, because the distinguishing mechanisms are inherent in each interpolation method, it is difficult to directly provide accurate information on discontinuities to the flux scheme.

The flow distinguishing step is separated from the interpolation step in eMLP to overcome previous shortcomings. In this step, the flow characteristics are evaluated using the primitive variables (density, velocity vector, and pressure). A fourth-order central differencing scheme is adopted as the sensing function to approximate the primitive variables of cell i. An approximated value can be obtained via

$$\Phi_{i,approximate} = \frac{-\Phi_{i-2}+4\Phi_{i-1}+4\Phi_{i+1}-\Phi_{i+2}}{6} = \Phi_i + O(\Delta\xi^4) \qquad (3\text{-}1)$$

The difference between the original value and the approximated value obtained through eq. (3.1) determines whether the Gibbs phenomenon has occurred or not. On the result of this determination, the flow is divided into three regions: a continuous region, a linear discontinuous region, and a nonlinear discontinuous region. The distinguishing criterion that accounts for the flow characteristics can be expressed as

Continuous region:

$$d_{(\rho,u,v,w,p),i} = \frac{|(\rho,u,v,w,p)_{i,approximate} - (\rho,u,v,w,p)_i|}{|(\rho,u,v,w,p)_i|} < \epsilon \tag{3.2a}$$

Linear discontinuous region:

$$d_{\rho,i} = \frac{|\rho_{i,approximate} - \rho_i|}{|\rho_i|} > \epsilon$$

or

$$d_{(u,v,w),i} = \frac{|(u,v,w)_{i,approximate} - (u,v,w)_i|}{|(u,v,w)_i|} > \epsilon \tag{3.2b}$$

and

$$d_{p,i} = \frac{|p_{i,approximate} - p_i|}{|p_i|} < \epsilon$$

Nonlinear discontinuous region:

$$d_{p,i} = \frac{|p_{i,approximate} - p_i|}{|p_i|} > \epsilon \tag{3.2c}$$

In case that the flow velocity is almost zero, there is a possibility that the velocity distinguishing function could malfunction. To handle this situation, the velocity distinguishing function should be turned off when the velocity magnitude is smaller than an infinitesimal constant. (Through numerical tests, this constant was set as 10^{-6}). The generally recommended threshold value ϵ for determining the occurrence of the Gibbs phenomenon is 0.001-0.01, as suggested by Kang et al. [19]. In most aviation applications, including rotorcraft, accurate results can be produced using 0.01.

3.1.2 Higher-order Interpolation

After the flow distinguishing step, the interpolations of the primitive variables are performed in accordance with the physical characteristics of the three divided regions. First, in the continuous region, high-order interpolation is performed without any limiting process. When the limiting process is applied in the local extrema, it is not possible to maintain the accuracy of the solution due to undesirable numerical dissipation. Therefore, in the continuous region, a simple high-order polynomial interpolation is executed. Second, in the linear discontinuous region, the limiting process is performed using a TVD criterion to handle numerical oscillations caused by contact discontinuities. Multi-dimensional contact discontinuities are smeared by a non-aligned grid system, which can be assumed to be a linear planar wave. In other words, the multi-dimensional linear convection equation can be expressed as a one-dimensional equation, and the oscillation can be effectively removed by the TVD criterion. Finally, an MLP criterion is used in the nonlinear discontinuous region. MLP satisfies the maximum principle in multi-dimensional flows and is able to achieve high accuracy for multi-dimensional shock waves without numerical oscillations. Applying three different reconstruction methods, which are selected based on the characteristics of each area, enables the efficient and accurate interpolation of the primitive variables. Table 3.2 summarizes the interpolation methods applied to the three areas. In order to obtain a high-order accurate solution, the β parameter is applied with fifth-order interpolation, and the MLP coefficient (α) is applied in the same way suggested by Kang et al. [19].

Table 3.2 Reconstruction methods of enhanced MLP

Continuous region	**No limiting function** $\Phi_{\mathrm{L}} = \Phi_{\mathrm{i}} + 0.5\beta_{\mathrm{L}}\Delta\Phi_{\mathrm{i}-\frac{1}{2}}, \qquad \Phi_{\mathrm{R}} = \Phi_{\mathrm{i+1}} - 0.5\beta_{\mathrm{R}}\Delta\Phi_{\mathrm{i}+\frac{3}{2}}$
Linear discontinuous region	**TVD MUSCL limiter** $\phi(\boldsymbol{r_{TVD}}, \beta) = max(0, min(2, 2\boldsymbol{r_{TVD}}, \beta)$ $\Phi_{\mathrm{L}} = \Phi_{\mathrm{i}} + 0.5\phi(\boldsymbol{r_{TVD}}_{\mathrm{L}}, \beta_L)\Delta\Phi_{\mathrm{i}-\frac{1}{2}}, \qquad \Phi_{\mathrm{R}} = \Phi_{\mathrm{i+1}} - 0.5\phi(\boldsymbol{r_{TVD}}_{\mathrm{R}}, \beta_R)\Delta\Phi_{\mathrm{i}+\frac{3}{2}}$
Nonlinear discontinuous region	**Multi-dimensional Limiting Process (MLP)** $\phi(\boldsymbol{r_{TVD}}, \beta) = max(0, min(\alpha, \alpha\boldsymbol{r_{TVD}}, \beta)$ $\Phi_{\mathrm{L}} = \Phi_{\mathrm{i}} + 0.5\phi(\boldsymbol{r_{TVD}}_{\mathrm{L}}, \beta_L)\Delta\Phi_{\mathrm{i}-\frac{1}{2}}, \qquad \Phi_{\mathrm{R}} = \Phi_{\mathrm{i+1}} - 0.5\phi(\boldsymbol{r_{TVD}}_{\mathrm{R}}, \beta_R)\Delta\Phi_{\mathrm{i}+\frac{3}{2}}$

3.2 Modifications of eMLP scheme (eMLP-VC)

As eMLP has been generally developed for a wide variety of flows, including magnetohydrodynamic as well as supersonic and hypersonic flows, the accuracy for rotorcraft flowfields can be further improved. The accuracy can be enhanced by capitalizing on the fact that most flowfields are vortex-dominated and subsonic. Moreover, the robustness of eMLP can be refined by maintaining the consistency of the sensing function and the interpolation method. In the following section, a newly modified eMLP, called eMLP-VC (eMLP for vorticity conservation), which features greater accuracy, efficiency, and robustness, is suggested.

3.2.1 Accuracy Enhancements

■ ***A New Distinguishing Criterion for Vortex-dominated Flow***

The original eMLP uses primitive variables to capture several types of discontinuities that may arise due to compressibility effects [52]. Pressure is used to identify strong nonlinear discontinuities such as a shock wave or a rarefaction wave. Because density and temperature jumps occur without a change in pressure in contact discontinuities, density is chosen for identifying contact discontinuities. A velocity vector is applied for slip discontinuities, which occur when a supersonic jet is present or the type of flow is different. With the original distinguishing mechanism, eMLP can be applied in various compressible flows accurately and efficiently. However, in vortex-dominated flows such as rotorcraft flowfields, where describing the interactions between vortices is important, it is not necessary to detect all the aforementioned flow phenomena. Reorganizing the distinguishing criterion with respect to the vortex-dominated flow characteristics enables a more efficient and accurate analysis.

Vortex profiles are continuous, and the vortices observed in rotorcraft flowfields also have continuous features. Fig. 3.1a displays the isentropic vortex model [51,53]with vortex strength $\beta_v = 5$. The gradients in the primitive variables of the vortex core are visible in Fig. 3.1b. The density and pressure gradients in the vicinity of the core are 0.4-0.6, whereas the velocity gradient is 1.3-1.4. The velocity gradient is two to three times steeper than the density and pressure gradients. The area where the grid is not sufficient can be considered a discontinuous region due to the steep velocity gradient, which can reduce the accuracy of the solution. In addition, in rotorcraft flowfields, there is no need to use the velocity vector as a distinguishing criterion because there is no risk of developing a discontinuity caused by a supersonic jet or a mix of different types of flows. The modified distinguishing criterion for eMLP-VC is presented in Table 3.3.

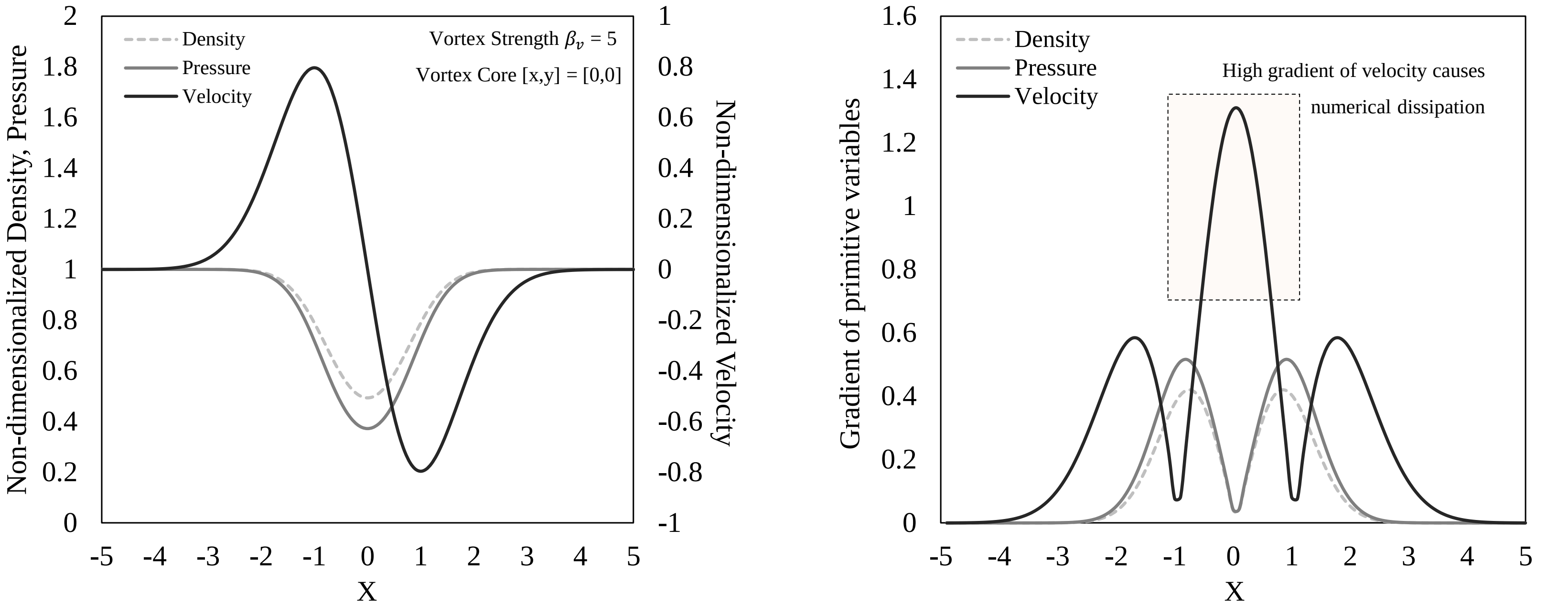

(a) Vortex profile (density, pressure, velocity)

(b) Gradient of primitive variables

Fig. 3.1 Isentropic vortex model's profile and gradient distribution

Table 3.3 Modified distinguishing criterion for rotorcraft flowfield

	Original criterion (eMLP)	Modified criterion (eMLP-VC)	Interpolation method
Continuous region	$d_{\rho,u,w,v,p} < \epsilon$ (for all primitive variables)		No limiting
Linear discontinuous region	$d_{\rho} > \epsilon$ or $d_{u,v,w} > \epsilon$	$d_{\rho} > \epsilon$	TVD limiting
Non-linear discontinuous region	$d_{p} > \epsilon$		MLP limiting

In the modified distinguishing criterion, the flow is classified using only the density and pressure without using the velocity vector, which was originally adopted in eMLP's distinguishing criterion. By excluding the calculation of the velocity vector, the flow distinguishing mechanism becomes much more efficient. A preserving test of the isentropic vortex shown in Fig. 3.1 was performed to verify the performance of the modified distinguishing criterion. The results of the test are shown in Fig. 3.2. The background of Fig. 3.2 shows the density contour when the non-dimensionalized time reaches 20. Each grid point is colored based on the continuity of the flowfield, which is determined by the original and modified distinguishing criterion. When using the modified distinguishing criterion, many of the parts that are judged to be discontinuous regions because of the high velocity gradient are considered continuous regions. This allows for pure high-order polynomial interpolation without any limiting process in the continuous regions, resulting in more accurate solutions. As a result of using the modified distinguishing criterion, 93% of the initial vorticity was preserved, whereas only 81% was preserved when the original distinguishing criterion is used. Therefore, the vortex preserving capability was further enhanced with the modified distinguishing criterion.

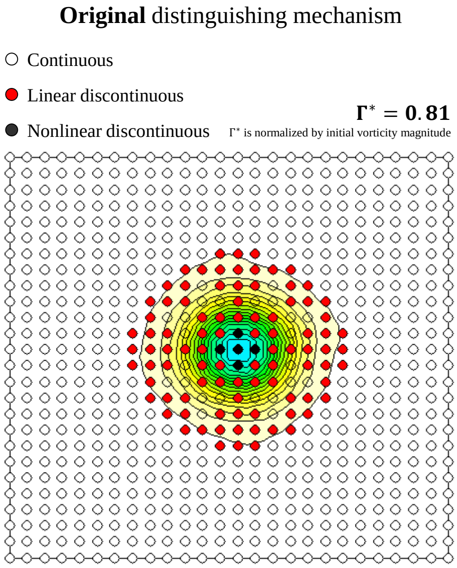

Fig. 3.2 Comparison of results of original/modified distinguishing mechanism and density contour

■ ***Addition of Low Mach Number Adjustment***

Because the conventional upwind-based flow reconstruction methods determine the flux at the cell interface in accordance with the flow direction, the solution for the compressible flow can be accurately and robustly obtained even if discontinuities exist. In incompressible flow at low speed, however, these methods cannot properly predict the flow physics due to excessive numerical dissipation. In case of rotorcraft flowfields, most regions are subsonic except near the tip of the blade, where shock discontinuities can occur. The vortex-dominated area that affects the performance of the rotorcraft is a particularly subsonic region; hence, using upwind-based methods can deteriorate the accuracy of the solution. Through an analysis of TVD limiting interpolation methods, Kim and Kim [54] found a method to prevent the loss of accuracy in upwind-type reconstruction methods in subsonic regions, which they expressed as

$$\Phi_{L,LM} = \Phi_L + \frac{max\left[0,(\Phi_R-\Phi_L)\left|\Phi_{L,sup}-\Phi_L\right|\right]}{(\Phi_R-\Phi_L)\left|\Phi_{L,sup}-\Phi_L\right|} min\left[a\frac{|\Phi_R-\Phi_L|}{2}, \left|\Phi_{L,sup}-\Phi_L\right|\right] \quad (3.3a)$$

$$\Phi_{R,LM} = \Phi_R + \frac{max\left[0,(\Phi_L-\Phi_R)\left|\Phi_{R,sup}-\Phi_R\right|\right]}{(\Phi_L-\Phi_R)\left|\Phi_{R,sup}-\Phi_R\right|} min\left[a\frac{|\Phi_L-\Phi_R|}{2}, \left|\Phi_{R,sup}-\Phi_R\right|\right] \quad (3.3b)$$

where $\Phi_{L,sup}$ and $\Phi_{R,sup}$ are the interpolated values using the TVD superbee limiter, which is used to determine the steepness of the gradient of the original interpolated value. In a gently varying region, a reconstruction of the original interpolated values is performed, which results in a less intense numerical dissipation and a more accurate solution. It is also designed to maintain the complete upwind characteristics in supersonic flows through simple quadratic functions, such as

$$a = 1 - \min(1, max(|M_L|, |M_R|))^2 \quad (3.4)$$

so that there is no loss of accuracy or robustness in supersonic flows.

3.2.2 Robustness Enhancement

An approximated value is calculated using the sensing function in the flow distinguishing step. The original eMLP uses a fourth-order central differencing scheme as the sensing function. If a fifth- or higher-order accurate interpolation, which needs more stencil than the fourth-order central differencing scheme, is performed, a robustness problem may occur. Only the part of the stencil applied in the interpolation process is handled in the flow distinguishing step; if there is a discontinuity at the edge of the stencil, information about the discontinuity may be omitted, causing numerical oscillations. The solver may diverge in case of a strong shock. Hence, the consistency between the interpolation method and the sensing function must be adjusted to prevent the aforementioned problems. The original sensing function was modified according to the equations shown in Table 3.4. The sensing function is adjusted according to the stencil used in the interpolation step. If third-order interpolation is performed, fourth- or higher-order sensing should be performed to include the stencil used in the interpolation step. If interpolation is performed in the fifth-order, the sixth- or higher-order sensing should be implemented. If the order of interpolation step is increased in this way, the order of the sensing function should be raised accordingly.

Table 3.4 Modified sensing function for robust calculation

Interpolation	Modified sensing function
3rd order interpolation $\boldsymbol{\beta_{3rd} = \frac{1 + 2r_{TVD_i}}{3}}$	4th order central differencing scheme $\Phi_{i,approximate} = \frac{-\Phi_{i-2} + 4\Phi_{i-1} + 4\Phi_{i+1} - \Phi_{i+2}}{6} = \Phi_i + O(\Delta\xi^4)$
5th order interpolation $\boldsymbol{\beta_{5th} = \frac{-2/r_{TVD_{i-1}} + 11 + 24r_{TVD_i} - 3r_{TVD_i}r_{TVD_{i+1}}}{30}}$	6th order central differencing scheme $\Phi_{i,approximate} = \frac{\Phi_{i-3} - 6\Phi_{i-2} + 15\Phi_{i-1} + 15\Phi_{i+1} - 6\Phi_{i+2} + \Phi_{i+3}}{20} = \Phi_i + O(\Delta\xi^6)$

The stationary shock discontinuity problem was calculated to verify the appropriateness of the modified sensing function. The initial conditions are

$$(\rho,u,v,w,p)_L = (1.0,2.887,2.887,2.887,1.0) \tag{3.5a}$$

$$(\rho,u,v,w,p)_R = (5.0,0.577,0.577,0.577,29.00) \tag{3.5b}$$

as the normal shock of Mach number 5 is raised at an angle of $45°$ to the grid line.

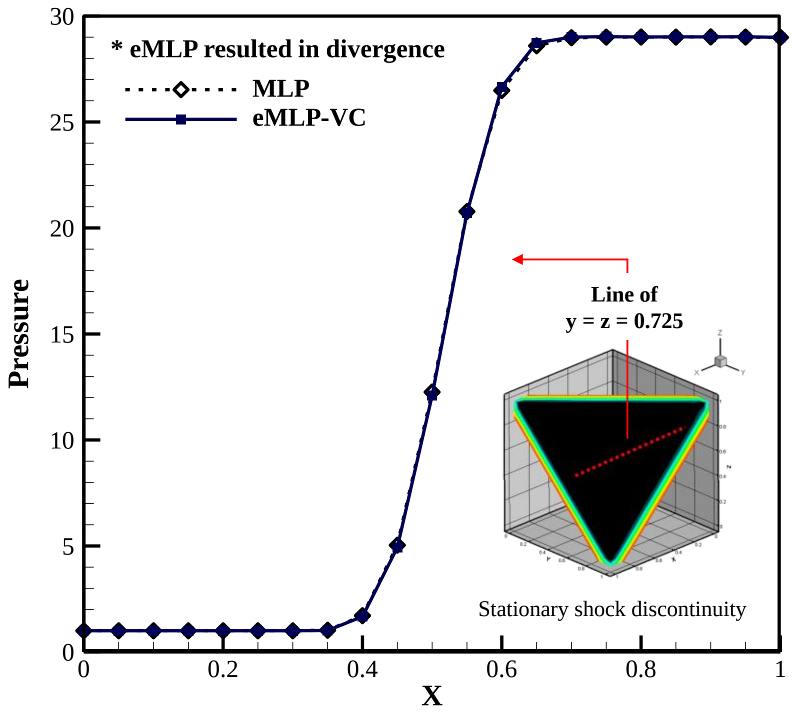

Fig. 3.3 Pressure distribution of cell surface $y = z = 0.725$.

For the steady calculations, a backward Euler method with local time stepping was adopted. The calculation was carried out until the residual dropped below 10^{-5}. The DADI method was used for the efficient inversion of the matrix [50]. The overall computational domain was set as [0,1]×[0,1]×[0,1], and grids of (20×20×20) were evenly distributed. Fig. 3.3 shows the pressure distribution of the cell surface $y = z = 0.725$. When calculating with the modified sensing function, the shock is captured without oscillation, just as in the MLP calculation. However, the calculation with eMLP resulted in a divergence. With the original distinguishing criterion, the information about shock discontinuities is not applied to the sensing function in the cell, where the shock is located at the edge of the stencil. Thus, the limiting process is not applied in the interpolation step, which causes the calculation to fail.

3.3 Advanced performance of eMLP-VC

Three numerical experiments (i.e., linear and nonlinear wave propagation problems, and a double Mach reflection problem) were conducted to assess the eMLP-VC. MLP, eMLP, and "no limiter" methods were compared to evaluate the improved accuracy of eMLP-VC. The "no limiter" method represents 5^{th}-order accurate polynomial interpolation without any limiting process. MLP, eMLP, and eMLP-VC incorporated a 5^{th}-order accurate polynomial as the β function, and the results of fifth-order accuracy were obtained in the region where the limiting process was not applied. All interpolations were performed for primitive variables. The upwind-based flux scheme AUSMPW+ was used for all cases. Other upwind-based schemes such as Roe-type [55] and HLLC-type [56] produced similar results. The third-order TVD Runge-Kutta method was used for time integration, with sufficiently small timesteps in each experiment.

3.3.1 Linear wave propagation problem

The initial linear wave profile is a smooth two-dimensional double sine wave:

$$q_0 = 2 + \sin(2\pi x)\sin(2\pi y) \tag{3.6}$$

The computational domain was [0,1]×[0,1], and each boundary had the periodic condition to assume a domain of infinite size. The grid system was (20×20). The timestep was set as 0.001 to prevent time integration errors from affecting spatial discretization errors. The non-dimensionalized advection velocity was set to 1 in the x-direction and 2 in the y-direction so that the wave returned to its original place at $t = 1$. Fig. 3.4 displays the contour maps showing the solution at $t = 1$ (see Fig. 3.4a, c, e) and the error between the solution and the initial profile (see Fig. 3.4b, d, f). As the results of the eMLP and the "no limiter" were the same, all regions were determined to be continuous through the original distinguishing criterion. The modified distinguishing criterion of eMLP-VC also defines all domains to be continuous. The solution of eMLP-VC was more accurate than that of eMLP due to the reduced numerical dissipation through low Mach number adjustment. When the limiting process is operated in all regions, as in MLP, the wave amplitude decreases due to undesirable numerical dissipation at local extrema, producing results with low accuracy.

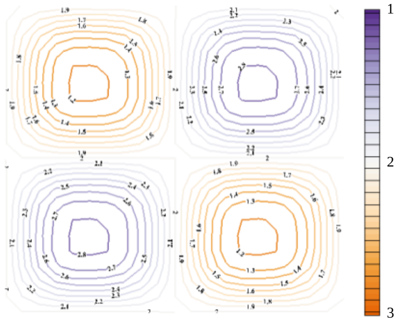

a) MLP, solution

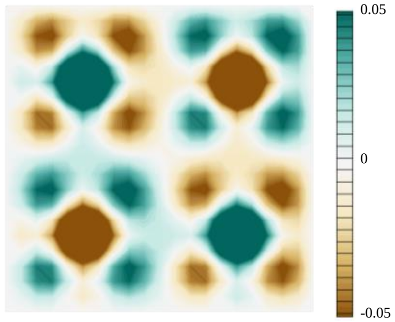

b) MLP, error

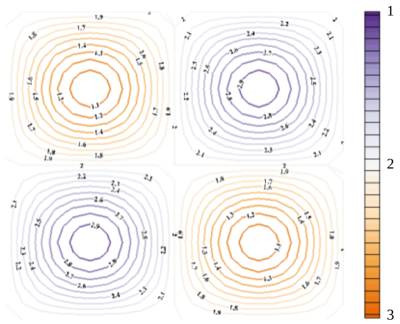

c) eMLP and “no limiter”, solution

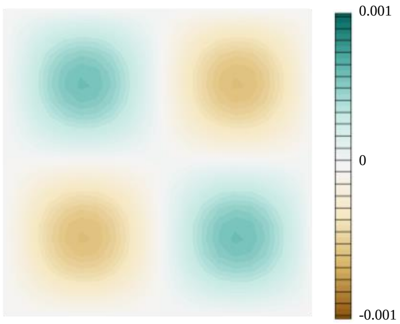

d) eMLP and “no limiter”, error

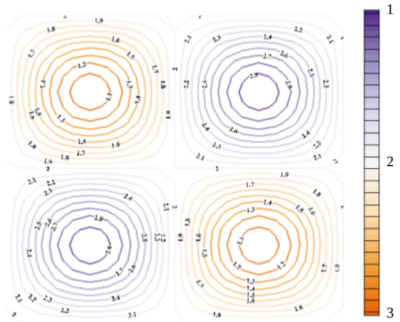

e) eMLP-VC, solution

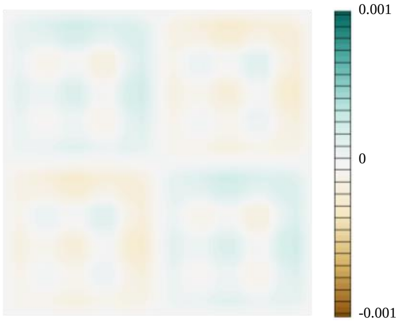

f) eMLP-VC, error

Fig. 3.4 Linear wave propagation problem calculation results at $t = 1$.

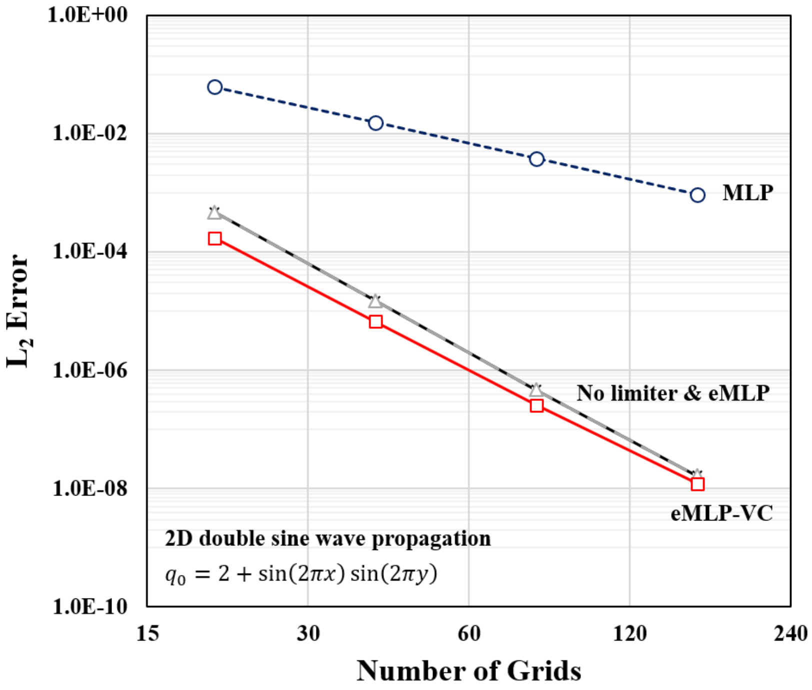

Fig. 3.5 L_2 norm of error of calculation results at $t = 1$.

A grid refinement test was conducted to check the order of accuracy of the linear wave propagation problem and the accuracy according to the grid. Fig. 3.5 shows the L_2 error of the four schemes as a function of the number of grids. The calculations were performed by varying the number of grids in one direction to 20, 40, 80, and 160. MLP, in which the limiting process is carried out in the whole domain, has a much larger L_2 error compared to the other three schemes. eMLP and the "no limiter" have the same result, which means that it was continuous in all domains as assessed by the distinguishing criterion. The orders of accuracy and L_2 errors are shown in Table 3.5. Through the addition of low Mach number adjustment, eMLP-VC is more accurate than the eMLP and "no limiter" which adopts 5^{th}-order polynomial reconstruction in whole domain without any limiting process. Although the order-of-accuracy of eMLP-VC is lower than that of eMLP and “no limiter”, the accuracy is higher than any of the other schemes. In particular, the smaller the grid, the greater the difference in accuracy when compared to eMLP and “no limiter”.

Table 3.5 Grid refinement test for linear wave propagation problem

	Grid system	L_2 error	Order of accuracy
No limiter (5^{th}-order reconstruction)	20×20	4.71E-04	
	40×40	1.49E-05	4.98
	80×80	4.69E-07	4.99
	160×160	1.64E-08	4.84
MLP	20×20	6.17E-02	
	40×40	1.53E-02	2.01
	80×80	3.84E-03	2.00
	160×160	9.36E-04	2.03
eMLP	20×20	4.71E-04	
	40×40	1.49E-05	4.98
	80×80	4.69E-07	4.99
	160×160	1.64E-08	4.84
eMLP-VC	20×20	1.71E-04	
	40×40	6.64E-06	4.69
	80×80	2.57E-07	4.69
	160×160	1.21E-08	4.41

3.3.2 Nonlinear wave propagation problem

In order to compare only the numerical dissipation of spatial discretization methods, the problem of preserving the isentropic vortex in the inviscid flow was selected. The governing equation for this problem is the two-dimensional inviscid and compressible Euler equation. The non-dimensionalized freestream values, which are density, velocity, and pressure, were set to $(\rho, u, v, p) = (1,0,0,1)$. The computational domain was [-5,5]×[-5,5], and each boundary had the periodic condition to assume a domain of infinite size. The intensities of the perturbations in the freestream values due to the initial vortex were determined via

$$\delta u = -\frac{\beta_v}{2\pi}(y - y_0)e^{\frac{1-r_v^2}{2}} \tag{3.7a}$$

$$\delta v = \frac{\beta_v}{2\pi}(x - x_0)e^{\frac{1-r_v^2}{2}} \tag{3.7b}$$

$$\delta T = -\frac{\beta_v^2(\gamma-1)}{8\gamma\pi^2}e^{1-r_v^2} \tag{3.7c}$$

where β_v, the vortex strength, was set to 5 [51,53] and (x_0, y_0), the position of vortex core, was set to (0,0). The distance from the vortex core, r_v, is defined as $r_v = \sqrt{(x - x_0)^2 + (y - y_0)^2}$. Isentropic flow and calorically perfect gas are assumed in this problem. There are two grid systems: a coarse grid system and a fine grid system. The coarse grid system has five grid points and the fine grid system has ten grid points in the vortex core to describe the vortex profile. The time-step was set to 0.01 for both grid systems. The results that occurred at the non-dimensionalized time $t = 50$ were compared.

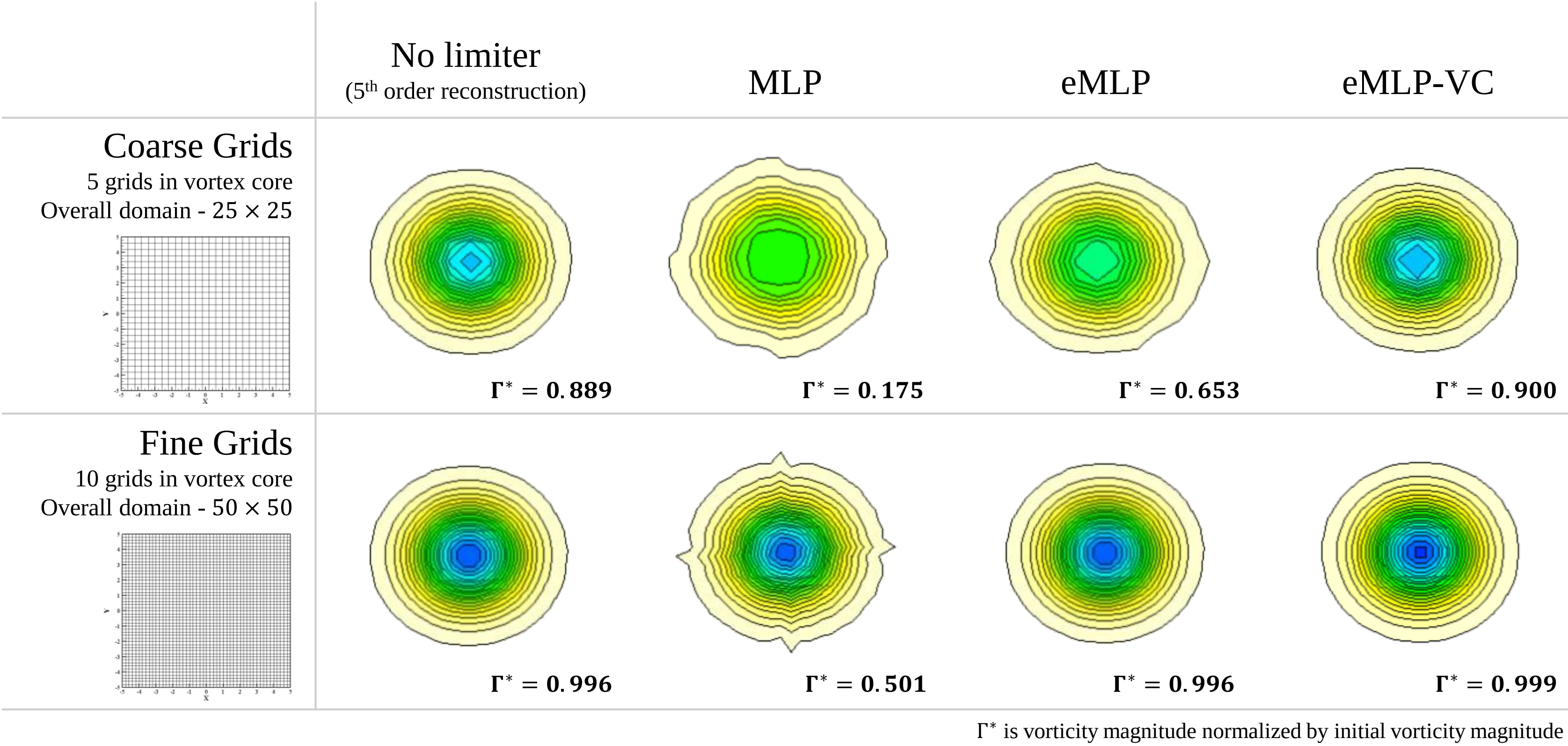

Fig. 3.6 Comparison of density contour (Up: Coarse Grids, Down: Fine grids)

A comparison of the density values of the coarse and fine grid systems is shown in Fig. 3.6. The calculations were performed for four reconstruction methods: "no limiter" (fifth-order polynomial interpolation without any limiting process), MLP, eMLP, and eMLP-VC. Because the number of grids for describing vortex profile is insufficient in the coarse grid system, many parts of the vortex core are deemed discontinuous regions, as shown in Fig. 3.2. The limiting process is performed in those discontinuous areas, which causes the vortex to dissipate due to the excessive numerical dissipation of the limiting process. After the non-dimensionalized time t=50, 17.5% of vorticity is preserved with MLP, 65.3% with eMLP, 88.9% with "no limiter," and 90.0% with eMLP-VC. MLP and eMLP exhibit more loss of vorticity than the "no limiter", but eMLP-VC preserved the vorticity better than the "no limiter". The modified distinguishing criterion of eMLP-VC assessed the majority of the domain to be continuous regions, which reduced the numerical dissipation and improved the accuracy. Furthermore, the low Mach number adjustment is performed in the subsonic region, resulting in highly preserved vorticity. In the fine grid system, the entire domain is gauged to be continuous in both the original and modified distinguishing criterion because the grid system is fine enough to accurately describe the vortex profile. Hence, eMLP assigns pure high-order polynomial interpolation in the entire domain, which preserves the same vorticity as the "no limiter" case. Both eMLP and the "no limiter" preserve 99.6% of the vorticity. When using eMLP-VC, the limiting process is not performed in the whole domain as in eMLP, and the vortex preserving capability is increased due to the low Mach number adjustment. As a result, the vorticity is almost completely preserved (99.9%).

3.3.3 Double Mach Reflection

Double Mach reflection problems have been selected to determine how several modifications in eMLP-VC affected the robustness and accuracy in a strong compressible flow. In this problem, a moving shock of Mach number 10 hits a 30-degrees inclined ramp at $x = \frac{1}{6}$. As the incident shock wave moves, a reflected shock and a Mach stem meet to create a primary triple point, resulting in a slip line and curved flow. Additionally, as the reflected shock breaks up, a secondary Mach stem and a secondary reflected shock are created, and a secondary triple point is created. These phenomena are shown in Fig. 3.7a. To verify the robustness and accuracy of the scheme in the compressible flow, strong moving shock and surrounding physical phenomena must be robustly simulated in high resolution without numerical oscillation. In particular, the resolution of the slip line and curled flow perform as an indicator to judge the accuracy of the numerical scheme [57]. A computational domain for double Mach reflection problem is [0,4]×[0,1] with equally spaced grids. A uniform grid spacing, h, is 1/512. The computation was carried out until the non-dimensionalized time (t) reaches 0.2, with a Courant-Friedrichs-Lewy (CFL) number, 0.8. For the comparison, MLP and eMLP schemes were used. The "no limiter" case was not used in this problem because the calculation diverges if the proper limiting function is not used in the discontinuity. In addition, the modified sensing function was used in eMLP to ensure the robustness.

Fig. 3.7 illustrates the flow structure of the double Mach reflection problem at $t = 0.2$ through density contour and numerical schlieren. The density contour consists of thirty equally spaced lines, representing from $\rho = 2$ to $\rho = 22.5$. Two triple points, the slip line, and the curled flow are shown in a close-up view using numerical schlieren. Fig. 3.7 shows that monotone solutions were achieved through the calculations using MLP, eMLP, and eMLP-VC. Especially results in eMLP and eMLP-VC, the curled flow generated from the slip line is clearly resolved.

The accuracy and robustness of eMLP-VC were verified through linear wave propagation, nonlinear wave propagation, stationary shock discontinuity, and double Mach reflection problems. eMLP-VC demonstrates a higher accuracy than the methods without a limiting process in the continuous area, and it robustly captures multi-dimensional discontinuities without numerical oscillations. For rotorcraft flowfields where vortex-dominated regions and multi-dimensional discontinuities exists, eMLP-VC is a good alternative to the conventional high-order accurate scheme.

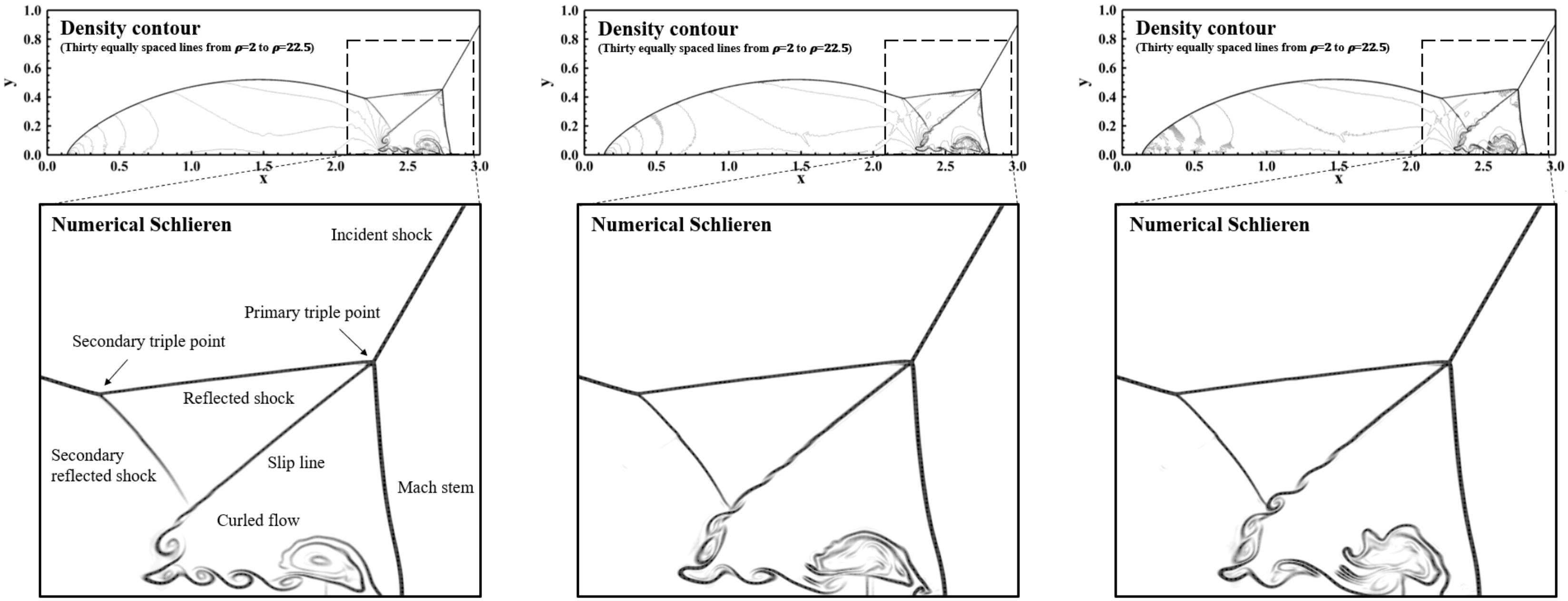

a) MLP b) eMLP c) eMLP-VC

Fig. 3.7 Comparison of density contour and numerical schlieren for double Mach reflection problem $\left(h = \frac{1}{512},\ t = 0.2\right)$.

Chapter 4. Comparative Assessment of High-Order Spatial Schemes in Terms of Local Accuracy

Several benchmark tests have been conducted to verify the accuracy of the eMLP-VC presented in the previous chapter. eMLP-VC showed excellent vorticity preservation capabilities while also showing the robustness even when strong shock waves exist. However, it is unknown whether it will perform well even when compared to the scheme that is conventionally used in rotorcraft flow fields, such as WENO-type schemes. In addition, if the accuracies of those schemes are different, a thorough investigation of the reasons for the performance difference is essential.

Although high-order spatial schemes can give reliable predictions of the aerodynamic performance of rotorcraft, the actual prediction accuracy in an aeroacoustic problem, which demands much higher accuracy, tends to be insufficient. The main reason for insufficiency is the reduced order-of-accuracy in the local computational domain. High-order spatial schemes insist that they theoretically produce the same order-of-accuracy in the entire computational domain. However, these schemes unintentionally switch the order-of-accuracy according to the type of flowfield. Because high-order spatial schemes include the non-linear part for robustness, it is inherently difficult to maintain a constant order-of-accuracy. The primary role of the non-linear part, designed using a different approach for each scheme, is to deal with discontinuities in a robust manner. When a discontinuity is observed in the domain, the non-linear part plays the role of artificial dissipation to prevent the oscillation of numerical results. The problem is that this part can be activated where a discontinuity does not exist. If an insufficient number of grids is given or the gradients of flow quantities are salient, the scheme can erroneously detect a continuous region as a discontinuous region. This brings unnecessary numerical dissipation and reduces the order-of-accuracy of numerical solutions.

For a more accurate prediction of a vortex-dominated rotorcraft flowfield and aeroacoustic characteristics of rotorcraft, the high-order spatial scheme should maintain the theoretical order-of-accuracy in the entire continuous computational domain. To identify the actual accuracy of a scheme in the discretized domain, an assessment in terms of local accuracy is required. There are several assessment techniques to identify the local accuracy of the scheme. Modified wavenumber analysis can estimate the dissipation and dispersion error of each scheme [29,58]. The ADR method, which is improved version of modified wavenumber analysis, is particularly useful for evaluating the non-linear effects of spatial schemes [29]. Even so, the ADR method is based on the simple linear advection equations, which have exact solutions. Consequently, the error in rotorcraft flow fields cannot be analyzed using the ADR method.

A suitable alternative may be to use the scheme's truncation error. Since the high-order spatial scheme yields a low-order truncation error locally while adjusting the stencil weight, the actual accuracy in the discretized domain can be analyzed by using the difference between ideal truncation error and applied truncation error.

In this chapter, the local-order-of-accuracy index (LAI) is newly defined for the quantitative assessment of local accuracy. The LAI compares the ideal accuracy of the high-order spatial scheme and the applied accuracy in terms of truncation error. The LAI represents the local accuracy of the applied scheme and can be computed in any problem. Five high-order spatial schemes are comparatively assessed in terms of local accuracy. The effect of the local accuracy of each scheme on performance prediction is investigated in aeroacoustic benchmark tests, including rotorcraft flowfield (HART-II problem [28]). LAI analyses show the change in order-of-accuracy of the scheme according to the flow velocity, flow characteristics, and grid number. Based on the results of analyses, essential requirements for precise prediction are proposed.

Spatial schemes in compressible flows had been developed to focus on capturing the shock discontinuity in a robust manner. However, such schemes have limitations in vortex-dominated flow, which requires relatively high accuracy. Recently, spatial schemes have progressed in such way that satisfies both robust shock-capturing and high-accuracy requirements. Several spatial schemes with high-order accuracy give reliable results even in rotorcraft flowfields, where tip and secondary vortices prevail.

Five high-order spatial schemes are compared to establish the essential requirements for precise rotorcraft performance prediction. Two schemes (eMLP [19], eMLP-VC [20]) were selected as improved versions of the TVD scheme. For the WENO-type scheme, the original WENO scheme and two advanced schemes were selected: WENO-JS [7], WENO-M [16], and WENO-Z [17]. A brief review of

WENO-type schemes are presented in Appendix A. A local truncation error analysis is performed to compare the accuracies of the advanced schemes. Different types of n^{th}-order accurate spatial discretization schemes are quantitively assessed using the LAI.

4.1 Computational costs of high-order spatial schemes

Even for a scheme with high order-of-accuracy and robust shock-capturing performance, if the computational cost of the scheme is unreasonable, its value decreases. Therefore, before evaluating the numerical performance of the previously introduced schemes, the computational cost for a simple problem was assessed first. WENO-JS, WENO-M, and WENO-Z were chosen as WENO-type schemes, and eMLP and eMLP-VC were selected as eMLP-type schemes. All settings except for the reconstruction scheme were the same. The Governing equation for the test case was set as the Euler equation. The upwind function was used as the flux function. The reconstruction was performed for primitive variables. The result of the TVD minmod limiter was used as the reference value. 1000 steps were advanced using 161×161×161 grids. The first-order backward difference formula with the DADI method [50] was used as the temporal integration method. After performing the same test 10 times for each scheme, the calculation time of 8 cases, excluding the cases that took the most and the least time was averaged. Intel Xeon Gold-6254 processor was used for the calculation. The results are shown in Table 4.1.

Table 4.1 Relative computational cost (reference: TVD minmod limiter)

Spatial discretization schemes	Computational cost (%)
WENO-JS	27.0
WENO-M	50.4
WENO-Z	29.1
eMLP	30.8
eMLP-VC	30.3

All schemes have a cost of about 25% more than that of the second-order accurate TVD minmod limiter. The costs of the schemes are similar except for WENO-M, which is about twice as expensive as WENO-JS. Although WENO-Z is an improved version of WENO-JS, WENO-Z has not much increased cost. eMLP-VC is also an advanced version of eMLP; the cost of eMLP-VC is rather reduced.

4.2 Analysis of Local truncation error

4.2.1 Local truncation error analysis using taylor series expansion

Explicit n^{th}-order accurate schemes such as the WENO- and eMLP-type schemes use polynomials with n^{th}-order accuracy to reconstruct the cell interface quantity. Assuming equally spaced grid points, the approximated quantity can be expressed as follows:

$$q(x) = l_n x^n + l_{n-1} x^{n-1} + \cdots + l_1 x + l_0 \tag{4.1}$$

where $l_i (i = 0,1,\cdots,n)$ is the polynomial constant. The cell averaged quantity with conservative properties can be expressed as follows:

$$\bar{q}_m = \frac{1}{\Delta x}\int_{\left(m-\frac{1}{2}\right)\Delta x}^{\left(m+\frac{1}{2}\right)\Delta x} q(x)dx \tag{4.2}$$

As shown in Fig. 4.1, $\bar{q}_m$ is the averaged quantity of cell m. Δx indicates the grid point spacing. The cell interface quantity, $q_{\frac{1}{2}}$, can be reconstructed, as shown in Eq. (11), using r stencils to the left and $(n-r)$ stencils to the right based on the 1/2 side.

$$q_{\frac{1}{2}} = \sum_{m=-(r-1)}^{(n-r)} c_m \bar{q}_m = q_{\frac{1}{2},exact} + O(\Delta x^n) \tag{4.3}$$

In eq. (4.3), c_m is the stencil weight, and $q_{\frac{1}{2},exact}$ is an exact physical quantity at the cell interface. The fifth-order accurate upwind-type polynomial scheme can be expressed as eq. (4.4a). The sixth-order accurate central-type polynomial scheme can be expressed as eq. (4.4b).

$$\begin{aligned} q_{\frac{1}{2}} &= \frac{1}{60}(2\bar{q}_{-2} - 13\bar{q}_{-1} + 47\bar{q}_0 + 27\bar{q}_1 - 3\bar{q}_2) \\ &= q_{\frac{1}{2},exact} - \frac{1}{60}\frac{d^5\bar{q}}{dx^5}\bigg|_{x=x_0} + O(\Delta x^6) \end{aligned} \tag{4.4a}$$

$$\begin{aligned} q_{\frac{1}{2}} &= \frac{1}{60}(\bar{q}_{-2} - 8\bar{q}_{-1} + 37\bar{q}_0 + 37\bar{q}_1 - 8\bar{q}_2 + \bar{q}_3) \\ &= q_{\frac{1}{2},exact} + \frac{31}{4320}\frac{d^6\bar{q}}{dx^6}\bigg|_{x=x_0} + O(\Delta x^7) \end{aligned} \tag{4.4b}$$

Equation (4.4a) shows the left state of the cell interface quantity of the upwind scheme. The right state of the cell interface can be obtained by applying the weight symmetrically, moving the stencil by one grid to the right. In the case of the central scheme, both left and right states can be obtained, as shown in eq. (4.4b). The weights applied in eq. (4.4) are the optimal weights corresponding to fifth- and sixth-order accuracy, that is, $\boldsymbol{c_{5th,optimal}} = \frac{1}{60}[2, -13, 47, 27, -3]^T$ and $\boldsymbol{c_{6th,optimal}} = \frac{1}{60}[1, -8, 37, 37, -8, 1]^T$, respectively. The truncation errors in Eq. (12) are $-\frac{1}{60}\frac{d^5\bar{q}}{dx^5}\Big|_{x=x_0} + O(\Delta x^6)$ and $+\frac{31}{4320}\frac{d^6\bar{q}}{dx^6}\Big|_{x=x_0} + O(\Delta x^7)$, respectively, which can be obtained by Taylor series expansion.

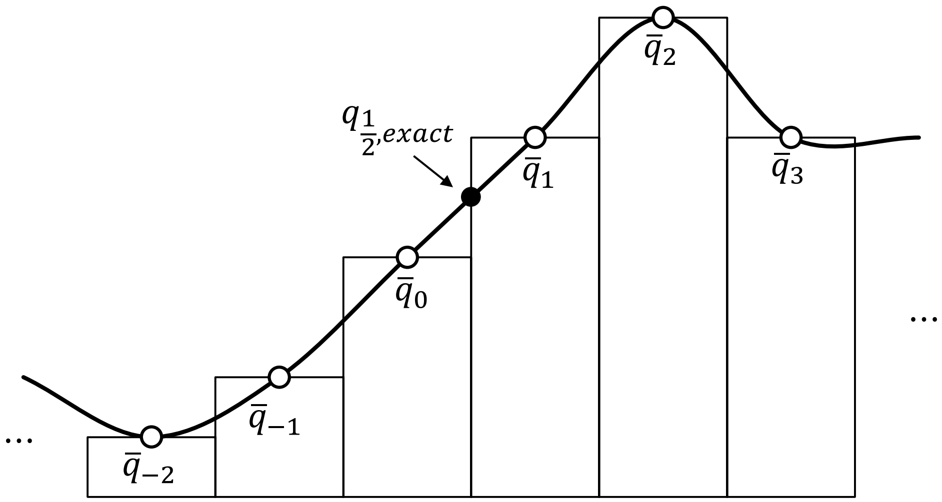

Fig. 4.1 Physical distribution and cell-centered quantities.

The n^{th}-order accurate spatial discretization schemes used for compressible flow, including the WENO- and eMLP-type schemes, have optimal accuracies in the grid system, which is sufficient to represent the change in flow in the incompressible region with low velocity and in the smooth region without flow discontinuity. However, in the region where compressibility and discontinuity occur, the stencil weight is adjusted using the schemes in a specific manner to address them robustly.

In other words, the stencil weight changes locally, depending on various factors, such as the nature of the flowfield and the quality of the grid system. Thus, the schemes do not have an ideal accuracy in all the domains. For example, in the case of a simple flow in which a smooth sine wave advects, high-order accuracy will be applied in all areas if an appropriate grid system is ensured and the wave propagation velocity is low. However, if an insufficient grid system is used to express this sine wave or if the propagation velocity is high, the applied spatial scheme adjusts the stencil weight accordingly. Consequently, artificial dissipation is applied by adjusting the weight from the optimal weight, and local accuracy decreases. In predicting the aerodynamic performance of a simple flow, local accuracy degradation may not meaningfully affect the performance prediction. However, in aeroacoustic problems where small pressure perturbations can affect the final noise performance, local accuracy degradation can have a significant impact. Therefore, even with the high-order accurate schemes which have theoretically the same order-of-accuracy, a scheme that does not easily decrease local accuracy should be used.

It seems difficult to directly compare the local errors of different types of discretization schemes because they reconstruct cell interface quantities through completely different approaches. However, direct comparisons are possible in terms of truncation error because schemes change the stencil weight in their respective manners, and the ideal weight is fixed. Using Taylor series expansion, exact cell interface quantity, $q_{\frac{1}{2},exact}$, based on cell averaged quantity, $\bar{q}_i$, at $i = 0$ can be expressed as follows:

$$q_{\frac{1}{2},exact} = \bar{q}_0 + \frac{1}{2}\bar{q}_0{}^{(1)}(\Delta x)^1 + \frac{1}{12}\bar{q}_0{}^{(2)}(\Delta x)^2 - \frac{1}{720}\bar{q}_0{}^{(4)}(\Delta x)^4 + O(\Delta x)^6 \quad (4.5)$$

Using eq. (4.5) and Taylor series expansion, the difference between each cell averaged quantity and exact cell interface quantity can be expressed as follows:

$$\bar{q}_{-2} = q_{\frac{1}{2},exact} - \frac{5}{2}\bar{q}_0{}^{(1)}(\Delta x)^1 + \frac{23}{12}\bar{q}_0{}^{(2)}(\Delta x)^2 - \frac{4}{3}\bar{q}_0{}^{(3)}(\Delta x)^3 +$$

$$\frac{481}{720}\bar{q}_0{}^{(4)}(\Delta x)^4 - \frac{4}{15}\bar{q}_0{}^{(5)}(\Delta x)^5 + O(\Delta x)^6 \quad (4.6a)$$

$$\bar{q}_{-1} = q_{\frac{1}{2},exact} - \frac{3}{2}\bar{q}_0{}^{(1)}(\Delta x)^1 + \frac{5}{12}\bar{q}_0{}^{(2)}(\Delta x)^2 - \frac{1}{6}\bar{q}_0{}^{(3)}(\Delta x)^3 +$$

$$\frac{31}{720}\bar{q}_0{}^{(4)}(\Delta x)^4 - \frac{1}{120}\bar{q}_0{}^{(5)}(\Delta x)^5 + O(\Delta x)^6 \quad (4.6b)$$

$$\bar{q}_0 = q_{\frac{1}{2},exact} - \frac{1}{2}\bar{q}_0{}^{(1)}(\Delta x)^1 - \frac{1}{12}\bar{q}_0{}^{(2)}(\Delta x)^2 -$$

$$\frac{1}{720}\bar{q}_0{}^{(4)}(\Delta x)^4 + O(\Delta x)^6 \quad (4.6c)$$

$$\bar{q}_1 = q_{\frac{1}{2},exact} + \frac{1}{2}\bar{q}_0{}^{(1)}(\Delta x)^1 + \frac{5}{12}\bar{q}_0{}^{(2)}(\Delta x)^2 + \frac{1}{6}\bar{q}_0{}^{(3)}(\Delta x)^3 +$$

$$\frac{31}{720}\bar{q}_0{}^{(4)}(\Delta x)^4 + \frac{1}{120}\bar{q}_0{}^{(5)}(\Delta x)^5 + O(\Delta x)^6 \quad (4.6d)$$

$$\bar{q}_2 = q_{\frac{1}{2},exact} + \frac{3}{2}\bar{q}_0{}^{(1)}(\Delta x)^1 + \frac{23}{12}\bar{q}_0{}^{(2)}(\Delta x)^2 + \frac{4}{3}\bar{q}_0{}^{(3)}(\Delta x)^3 +$$

$$\frac{481}{720}\bar{q}_0{}^{(4)}(\Delta x)^4 + \frac{4}{15}\bar{q}_0{}^{(5)}(\Delta x)^5 + O(\Delta x)^6 \quad (4.6e)$$

$$\bar{q}_3 = q_{\frac{1}{2},exact} + \frac{5}{2}\bar{q}_0{}^{(1)}(\Delta x)^1 + \frac{53}{12}\bar{q}_0{}^{(2)}(\Delta x)^2 + \frac{2}{9}\bar{q}_0{}^{(3)}(\Delta x)^3 +$$

$$\frac{2431}{720}\bar{q}_0{}^{(4)}(\Delta x)^4 + \frac{81}{40}\bar{q}_0{}^{(5)}(\Delta x)^5 + O(\Delta x)^6 \quad (4.6f)$$

where $\bar{q}_0{}^{(i)} = \left.\frac{d^i\bar{q}}{dx^i}\right|_{x=x_0}$. The i^{th}-order truncation error coefficients are defined as $\boldsymbol{e_i}(i = 1,2,\cdots)$. For example, first-order truncation error coefficients, $\boldsymbol{e_1}$, are defined as $\left[-\frac{5}{2}, -\frac{3}{2}, -\frac{1}{2}, \frac{1}{2}, \frac{3}{2}, \frac{5}{2}\right]^T$ and second-order truncation error coefficients, $\boldsymbol{e_2}$, are defined as $\left[\frac{23}{12}, \frac{5}{12}, -\frac{1}{12}, \frac{5}{12}, \frac{23}{12}, \frac{53}{12}\right]^T$. By combining the stencil weights ($\boldsymbol{c}$) calculated for each scheme and the i^{th}-order truncation error coefficients ($\boldsymbol{e_i}$), the truncation error of each cell interface quantity can be calculated. In other words, $\boldsymbol{c^T} \cdot \boldsymbol{e_i}$ implies the i^{th} order truncation error of the scheme. If $\boldsymbol{c^T} \cdot \boldsymbol{e_1}$ (first-order truncation error) is zero, and $\boldsymbol{c^T} \cdot \boldsymbol{e_2}$ (second-order truncation error) has a non-zero value in a specific cell interface, then this scheme is locally second-order accurate.

4.2.2 Local-Order-of-Accuracy Index (LAI)

In this section, to generalize the discussion of the above section and to compare the local truncation errors generated by each spatial discretization scheme, an index that satisfies the following requirements is proposed.

R1. For the n^{th}-order accurate spatial discretization schemes using an n-point stencils, the index should be consistently applicable in the same manner.

R2. The index should also be applicable for the comparison of schemes using different orders or numbers of stencils.

The index that satisfies the above conditions is called the LAI and can be expressed as follows:

$$\mathrm{LAI} = 1 + \sum_{k=1}^{\mathrm{n}} \prod_{i=1}^{k} \max\left\{0, \left(1 - \frac{|\boldsymbol{c}^{\boldsymbol{T}} \cdot \boldsymbol{e}_{\boldsymbol{i}}|}{|\Gamma_i|}\right)\right\} \tag{4.7}$$

$$= 1 + \max\left\{0, \left(1 - \frac{|\boldsymbol{c}^{\boldsymbol{T}} \cdot \boldsymbol{e}_{\boldsymbol{1}}|}{|\Gamma_1|}\right)\right\} + \max\left\{\left(1 - \frac{|\boldsymbol{c}^{\boldsymbol{T}} \cdot \boldsymbol{e}_{\boldsymbol{1}}|}{|\Gamma_1|}\right)\right\} \max\left\{0, \left(1 - \frac{|\boldsymbol{c}^{\boldsymbol{T}} \cdot \boldsymbol{e}_{\boldsymbol{2}}|}{|\Gamma_2|}\right)\right\} +$$

$$\cdots + \max\left\{0, \left(1 - \frac{|\boldsymbol{c}^{\boldsymbol{T}} \cdot \boldsymbol{e}_{\boldsymbol{1}}|}{|\Gamma_1|}\right)\right\} \max\left\{0, \left(1 - \frac{|\boldsymbol{c}^{\boldsymbol{T}} \cdot \boldsymbol{e}_{\boldsymbol{2}}|}{|\Gamma_2|}\right)\right\} \cdots \max\left\{0, \left(1 - \frac{|\boldsymbol{c}^{\boldsymbol{T}} \cdot \boldsymbol{e}_{\boldsymbol{n}}|}{|\Gamma_n|}\right)\right\}$$

The LAI consists of the sum and product of $\max\left\{0, \left(1 - \frac{|\boldsymbol{c}^{\boldsymbol{T}} \cdot \boldsymbol{e}_{\boldsymbol{i}}|}{|\Gamma_i|}\right)\right\}$ that represents a function of the i^{th}-order error measure. Γ_i is a constant for normalizing $\boldsymbol{c}^{\boldsymbol{T}} \cdot \boldsymbol{e}_{\boldsymbol{i}}$ and is defined as the i^{th}-order truncation error coefficient generated during the i^{th}-order accurate polynomial reconstruction. $\Gamma_1 = \frac{1}{2}, \Gamma_2 = -\frac{1}{6}, \Gamma_3 = \frac{1}{12}, \Gamma_4 = -\frac{1}{30}, \Gamma_5 = -\frac{1}{60}$.

Important properties for the LAI for the n^{th}-order accurate scheme comparison are as follows:

1. An explicit spatial discretization scheme using n stencils can yield the LAI value up to n. For example, the LAI of the fifth-order polynomial is 5. The LAI of the WENO-type scheme can have a value of 3–5 because the five-point stencil fifth-order accurate WENO-type scheme has at least a third-order accuracy in the flowfield. The LAI of the fifth-order eMLP can have a value of 1–5 because the eMLP reconstructs the flowfield using different approaches in each distinguished region. In the case of eMLP-VC, with a low Mach number adjustment, the LAI can have a value of 1-6.

2. $\frac{|c^T \cdot e_i|}{|\Gamma_i|}$ stands for the i^{th}-order error measure. If the i^{th}-order error measure ($i \leq n-1$) is zero and the n^{th}-order truncation error is smaller than that of the n^{th}-order polynomial, the LAI value is $(n+ \alpha)$. $(0 < \alpha < 1)$. It can be considered that the scheme has $(n+\alpha)^{th}$-order accuracy. If the i^{th}-order error measure ($i \leq n-1$) is zero and the n^{th}-order truncation error is larger than or equal to that of the n^{th} order polynomial, the LAI value is n. It's because the i^{th}-order error measure ($i \leq n-1$) is still zero.
3. The low-order error measure limits the influence of the high-order error measures on the LAI. If the low-order error measure goes large, a reduced LAI index will be yielded even if the high-order error measure is small.

In the case of different types of schemes (such as, eMLP- and WENO-type), local truncation errors can be compared using the LAI. Even when the number of stencils varies or the ideal accuracy varies, the LAI can be extended and used in the same manner. However, accuracy comparison using the truncation error is physically meaningful only in the subsonic region where the physical quantity is distributed smoothly. The comparison is difficult to be applied in the region where a jump in a physical quantity occurs. Since the LAI was developed under the assumption of equally spaced grids, it can be only used on equally spaced grids. In addition, although the LAI value itself does not have any physical meaning, it can be used for quantitative comparison and analysis of the numerical errors of each scheme.

4.3 Assessment of high-order spatial schemes through benchmark tests

To compare the local truncation error distribution and acoustic predictability of high-order spatial numerical schemes in rotorcraft flowfield, four different representative benchmark problems were solved. For one-dimensional (1D) simulations, sine wave and gaussian pulse advection problem were selected. The sine wave and Gaussian pulse represent low and high frequency waves, respectively. The global-order-of-accuracy of each scheme was confirmed through the grid convergence test. Five schemes all have fifth-order accuracy in theoretically. Only eMLP-VC can yield up to sixth-order accuracy when the flow Mach number is zero. The accuracy of each scheme was compared through the LAI distribution in variable grid levels. For two-dimensional (2D) simulation, non-isothermal acoustic pulse propagation problem and isentropic vortex advection problem were selected. These two flows, which exist dominantly in the actual rotorcraft flowfield, are suitable for assessing aeroacoustics predictability of high-order accurate schemes. In particular, the performances of high-order accuracy schemes were assessed at relatively coarse grids considering the grid system of the actual engineering field. Table 4.2 contains a summary of benchmark tests.

Table 4.2 Summary of 1D and 2D benchmark tests

	1D		**2D**	
	Sine wave advection	**Gaussian pulse advection**	**Acoustic pulse propagation**	**Isentropic vortex advection**
Governing Equation	Scalar conservation law $$\frac{\partial q}{\partial t} + a_{SCL}\frac{\partial q}{\partial x} = 0$$ (a_{SCL} = advection speed)		Non-dimensional, compressible Euler equation $$\frac{\partial \bar{Q}}{\partial t} + \frac{\partial \bar{F}}{\partial x} + \frac{\partial \bar{G}}{\partial y} = 0$$ ($\bar{Q}$ = conservative variables, $\bar{F}, \bar{G}$ = convective fluxes)	
Flux function	Upwind		Local Lax Friedrich	
Temporal Integration	Explicit 3rd order TVD Runge-Kutta scheme			
Test objectives	Low frequency waves (low / high amplitude)	High frequency waves	Acoustic waves due to pressure perturbation in lifting surface	Vortex dynamics near lifting surfaces

4.3.1 1D Sine Wave Advection

Sine waves with two different amplitudes were advected to the right direction in this problem. The advection speed, a_{SCL}, was set to 0.1. The initial conditions of two different amplitudes were as follows:

$$q_{low-amplitude} = 6 + 0.1\sin\left(\frac{x}{2.5}\pi\right),\ q_{high-amplitude} = 6 + 5\sin\left(\frac{x}{2.5}\pi\right) \quad (4.8)$$

The computational domain was set as [-5, 5] with uniform spacing. Using the periodic boundary, the waves return to the original place at the non-dimensionalized time, t=100. The upwind function was used as a flux function. The five schemes, which are WENO-JS, WENO-M, WENO-Z, eMLP, and eMLP-VC, introduced above were used for reconstruction methods. Temporal integration was performed using the 3rd-order accurate TVD Runge-Kutta method. A sufficiently small time-step was set, which is 0.001, so the temporal error does not affect the spatial error comparison. The maximum CFL number was 0.06. All results were compared at the non-dimensionalized time, $t = 100$.

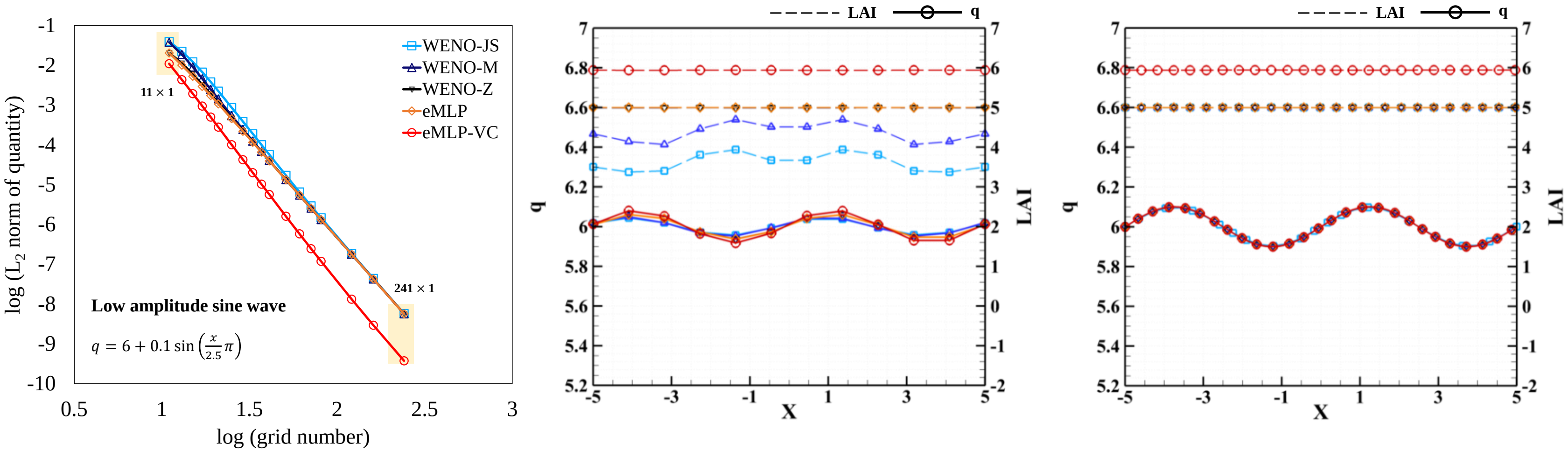

a) Grid convergence test **b) Distribution of quantities ([11×1])** **c) Distribution of quantities ([241×1])**

Fig. 4.2 Results of low amplitude sine wave advection problem.

Figure 4.2 shows the results of the advection problem of a low amplitude sine wave. Fig. 4.2a is the result of the grid convergence test, and global-order-of-accuracy of the schemes can be confirmed. More information on the grid convergence test is given in the table in the Appendix B. Fig. 4.2b and 4.2c are graphs showing the conserved scalar quantity and LAI distribution in coarse and dense grid systems. Even for sinewaves with very small amplitude and small frequency, if the coarse grids are given, the spatial scheme can yield reduced order-of-accuracy. In Fig. 4.2b, WENO-M and WENO-JS produced the reduced order-of-accuracy in all domains. Accordingly, the amounts of sine wave preserved were diminished. On the other hand, in the case of a dense grid system, all schemes have ideal accuracy in all domains. eMLP-VC showed increased order-of-accuracy in all domains thanks to the low Mach number adjustment.

The results of a high amplitude sine wave advection problem are shown in Fig. 4.3 Fig. 4.3a shows the result of the grid convergence test. Fig. 4.3b-f are graphs showing the conserved sine wave and LAI distribution in different grid systems. Since the amplitude of the sine wave is large, most schemes apply numerical dissipation to the sine wave in a relatively coarse grid system. Only WENO-Z on the coarsest grid yields 5^{th}-order accuracy in all domains. Consequently, WENO-Z preserved the scalar quantity the most. Except for WENO-JS, the WENO-type schemes produced ideal results as the grid became denser. On the other hand, WENO-JS did not reach the ideal order-of-accuracy even on the finest grid.

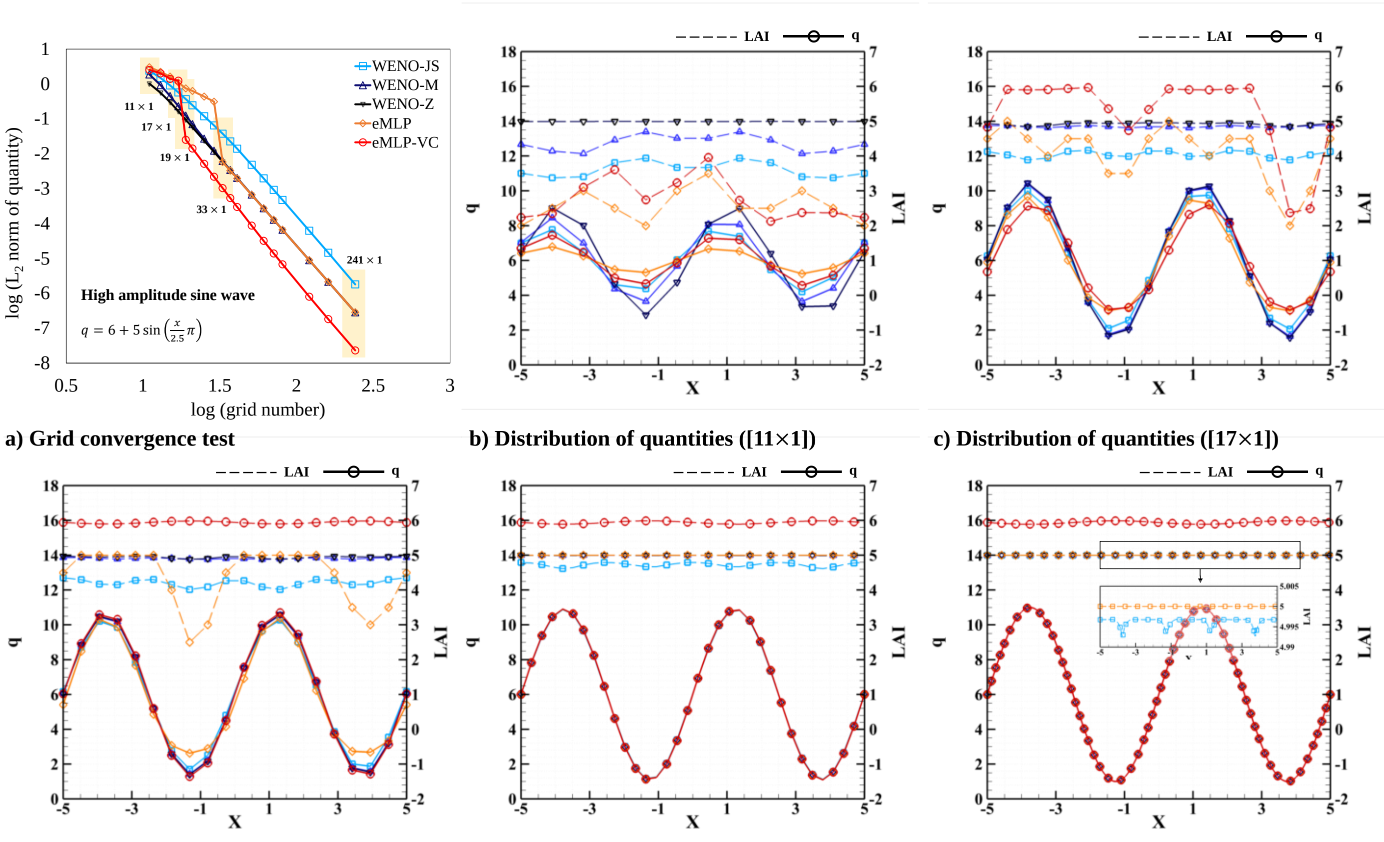

a) Grid convergence test

b) Distribution of quantities ([11×1])

c) Distribution of quantities ([17×1])

d) Distribution of quantities ([19×1])

e) Distribution of quantities ([33×1])

f) Distribution of quantities ([241×1])

Fig. 4.3 Results of high amplitude sine wave advection problem.

The eMLP-type schemes show non-linear results in the grid convergence test. Above a certain grid level, the accuracy increases dramatically, which also can be confirmed through the LAI distribution. When the domain is assessed as a continuous region, the limiting process is not performed, and the accuracy increases sharply. But, when the domain is assessed as a discontinuous region, the limiting process is performed. Then the local-order-of-accuracy is reduced to the first- or second-order locally.

4.3.2 1D Gaussian Pulse Advection

Gaussian acoustic pulse advects in the right direction in this problem. The computational domain is [-5,5] × [-5,5] with equally spaced grids. The initial condition was set as suggested in CAA 1st workshop [59], and can be expressed as follows:

$$q = 0.05 \exp\left(-(ln2)\left(\frac{x}{30}\right)^2\right) \tag{4.9}$$

Considering the domain size, the width and amplitude of the pulse were scaled by 1/10. The performances of the schemes were compared in subsonic (M=0.1) and supersonic (M=1.0) advection speed. The flux function and temporal integration methods were applied in the same way as the 1D sine wave advection problem. A periodic boundary condition was applied so that the pulse can be returned to the original position after a certain period.

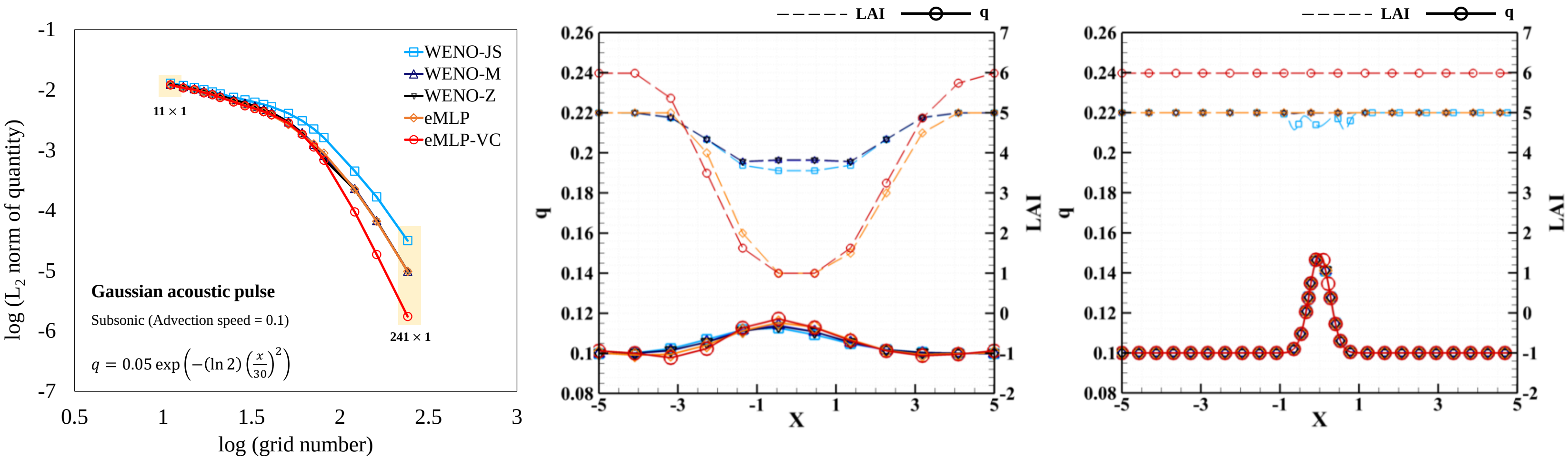

a) Grid convergence test

b) Distribution of quantities ([11×1])

c) Distribution of quantities ([241×1])

Fig. 4.4 Results of gaussian pulse advection problem (subsonic, M=0.1).

In the subsonic case, the solution and initial condition at the non-dimensionalized time, t=100, were compared. Figure 4.4a shows the results of grid convergence test. More information about the grid convergence test is given in Appendix B. Figures 4.4b and 4.4c show the pulse and LAI distribution in each grid system. When the grid is very coarse (see Fig. 4.4b), the low LAI value is widely distributed around the pulse in all five schemes. Numerical dissipation is applied across almost all domains, which leads to very inaccurate results - the denser the grid, the less degradation of local-order-of-accuracy. In the densest grid, all schemes except WENO-JS have ideal accuracy. In the case of WENO-JS, slight degradation of local-order-of-accuracy around the pulse peak remains.

In the case of the supersonic pulse advection problem, the solution and initial condition at the non-dimensionalized time, $t = 10$, were compared. Fig. 4.5 shows the grid convergence test results. The notable difference from the subsonic case is represented in the result of eMLP-VC. eMLP-VC has 5th-order accuracy in all domains as the low Mach number adjustment that was activated during subsonic is deactivated. On the other hand, the WENO-type schemes reconstruct the cell interface quantity independently of advection speed. In other words, the cell interface quantity is reconstructed using only the distribution of the interpolation quantity regardless of flow characteristics. Therefore, the LAI distribution in the supersonic problem is the same in the subsonic.

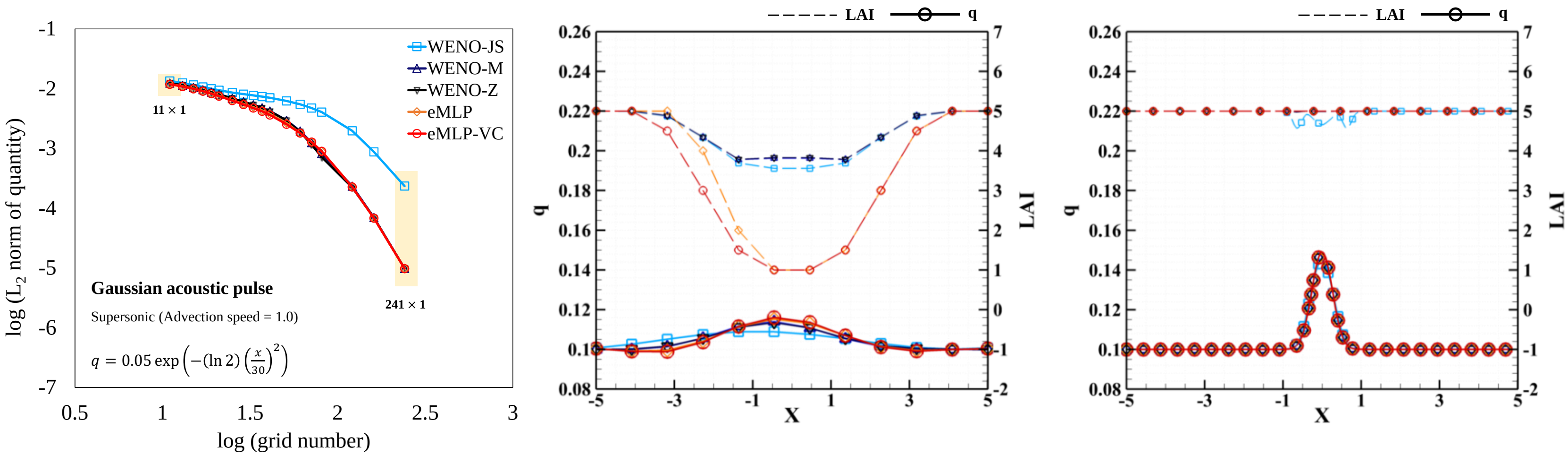

a) Grid convergence test b) Distribution of quantities ([241×1]) c) Distribution of quantities ([241×1])

Fig. 4.5 Results of gaussian pulse advection problem (supersonic, M=1.0).

4.3.3 2D Acoustic Pulse Propagation

The 2D non-isothermal acoustic pulse problem is a benchmark test commonly used in the aeroacoustic field, with the following initial condition:

$$(\rho_0, u_0, v_0, p_0) = [1, 0, 0, 1 + \exp\{-40(x^2 + y^2)\}] \tag{4.10}$$

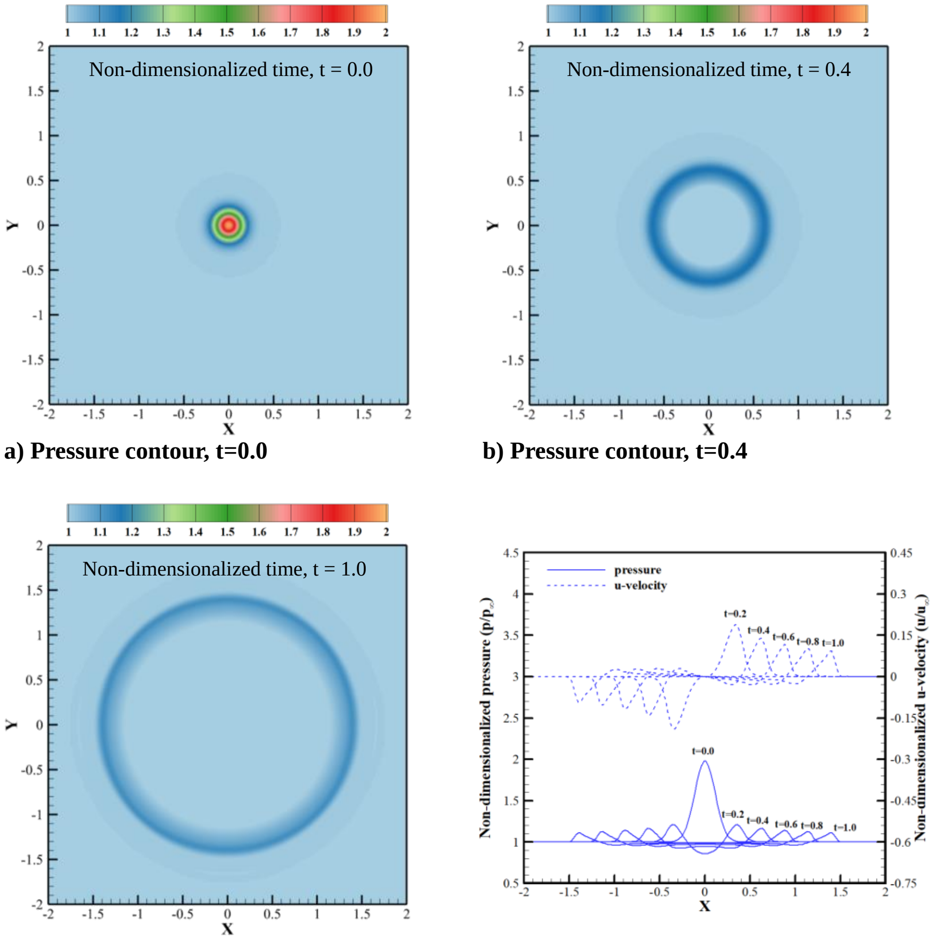

a) Pressure contour, t=0.0

b) Pressure contour, t=0.4

c) Pressure contour, t=1.0

d) Pressure and u-velocity distribution along the y=0 line

Fig. 4.6 Pressure contours and physical quantity distributions of the 2D acoustic pulse test (Grids = [161×161], eMLP-VC).

The 2D non-isothermal acoustic pulse pressure fields at non-dimensional time t = 0.0, 0.4, and 1.0 are shown in Fig. 4.6. The pressure perturbation causes an acoustic wave. As shown in Fig. 4.6d, changes in physical quantities such as pressure, velocity, and density appear over time. For computation, the inviscid and compressible Euler equation was set as the governing equation. The computational domain was composed of [-2,2] × [-2,2] with equally spaced grids; three grid systems were tested, each of which was 41, 81, and 161 grid points in one direction. Calculations were conducted by placing periodic boundaries on all the surfaces. For the convective flux function, local Lax-Friedrich, an upwind-base flux scheme, was used. Characteristic variables are reconstructed using high-order spatial schemes. For temporal integration, the third-order accurate explicit TVD Runge-Kutta method was used. The time-steps of all cases are set to 0.002, where the maximum CFL number is 0.81. It is confirmed that the temporal error does not affect the spatial discretization error.

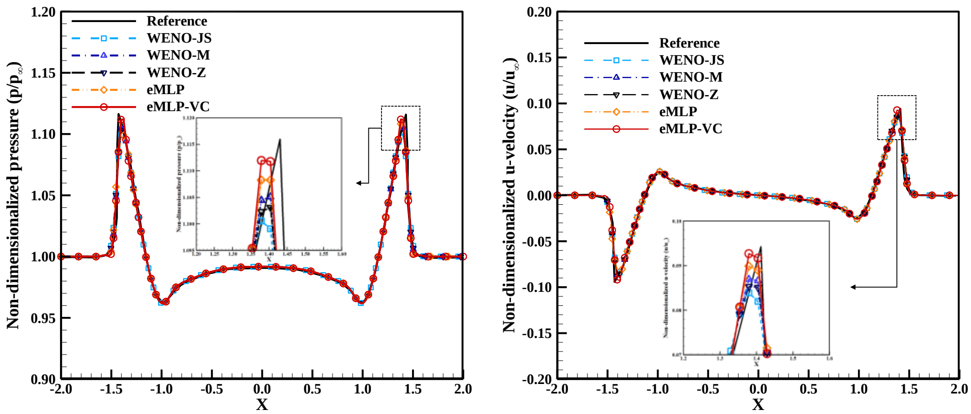

Fig. 4.7 Gaussian acoustic pulse test results
{a) pressure distribution, b) u-velocity distribution}.

The pressure and u-velocity distributions along the y = 0 line of Fig. 4.6c are plotted in Figs. 4.7a and 4.7b, respectively. The numerical dissipation of each scheme can be analyzed by comparing the result of the reference solution [60,61]. The reference solution was obtained through computation with highly dense computation grids consisting of 10^4 points in 1D. Comparing the pressure amplitudes with one another at the non-dimensionalized time, $t = 1.0$, each scheme has 86%, 90%, 89%, 85%, 96% (WENO-JS, WENO-M, WENO-Z, eMLP, eMLP-VC, respectively) relative to the reference value. As an acoustic wave propagates, its intensity decreases while its dissipation increases.

The LAI contours of five schemes are shown in Fig. 4.8. The LAI was calculated using the pressure quantity. Schemes show degradation of local accuracy in the wave front where acoustic pulses propagate. The LAI of WENO-JS drops to 3.43, and that of eMLP drops to 1.50. WENO-M and WENO-Z show higher LAI values, but they still show the degradation of LAI. In other words, the truncation error increases in the wavefront line where the physical quantity changes markedly, thereby lowering the overall accuracy. However, in the case of eMLP-VC ($LAI_{average}$ = 6.00), high-order accuracy is maintained in all domains because all domains are considered to be continuous regions in the flow distinguishing step of eMLP-VC. eMLP-VC performs additional correction in the incompressible region considering the flow characteristics. Because the advection velocity of the Gaussian acoustic pulse flowfield is almost zero in all regions, the accuracy of eMLP-VC can be increased by one order of magnitude in most regions ($LAI_{maximum}$=6.00).

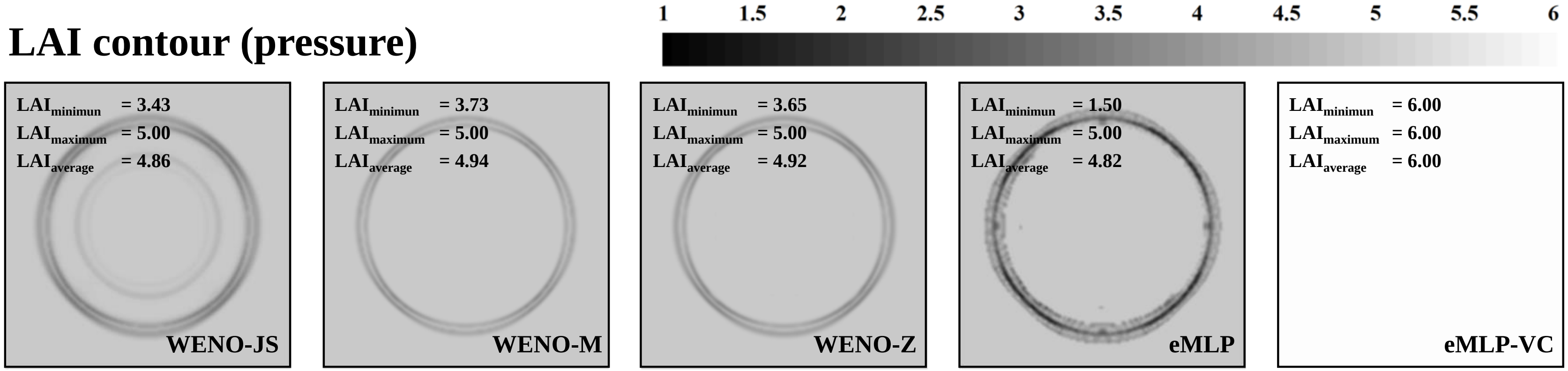

Fig. 4.8 LAI contours of five different schemes (Non-dimensionalized time, $t = 1.0$, LAI of pressure quantity).

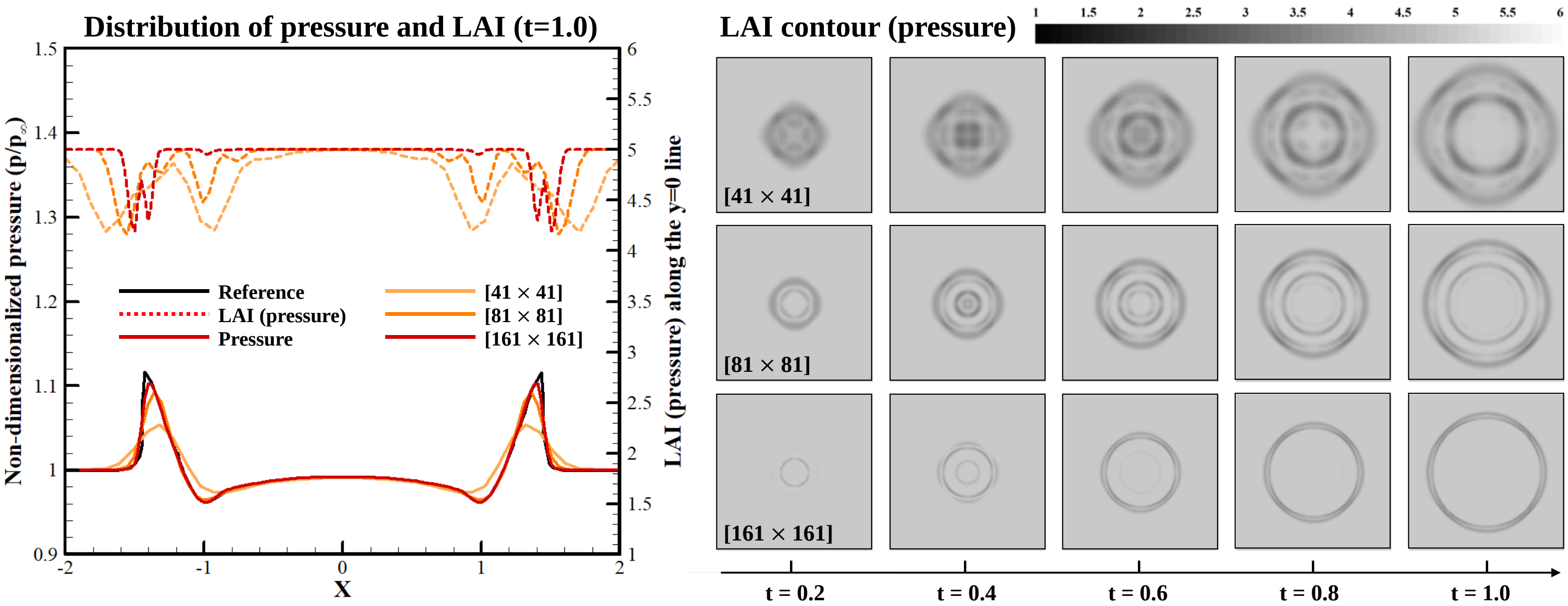

Fig. 4.9 Gaussian acoustic pulse test results with different grid resolutions using WENO-Z scheme.

Figure 4.9 shows the results of the acoustic pulse propagation problem in three grid systems. The pressure and LAI distribution along the $y = 0$ line at $t = 1.0$ are shown in Fig. 4.9a. The LAI contours over time using WENO-Z are represented in Fig. 4.9b. Though not shown in this paper, and the rest of the schemes show similar results. The degradation of local-order-of-accuracy decreases as the grid becomes denser, and the amount of preserved acoustic pulse increases accordingly. The gradients are steep in the wavefront so that local degradation occurs even when the fine grids are applied.

4.3.4 2D Isentropic Vortex Advection

Because the representative source of rotorcraft aeroacoustic noise is one of vortex interaction, vortex preservation and capturing the interaction with slight numerical dissipation are essential elements for accurate noise prediction. The isentropic vortex advection problem was selected as the 2D benchmark test, with the following initial condition:

$$(\rho_0, u_{\theta,0}, u_{r,0}, p_0) = \left[\left\{1 - \frac{\gamma_v - 1}{2} M_v^2 e^{[1-r_v^2]}\right\}^{\frac{1}{\gamma_v - 1}}, M_v r_v \exp\left[\frac{1-r_v^2}{2}\right], 0, \frac{\rho_0^{\gamma_v}}{\gamma_v}\right] \quad (4.11)$$

where $u_{\theta,0}$ and $u_{r,0}$ represent the initial tangential and radial velocities, respectively. The vortex Mach number, M_v is 0.39. r_v is the distance from the vortex core $(x, y) = (0,0)$. The gas constant, γ_v, is 1.4. Flowfields dominated by aeroacoustic noise consist of the interaction of numerous large and small vortices. To preserve them all, an effective grid system must be constructed. In addition, to observe the characteristics of the scheme in terms of the advection speed of the vortex, four different speeds were compared, from subsonic to supersonic. The computational domain is [-5,5] × [-5,5] with equally spaced grids. A grid convergence test was conducted. The coarsest grid system had 11 grids in one direction, and the finest grid system had 161 grids in one direction. Calculations were conducted by placing periodic boundaries on all the surfaces.

The 2D inviscid Euler equation was set as the governing equation to compare only the dissipation of the numerical scheme. The convective flux function was local Lax-Friedrich, upwind function. Characteristic variables are reconstructed using high-order spatial schemes. For temporal integration, the third-order accurate explicit TVD Runge-Kutta method was used. The time step of all cases was set to 0.001, and the maximum CFL number was 0.425. A total of four tests were conducted with an advection Mach number M_{∞} = 0.1, 0.25, 0.5, and 1.25. The vortex moves in +y direction. All computational results were compared with the initial value at the time at which the vortex first returned to the domain.

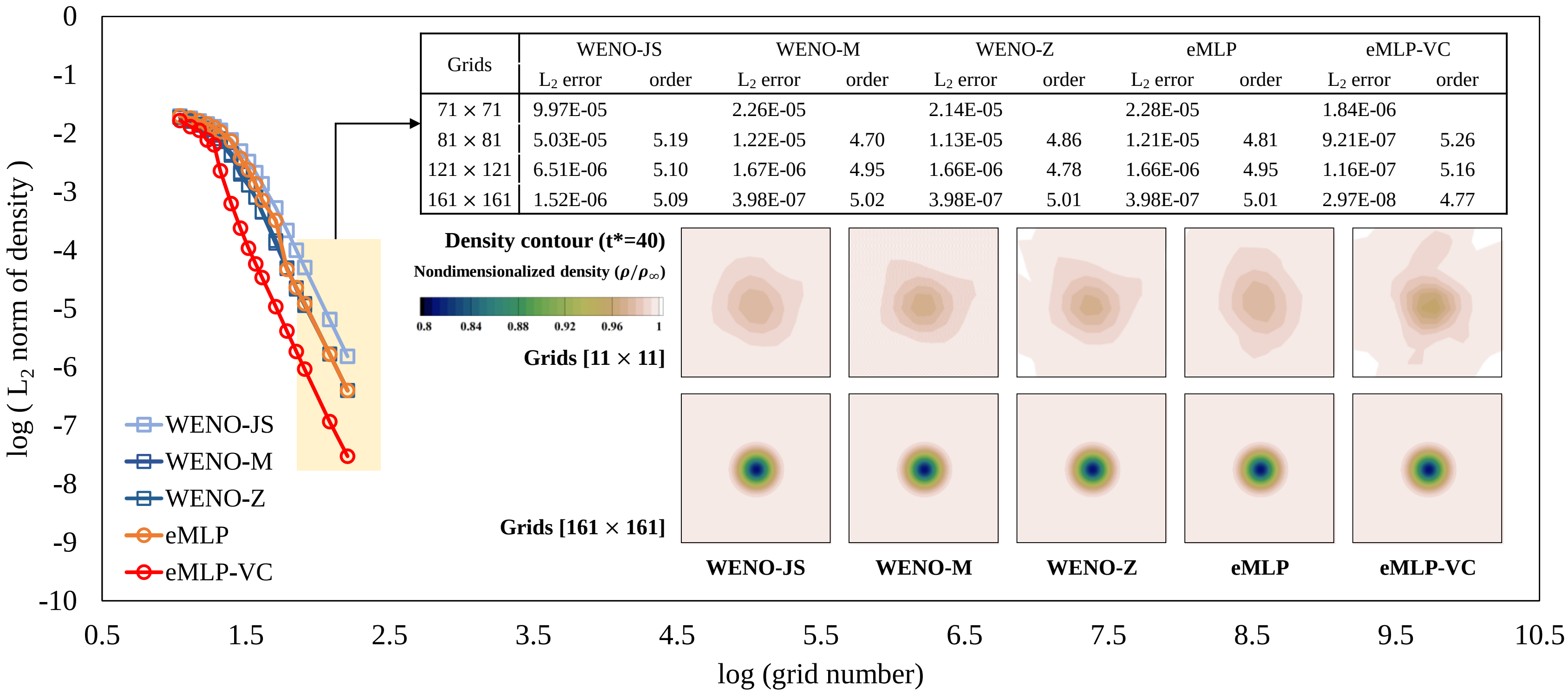

Grids	WENO-JS		WENO-M		WENO-Z		eMLP		eMLP-VC	
	L_2 error	order	L_2 error	order	L_2 error	order	L_2 error	order	L_2 error	order
71 × 71	9.97E-05		2.26E-05		2.14E-05		2.28E-05		1.84E-06	
81 × 81	5.03E-05	5.19	1.22E-05	4.70	1.13E-05	4.86	1.21E-05	4.81	9.21E-07	5.26
121 × 121	6.51E-06	5.10	1.67E-06	4.95	1.66E-06	4.78	1.66E-06	4.95	1.16E-07	5.16
161 × 161	1.52E-06	5.09	3.98E-07	5.02	3.98E-07	5.01	3.98E-07	5.01	2.97E-08	4.77

Fig. 4.10 Results of 2D isentropic vortex advection problem at advection Mach number, M=0.25 (grid resolution test, global-order-of-accuracy, and density contours).

The global-order-of-accuracy obtained through the grid convergence test is shown in Fig. 4.10. More information on the grid convergence test is given in the table in the Appendix. Density contours in the coarsest and finest grids are also presented. When there are more than 121 grids in one direction, WENO-M, WENO-Z, and eMLP all have the same error level. In other words, all three schemes have exactly 5th-order accuracy in the entire domain. In the case of WENO-type schemes, the WENO-M and WENO-Z schemes with weights adjusted to reduce the decrease in accuracy at critical points demonstrate higher accuracy than the WENO-JS. On the other hand, in WENO-JS, global-order-of-accuracy converges to 5. Still, the error of WENO-JS is larger than that of other high-order accurate schemes because of the degradation of local accuracy. In the case of eMLP-VC, the vorticity preserving capability is the highest in all grid systems. The low Mach number adjustment effect activated in the subsonic region minimizes degradation of local accuracy. Also, the flow distinguishing step of eMLP-VC is set appropriately for the vortex flow, so it shows good performance than eMLP.

The density distributions of the isentropic vortex advection problems are shown in Fig. 4.11. The test results for three grid systems are shown, and the LAI contours for each grid system are also presented. The coarse grid system has 11 grids in one direction, equivalent to having two grids inside the vortex core. The medium grid system has 21 grids in one direction, equivalent to four grids inside the vortex core. The fine grid system has 161 grids in one direction, equivalent to 32 grids inside the vortex core.

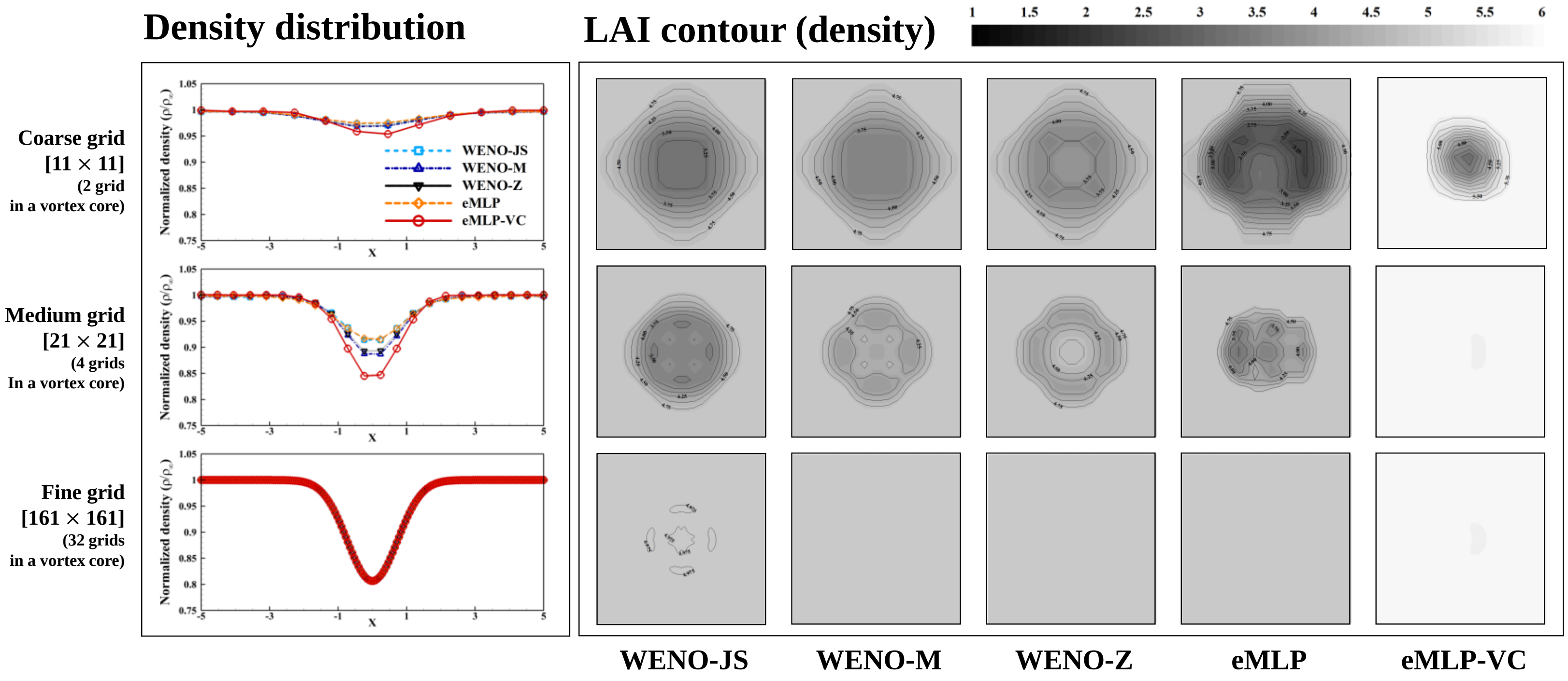

Fig. 4.11 Comparison of the LAI and density in three different grid systems at $M_\infty = 0.25$.

Ideal order-of-accuracy is expected for all domains because the isentropic vortex is a physically continuous flow. However, in the discretized domain, ideal order-of-accuracy is not applied, as shown in Fig. 4.11. The LAI of eMLP-VC is larger than those of other schemes. This is because eMLP-VC assesses the whole computational domain as continuous, and consequently, local accuracy is maximized through low Mach number adjustment. In the case of eMLP, the limiting function was applied locally as the vortex core region was assessed to be discontinuous. WENO-type schemes have different error distributions from eMLP-type schemes. While eMLP has a reduced accuracy in the vortex core region, WENO-type schemes show lower accuracy in the area surrounding the vortex core. This is because WENO-type schemes partially adjust the polynomial weights in a place where the slope changes significantly. Nevertheless, because WENO-M and WENO-Z use the mapping and global smoothness indicator methods, respectively, the LAI of both schemes is higher than that of WENO-JS. Consequently, local accuracy degradation is lowered in WENO-M and WENO-Z.

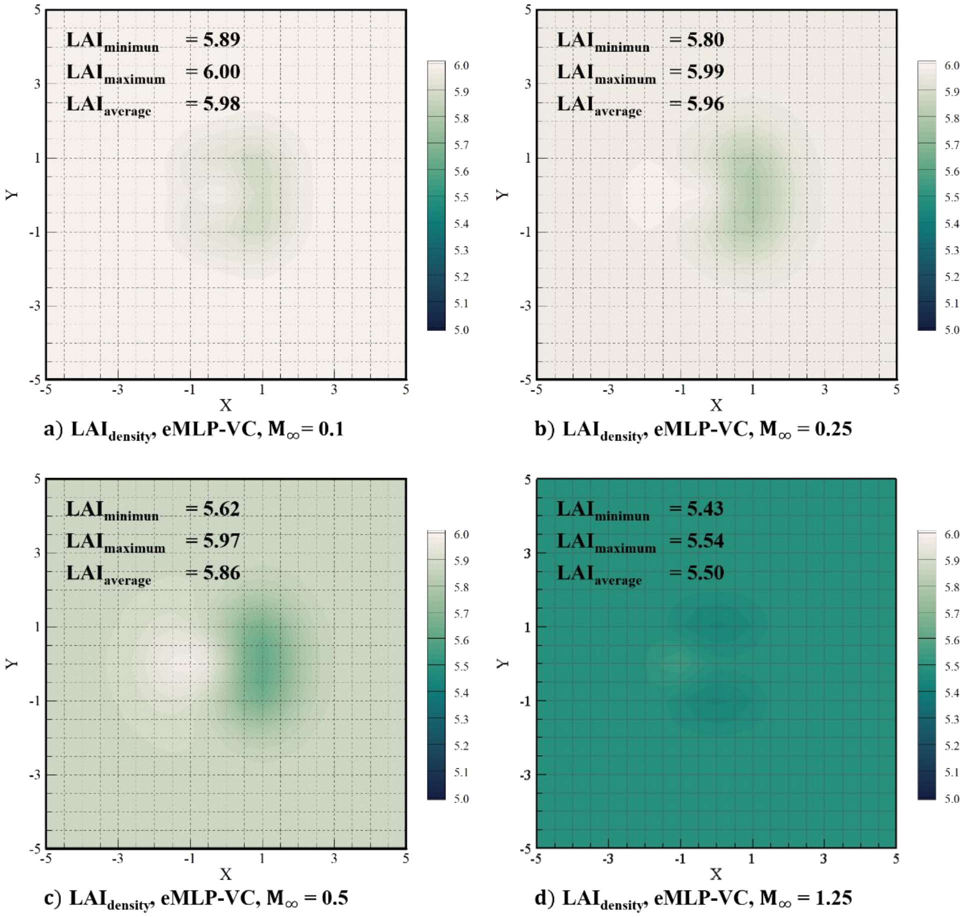

a) LAI$_{density}$, eMLP-VC, M_∞= 0.1

b) LAI$_{density}$, eMLP-VC, M_∞ = 0.25

c) LAI$_{density}$, eMLP-VC, M_∞ = 0.5

d) LAI$_{density}$, eMLP-VC, M_∞ = 1.25

Fig. 4.12 Local-order-of-accuracy index (LAI) of eMLP-VC for four different Mach numbers.

eMLP-type schemes use physical quantities such as pressure and density to distinguish the flowfields and apply different reconstruction methods. Furthermore, in the case of eMLP-VC, additional reconstruction is performed for low Mach numbers. Hence, local accuracy varies according to the advection Mach number. Figure 4.12 shows the LAI of eMLP-VC for four different speeds. The LAI of eMLP-VC decreases as the speed increases. At $M_\infty = 0.1$, to increase the accuracy, eMLP-VC reconstructs the cell interface quantity in a form similar to that of the central difference. At $M_\infty = 1.25$, eMLP-VC uses an upwind form to maintain the robustness in compressible flow. Using low Mach number adjustment, eMLP-VC compensates for the decrease in accuracy in the incompressible flow, which is a drawback of the upwind-type flux function. Since the vortex rotates counter-clockwise, eMLP-VC yields a lower LAI on the right side of the vortex core. Conversely, on the left side of the vortex core, the rotation and the advection are in opposite directions, resulting in a higher LAI.

4.4 Main characteristics essential for high-resolution rotorcraft flowfield

Using one- and two-dimensional benchmark tests, the variation in the conservation of physical quantities from scheme-to-scheme was confirmed. This variation in conservation is mainly due to two scheme characteristics.

First, different types of function of smoothness (FoS) inherent in each scheme have a significant influence on the local accuracy. FoS plays a role in changing the stencil weights (c) locally. In WENO-type schemes, FoS is applied as a smoothness indicator and a weighting algorithm. In eMLP-type schemes, FoS is applied as an independent flow-distinguishing step and a limiting function. FoS is necessary to address discontinuities caused by compressible flow, but it must be activated elaborately because it can cause a decrease in local accuracy in a region where there is no discontinuity. In particular, FoS should carefully distinguish numerical discontinuities owing to the coarse grid in the continuous region and real physical discontinuities such as shocks. The FoS performances of WENO-M and WENO-Z are better than that of WENO-JS. Moreover, the FoS performance of eMLP-VC is better than that of eMLP, as observed in the results of the 2D benchmark tests.

Second, hybrid central-upwind type characteristics are required. Among the five schemes, the scheme that exhibits hybrid central-upwind characteristics is eMLP-VC, which has high LAIs in the benchmark problems. The physical quantities are preserved the most in eMLP-VC case. In the incompressible area, the upwind characteristics of the flux function are trivial because discontinuities such as shocks do not occur. Because the dissipation and dispersion errors of the numerical scheme are less in the central-type scheme than in the upwind-type scheme, it is preferable to preserve a physical quantity by applying the central type-based scheme in the incompressible area. The low Mach number adjustment applied to eMLP-VC is designed to exhibit hybrid central-upwind characteristics. This adjustment can be applied to any upwind-type scheme that requires the left and right states of the cell interface quantity. Therefore, it has a desirable effect when applied to any upwind-type scheme.

Chapter 5. Applications: Numerical Investigation and Design Exploration of Rotorcraft

The developed eMLP-VC was applied to actual rotorcraft flowfield analysis. Three cases related to UAM eVTOL aircraft flow fields were selected. The main objective of this chapter is to determine whether the eMLP-VC is robust and efficient for achieving high accuracy in real-world flow fields. Also, it will be important to determine whether the aerodynamic performance can be accurately predicted even without a sufficient number of grids in the case of complicated flow conditions. The details of three cases are as follows:

1. First, the propeller-wing interaction model (PROWIM), in which the propeller and wing interaction effect is dominant, was analyzed. The wake generated by the propeller interacts with the wing, which results in the fluctuation of the airloads. It is important to accurately capture the amount of pressure fluctuation in the wing generated by the interaction, as it also affects the vibration and noise performance of the entire aircraft.

2. As the second test, the Second Higher-Harmonic Control Aeroacoustic Rotor Test (HART-II) was selected. Though HART-II rotor is not an example of UAM eVTOL aircraft, HART-II rotor is appropriate to test the performance of the numerical scheme due to two facts: 1) the BVI interaction commonly seen in UAM eVTOL aircraft is dominant in HART-II flow field, 2) Many researchers have been studied the HART-II rotor and resulted that the spatial discretization scheme is

important for BVI to be captured accurately. The strength of the vortex generated at the tip must be accurately maintained, and the interaction between the vortex and the blade must be captured robustly. In particular, the strength of the vortex that collides with the wing becomes weaker towards the inboard, and it is important to preserve these vortexes well for interaction.

3. Finally, co-rotating coaxial rotor for UAM eVTOL aircraft was designed. By using multiple propulsors in UAM eVTOL aircraft, it is possible to use coaxial rotors rotating in the same direction in one rotor system. By optimizing the rotor using several design variables such as vertical spacing, index angle, and pitch angle, aerodynamic performance can be maximized. The design exploration was conducted using high fidelity RANS solver with high-order spatial discretization scheme, eMLP-VC. In addition, detail analysis was performed on the optimal configuration. It was possible to capture complex vortex dynamics including vortex breakdown and vortex pairing, which could only be seen by using denser grids.

5.1 Propeller-Wing Interaction (PROWIM)

PROWIM configurations of wing-nacelle-propeller shown in Fig. 5.1a were tested at Delft University of Technology [62] for analysis of the propeller-wing interaction. The wing has a rectangular shape with aspect ratio=5.33, which is untwisted, untapered, and uses the NACA 64-2-015A airfoil. The NACA 5868-9 propeller, which has four blades with Clark-Y airfoil, was used. The pitch angle of the propeller at 0.75R was fixed at 25 degrees, and NACA report 640 (1938) was referenced [63]. The wing incident angle was 4°, and the propeller rotated counter-clockwise. Two cases of prop-on and prop-off conditions were analyzed. The freestream Mach number was M=0.14, and the Reynolds number was $Re = 0.8 \times 10^6$.

In case of the prop-off condition, a steady analysis was carried out, and the convergence speed was accelerated by using the local time stepping method. In contrast, the prop-on condition was solved using an unsteady solver. The time integration was conducted using a second-order backward difference formula and a dual time stepping method. The timestep of the entire domain was an azimuth angle interval of 1° per step. The time accuracy was improved by performing 10 dual time-stepping analyses at each physical timestep. The grid system is shown in Fig. 5.1b. The wing and propeller (without a nacelle) were simulated using the overset grid system [35]. The propeller blade had 241×165×81 (chordwise×spanwise×normal) O-type grids. The background grids including the wing configuration had 48 million grids. The background grids extended approximately 100 wing chord length in all directions. The grids were clustered near wing and wake region with spacing of 0.1 blade chord length. The first grid spacing in the normal direction was set to $y+=1$ based on the blade tip for being able to accurately predict the velocity distribution inside the boundary layer.

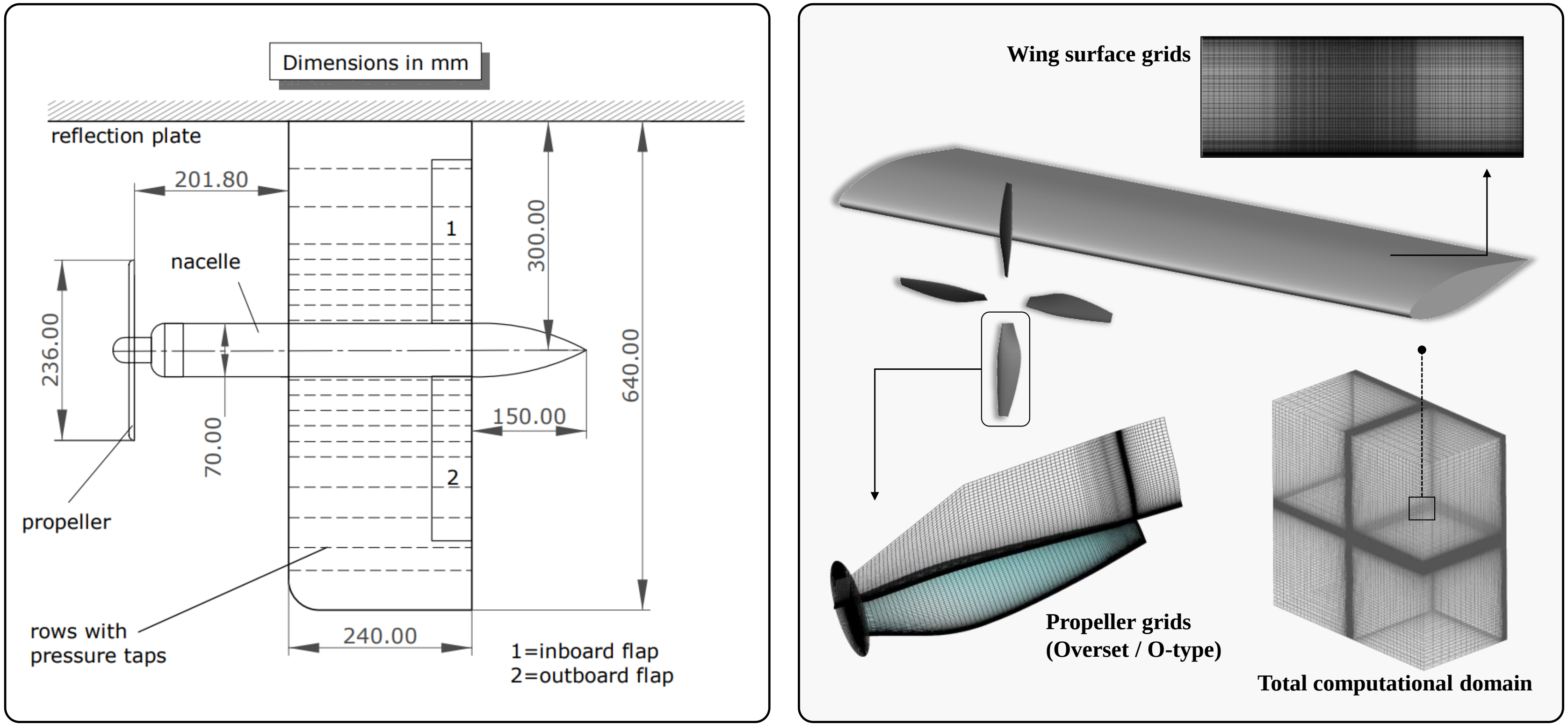

a) Dimensions of PROWIM configuration **b) Grid system for PROWIM**

Fig. 5.1 Experimental and computational configuration for PROWIM (propeller grids: 241×165×81, background grids: 48 million).

Fig. 5.2 shows the normal force distribution of the wing, comparing CFD and experimental values for the prop-on and prop-off cases. The results of the CFD solver reflect the experimental data accurately. In the prop-off case, the CFD result in the nacelle region overpredicts the experimental value, but in other areas the CFD makes accurate predictions. The normal force difference between the prop-off and prop-on cases occurs due to the influence of the wake. While the second-order accurate TVD monotone upstream-centered scheme for conservation law (MUSCL) limiter eliminates most effects of the wake due to the excessive numerical dissipation, the high-order accurate eMLP-VC and WENO, which have relatively low numerical dissipation, can capture the fluctuations in the aerodynamic loads. Tip vortices and secondary vortices generated by the propeller blades interact as they pass through the wing. The pressure fluctuation caused by the wake-propeller interaction is dominant at 28% and 64% wing span, as shown in Fig. 5.2. The results using TVD MUSCL limiter show no vortex effect, while the results using eMLP-VC and WENO show that a vortex interacts with the wing surface. Changes in the normal force due to the wingtip vortex can also be seen only in the high-order accurate eMLP-VC and WENO results.

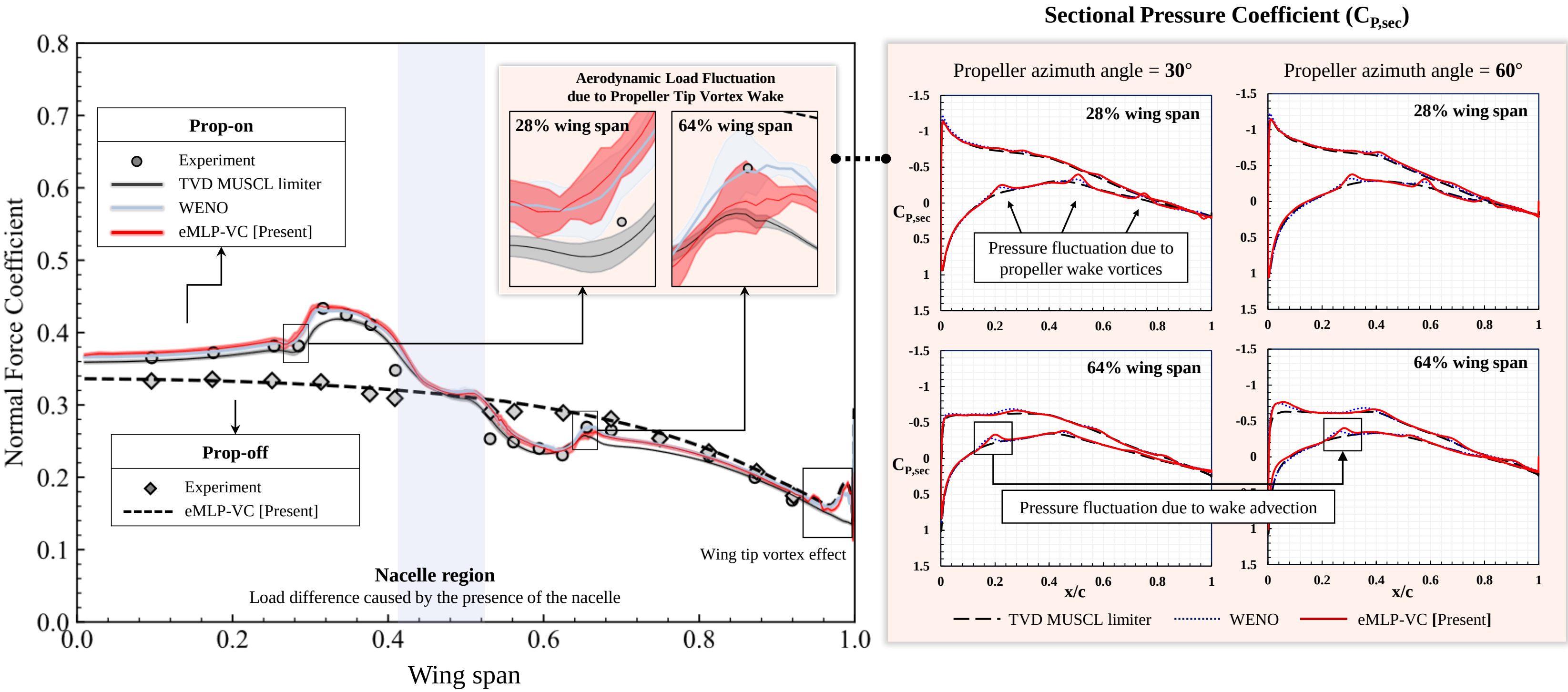

Fig. 5.2 Sectional normal force and sectional pressure coefficient of PROWIM ($\alpha_{wing} = 4°, M = 0.14, Re = 0.8 \times 10^6$).

Figure 5.3 shows the schematic of the PROWIM flowfield and the vorticity magnitudes of the propeller wake and wing tip vortex. The vorticity strength of the propeller wake was evaluated in the section located at 0.42R (R is the propeller radius), as indicated by the AA' plane in Fig. 5.3b. In case of the wing tip vortex, the evaluation was made in the BB' plane located at 1.35R in the wake direction from the trailing edge of the wing as shown in Fig. 5.3c. The TVD MUSCL limiter and WENO preserved the tip vortices but could not describe the behavior of the secondary vortices and vortex sheets, which have relatively small vorticities. In the case of eMLP-VC with high vortex preserving capability, the vortex sheets and secondary vortices were preserved along with the tip vortices and their interactions. In particular, it preserved the effect of the secondary vortices on the tip vortex and the subsequent dynamical changes. This preservation of the wing tip vortex confirms that eMLP-VC has more advanced vortex preserving capability than the TVD MUSCL limiter and WENO. When normalized by the vorticity magnitude of eMLP-VC, WENO preserves only 55% and the TVD MUSCL limiter preserves only 24%.

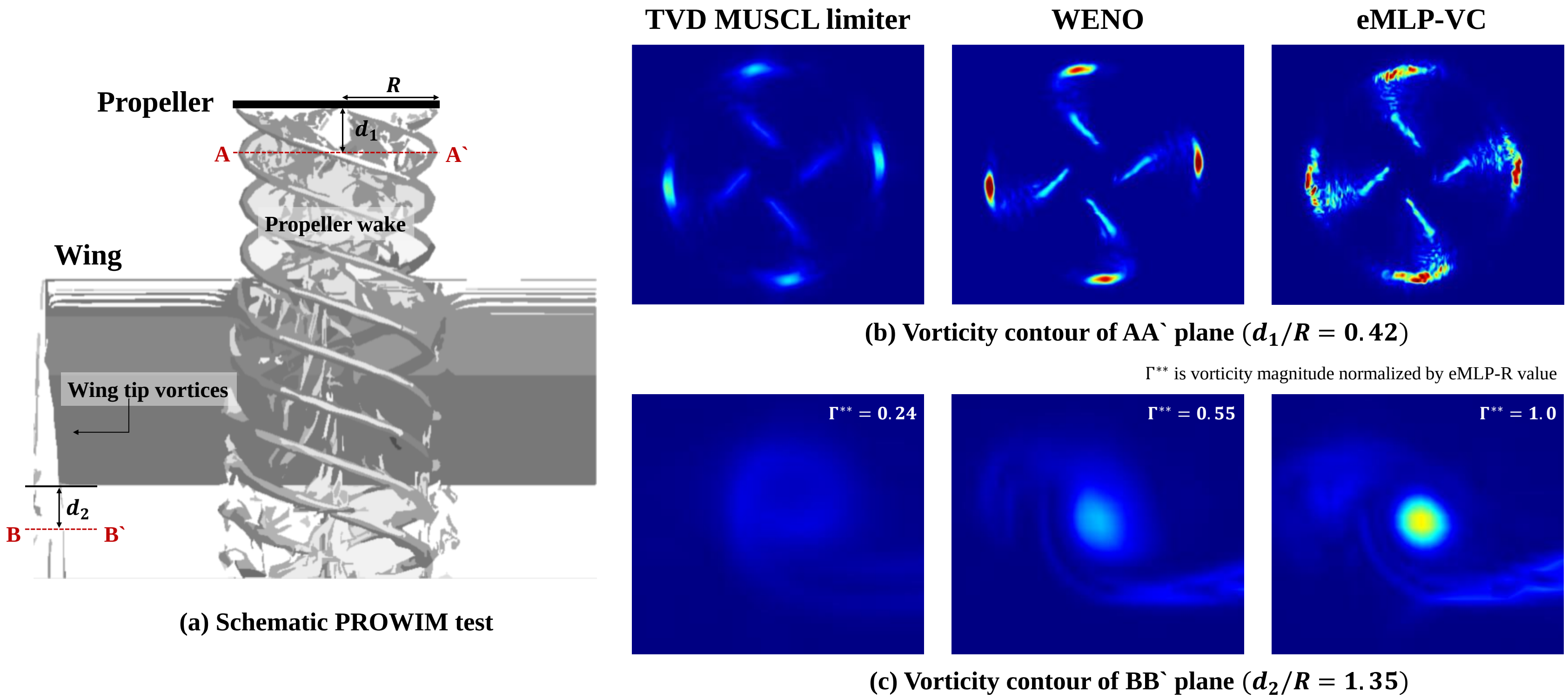

(a) Schematic PROWIM test

(b) Vorticity contour of AA` plane ($d_1/R = 0.42$)

(c) Vorticity contour of BB` plane ($d_2/R = 1.35$)

Fig. 5.3 Vorticity contour of wake and wing tip vortices.

Figure 5.4 shows the propeller-wing interaction through the iso-surface visualization method based on the rortex. The upper and side views of PROWIM flowfields analyzed by five different schemes (TVD MUSCL limiter, WENO, MLP, eMLP, eMLP-VC) are described. The amount of numerical dissipation of five schemes can be indirectly assumed. Rortex is a parameter used for visualizing vortices, and it can effectively distinguish rotational vortices from non-rotational sources, such as shear layers, discontinuity structures, and non-physical structures [64,65]. The rortex used in Fig. 5.4 is defined in the same as it is in Xiangrui Dong et al. [64]. The non-dimensionalized rortex (Ω_R) is 0.75.

All high-order accurate WENO, MLP, eMLP, and eMLP-VC methods describe the interaction between the strongest tip vortices and the wing. The tip vortices are preserved up to the trailing edge of the wing, and they simultaneously affect the pressure distribution of the wing. Secondary vortices with relatively weak vorticities are modeled only by eMLP-VC. These secondary vortices change the behavior of the tip vortices and convect and interact with the wing. The TVD MUSCL limiter, on the other hand, has difficulty in preserving the tip vortices due to excessive numerical dissipation. The vortices dissipate the moment they first interact with the wing.

The flowfield can be classified by using the distinguished criterion embedded into eMLP and eMLP-VC, as shown in Fig. 5.4. The flowfield is divided into continuous, linear discontinuous, and nonlinear discontinuous regions (colored in white, gray, and black, respectively).

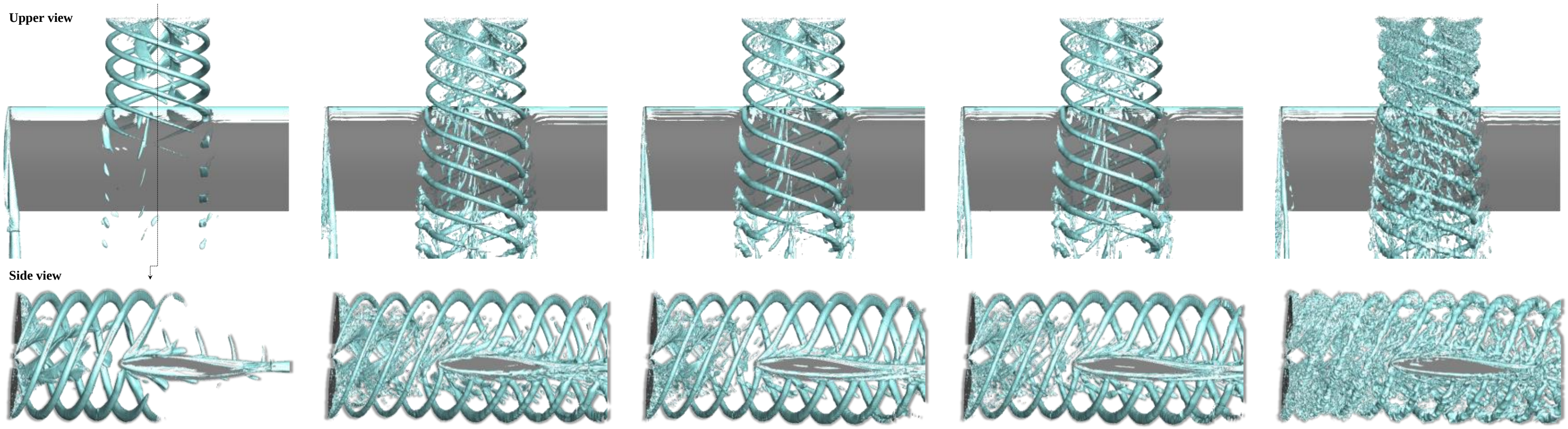

(a) TVD MUSCL limiter (b) WENO (c) MLP (d) eMLP (e) eMLP-VC

Fig. 5.4 Flowfield of PROWIM using iso-surface visualization method (rortex, $\Omega_R = 0.75$).

The planes for comparison are 0.08R and 0.42R away from the front of the propeller. The wake area of the propeller is a region where only vortex-vortex interaction exists, and because there is no discontinuous phenomenon such as shock or rarefaction wave, it should be considered a continuous region. However, as shown in Fig. 3.2, the original distinguishing criterion can consider the vortex flow as discontinuous when there are insufficient grid points to describe the vortex profile properly. In a discretized domain, abrupt variation in the velocity vector can be seen as discontinuous, though the vortex flow is not a discontinuous flow. Likewise, in PROWIM calculation, most of the vortex-dominated wake regions are considered as discontinuous regions when using the original distinguishing criterion in eMLP as shown in Fig. 5.5. The limiting process is applied in these areas, resulting in unwanted numerical dissipation and low-resolution results. In contrast, when using the modified distinguishing criterion in eMLP-VC, most of the wake regions are considered as continuous regions due to the exclusion of the velocity vector in the distinguishing mechanism. Especially in the plane 0.42R away from the front of the propeller, all regions are considered as continuous regions. No undesirable limiting process is employed in most of the wake regions, which prevents numerical dissipation and enhances the accuracy of the simulated flowfields. As can be seen from the vorticity contours in Fig. 5.3, the behavior of the secondary vortices and their interaction with the tip vortices can be explained as a consequence of the increased vortex preserving capability.

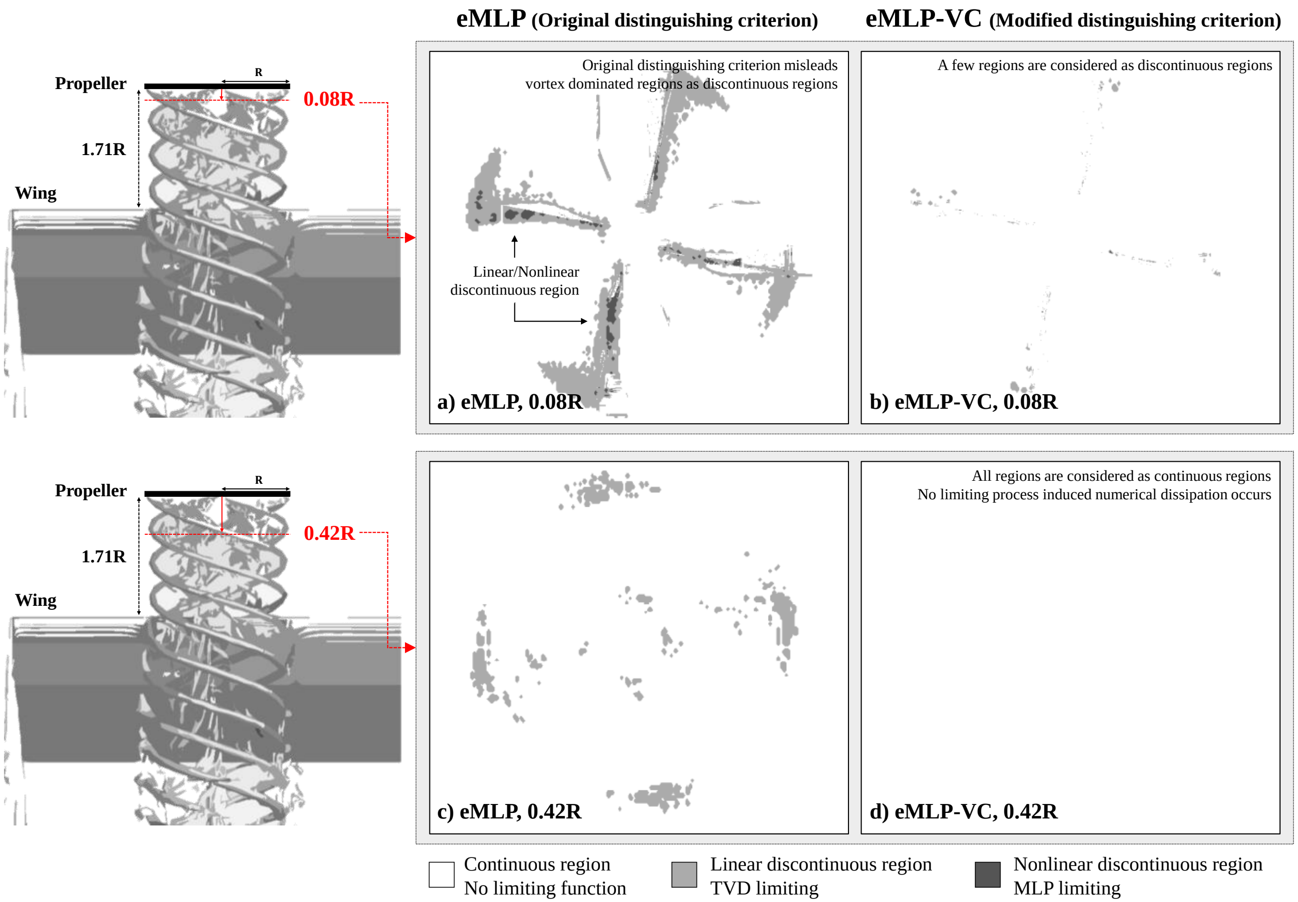

Fig. 5.5 Smoothness contour of front plane of the propeller classified according to the distinguishing criterion.

5.2 Numerical investigation: Descent flight (BVI, HART-II)

The HART-II blade was tested under several descending flight conditions, in which the BVI was significant. Because aerodynamic load fluctuation and noise generation through vortex interaction mainly occur, the HART-II problem is suitable for observing the effect of the local error of spatial discretization schemes on aeroacoustic predictability. For simulation, aerodynamic and structural analyses were performed using the CFD-computational structural dynamics (CSD) loose coupling method. Loading and thickness noise were calculated through acoustic analogy using the Ffowcs Williams and Hawkings (FW-H) equation. The experimental condition used in this study was a baseline case with an advance ratio of 0.15, a hover tip Mach number of 0.639, and a precone angle of 2.5°. In the HART-II experiment, the shaft tilt angle was 5.3°, but 4.5° was used to account for wind tunnel effects. For details on the HART-II experiment, please refer to Smith et al. [28]. A HART-II fuselage facilitates the prediction of the intensity and phase of BVI on the advancing side but not on the retreating side. Therefore, in this study, the aerodynamic and noise prediction ability of the spatial discretization scheme was efficiently compared using an isolated rotor without a fuselage.

5.2.1 CFD-CSD Loose Coupling

The Comprehensive Analytical Model of Rotorcraft Aerodynamics and Dynamics II (CAMRAD II) [66] was used for CFD-CSD loose-coupling analysis to model the flexibility of the blades. CAMRAD II models the elastic blade using nonlinear finite elements, the control system in multibody dynamics with finite elements, and the rotor aerodynamic environment based on second-order lifting line theory, including various physical models of inflow, wake, and unsteadiness. These interdisciplinary techniques are coupled and provide complete trim and transient solutions. Loosely coupled with the CFD solver, CAMRAD II provides a trimmed state of the blade that combines the control angle, dynamic motion, and elastic deformation. The CFD solver receives this information, performs a new analysis, and sends the updated aerodynamic loads back to CAMRAD II. In this way, several iterations of analysis are conducted until the aerodynamic loads from the CFD and CSD solver are the same. The overall CFD-CSD loose coupling algorithm and convergence history are shown in Fig. 5.6. After seven iterations, the converged solution that accounts for the aerodynamic forces and moments was acquired in this study.

The details of the CFD solver are as follows. For the time integration method, a second-order backward difference formula with dual time stepping was used. The matrix inversion was efficiently performed through the DADI method. The size of the physical timestep was an azimuth angle of 0.2° with 20 dual time step sub-iterations. The local time stepping method was conducted during the process of dual time stepping to accelerate the convergence. The initial CFD solution was obtained from the calculation result of three rotor revolutions; 1.25 rotor revolutions were calculated by restarting from the previous data for every CFD-CSD coupling iteration.

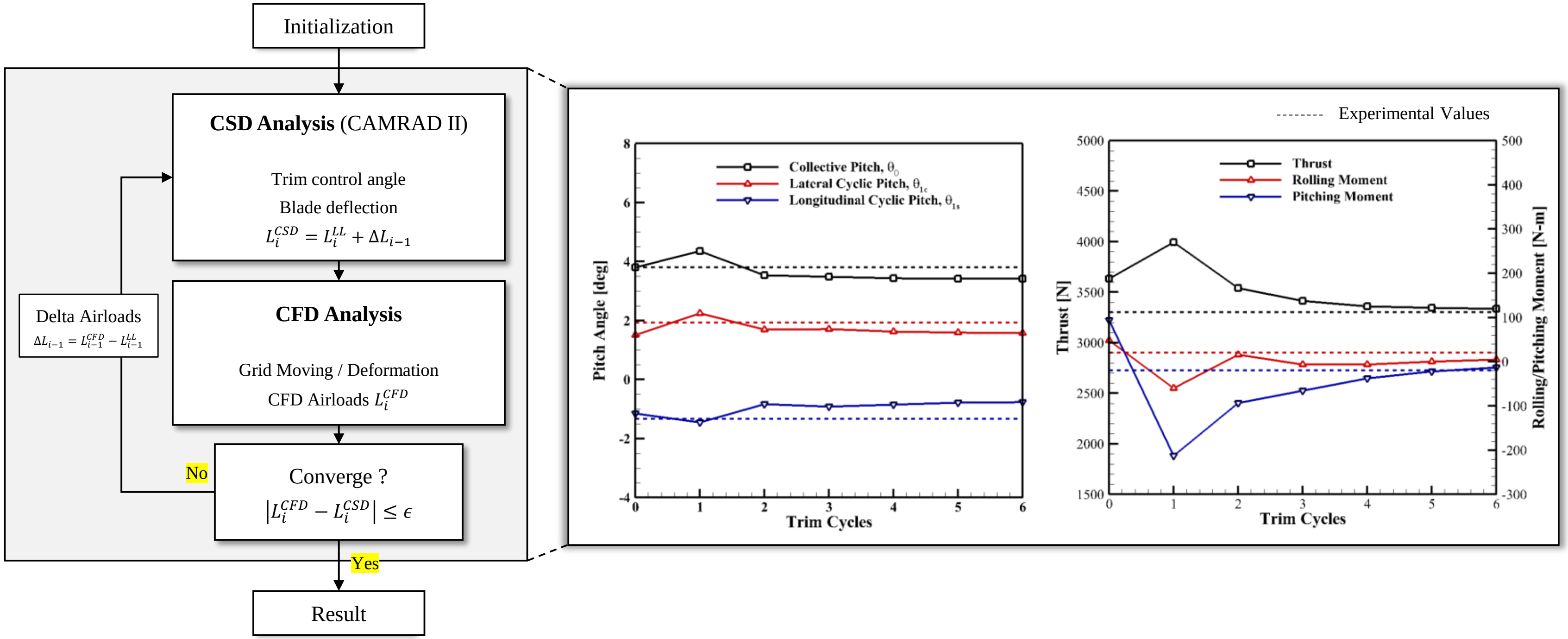

Fig. 5.6 CFD-CSD loose coupling algorithm and iteration history.

The grid system used for the analysis is shown in Fig. 5.7. The rotational motion of the rotor was simulated through the overset grid system. The size of the grid of one blade was 346×115×35 (chordwise×spanwise×normal) in C-H type. The first grid spacing in the normal direction was 1×10^{-5} times the chord length; this allowed the velocity distribution inside the boundary layer to be accurately modeled. The background grids were 21.4 million, with 15% chord spacing in the near-body grid.

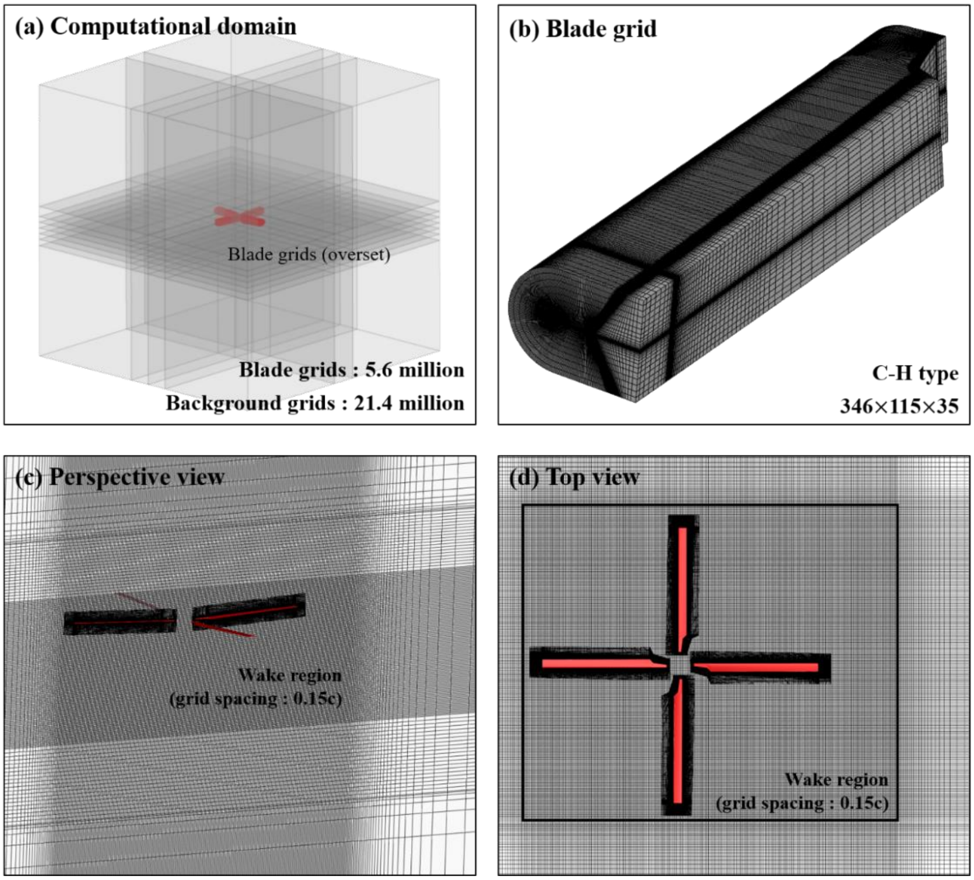

Fig. 5.7 Overset grid system of HART II.

5.2.2 Acoustic Analogy

The KR-Noise (Korea Aerospace Research Institute Rotor-Noise) solver [67] was used to predict the noise generated by the rotor blades. It is a tonal noise prediction solver that uses the Farassat Formulation 1A equation based on the FW-H equation [68]. Loading and thickness noise are considered. A source-time-dominant algorithm was used to consider sound wave propagation speed and the arrival distance. The noise is calculated using the unsteady aerodynamic loads of the trimmed solution.

5.2.3 Aerodynamic Results

Figure 5.8 shows the LAI and the vorticity contours in a plane 1.0 chord up from the rotor disk plane. The LAI was calculated using the density quantity. Similar patterns were found in LAIs calculated using pressure and velocity fields (not shown in this paper). The vortices generated by the rotor blades interact with each other, as observed in the vorticity contours. Tip vortices with a relatively strong vorticity are well-simulated in all five schemes. However, vortices generated from the root dissipate rapidly in WENO-JS due to their relatively weak vorticities.

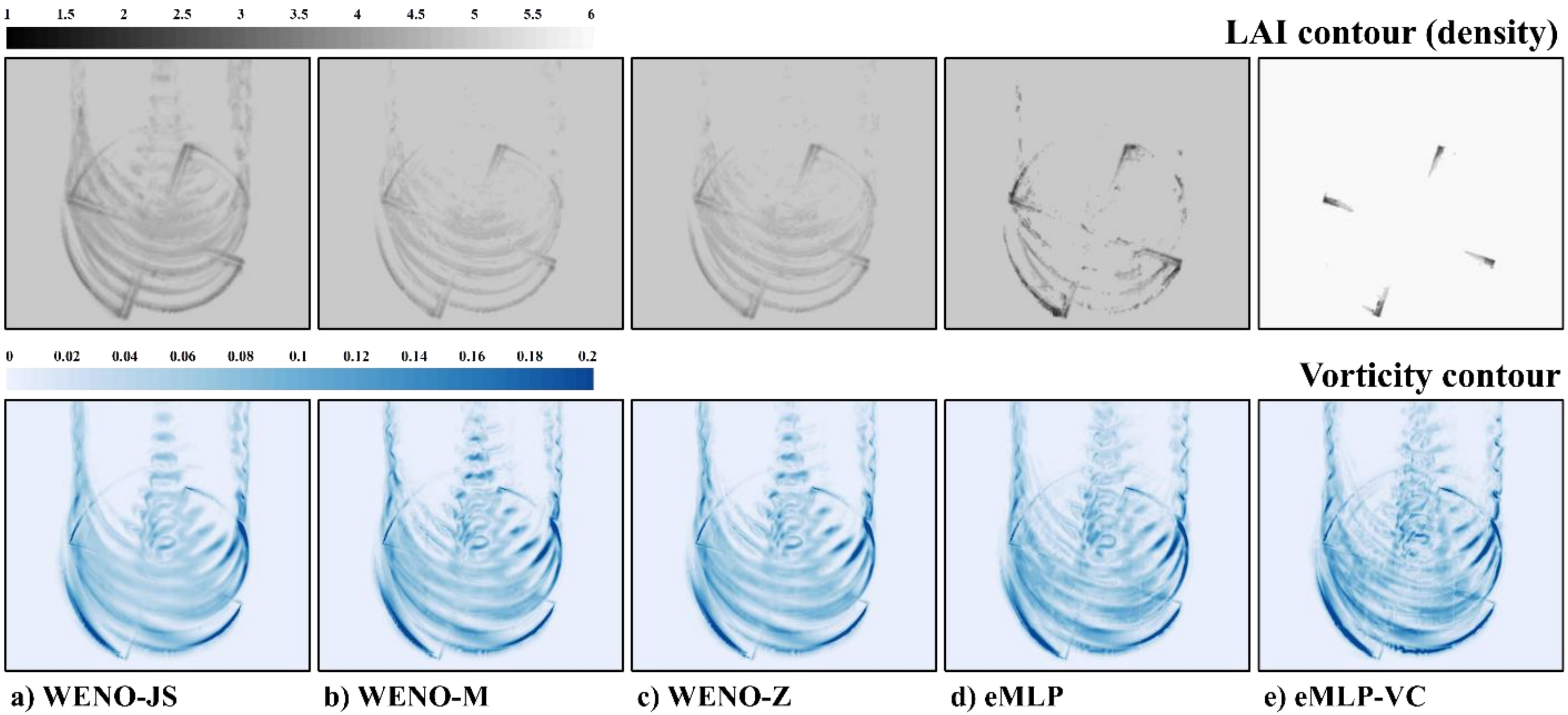

Fig. 5.8 Local-order-of-accuracy index and vorticity contour at 1.0c above the rotor disk plane {a)WENO-JS, b)WENO-M, c)WENO-Z d) eMLP, e) eMLP-VC}.

In the plane shown in Fig. 5.8, all areas are physically continuous because only the interactions of vortices without any discontinuities exist. Therefore, if the grids are sufficient for the accurate description of the vortex profile distribution, ideal accuracy should be applied in all areas. However, the grids used in this study are relatively coarse. Considering the realistic core size of the tip vortex [27,69], the near body grids give one grid point in the vortex core. As shown in the 2D Isentropic vortex advection problem, it is not easy to preserve the vortex in such a coarse grid system. The poor grid quality leads to the artificial dissipation inherent to numerical schemes. Consequently, the local truncation error increases, and the local accuracy and LAI decrease. All schemes have a low LAI at the region where the tip vortex is formed. WENO-JS has a low level of LAI even in the trajectory of the tip vortex. The LAI of eMLP degrades more severely. This degradation of LAI implies that excessive numerical dissipation is continuously applied while the vortex advects. Consequently, a relatively weak vortex faces the following blade.

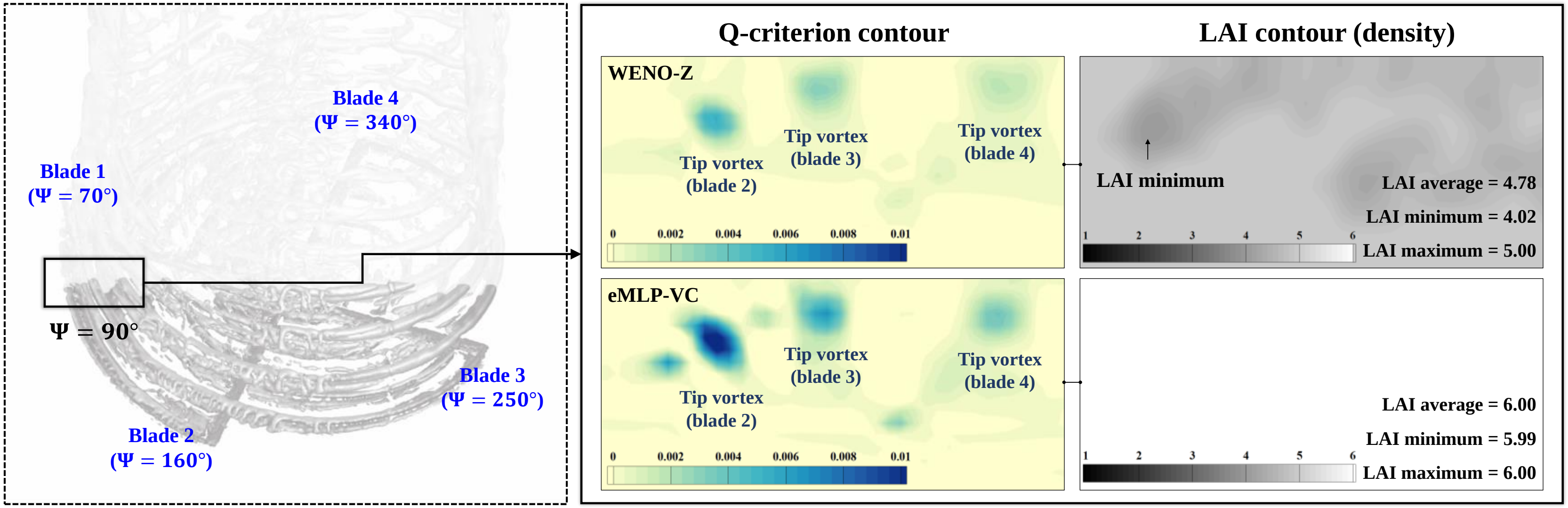

Fig. 5.9 Local-order-of-accuracy index and q-criterion contour at $\psi = 90°$ plane.

The tip vortex generated by the leading blade is advected, and degradation of LAI appears even before the vortex hits the next blade. Figure 5.9 shows the Ψ=90° plane when blade 1 is positioned at Ψ=70°. The vortices generated from the leading blade are shown in the Q-criterion contour. The degradation of local-order-of-accuracy is represented through the LAI contour. WENO-Z yielded the reduced LAI near the vortices. In particular, more degradation occurs near the tip vortex of blade 2, which has strong strength due to the short vortex age. Since the vortex flow change is large in the insufficient grid system, WENO-Z adjusts the stencil weight and applies excessive numerical dissipation. As can be seen in Fig. 5.8, numerical dissipation is continuously applied to the vortex trajectory, and as a result, the strength of the vortex is weakened, and the actual physical phenomenon cannot be properly simulated.

The LAIs of the five schemes can be quantitatively compared. In Fig. 5.10, the mean, minimum, and maximum LAI values are compared. The average value in the 1.0 chord above rotor plane is smaller than the maximum value that each scheme can produce. The local truncation error increases in the wake region, which lowers the overall accuracy. The minimum LAIs of the eMLP-type schemes are 1.00 and 1.22. In eMLP-type schemes, the tip vortex region of strong vorticity is considered as the discontinuous region, such that TVD and MLP limiting are applied. Consequently, first-order accurate reconstruction is performed, resulting in low local accuracy. The minimum LAIs of WENO-type schemes are 3.15, 3.26, and 3.16. The WENO-type schemes have higher LAIs than the eMLP-type scheme in the discontinuous region because WENO-type schemes use at least third-order accurate reconstruction method. The eMLP-type schemes that use the limiting method only where the change in flow is relatively large exhibit local accuracy degradation solely in the tip vortex trajectory and can maintain ideal high-order accuracy in the remaining area. In eMLP-VC, the fifth-order truncation error is eliminated in most areas through low Mach number adjustment; thus, the average LAI value of the entire domain is 6.00.

Through LAI analysis, we were able to specify the region where numerical dissipation is applied. In the tip vortex generation region, all three schemes strongly add numerical dissipation. In the case of eMLP and WENO-type schemes, numerical dissipation is continuously added during the vortex advection process. The applied numerical dissipation continuously weakens the strength of the vortex and the strength of interaction with the following blade. Consequently, numerical dissipation limits the prediction of load fluctuation and aeroacoustic noise.

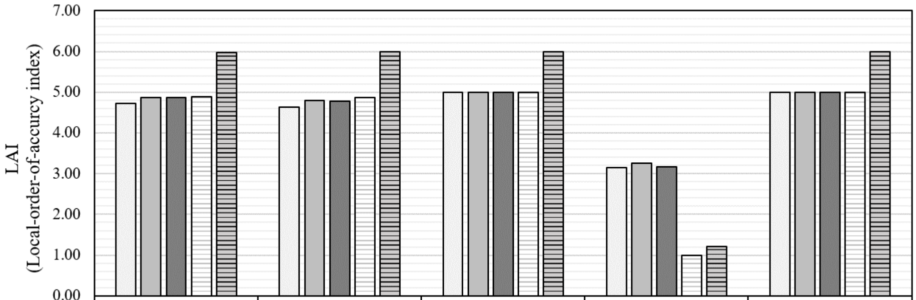

	Average (1.0c above, Fig. 15)	Average (psi=90, Fig. 16)	Average (whole domain)	Minimum (whole domain)	Maximum (whole domain)
WENO-JS	4.72	4.63	5.00	3.15	5.00
WENO-M	4.87	4.79	5.00	3.25	5.00
WENO-Z	4.86	4.78	5.00	3.16	5.00
eMLP	4.89	4.87	5.00	1.00	5.00
eMLP-VC	5.97	6.00	6.00	1.22	6.00

Fig. 5.10 Comparison of the local-order-of-accuracy indexes (HART-II).

The overall HART-II rotor flowfield is shown in Fig. 5.11. Figure 5.11 shows the vortices of HART-II based on the iso-surface method according to the Q-criterion. Several physical phenomena during the forward flight are revealed, such as blade–vortex interaction, vortex–vortex interaction, and vortex merging. Differences in interaction depend on the scheme. The differences are clearly revealed in the enlargements shown in Fig. 5.11. The calculation results clearly show that the blade and vortices interact at $\psi = 70°$ and $\psi = 340°$. The vortex colliding with the inner section of the blade at $\psi = 70°$ is a vortex generated by the blade before one revolution. The vortex strength is weak because the age is old, and the vortex is generated at a small angle of attack. Nevertheless, WENO-M, WENO-Z, and eMLP-type schemes adequately capture the weak BVI, while WENO-JS cannot.

The reason why eMLP-VC adequately simulates the interaction of vortices is that high-order accuracy is maintained in the entire domain, except for some regions where tip vortices are generated. Not only the tip vortex but also the secondary vortex of weak vorticity is evident in the eMLP-VC results. However, WENO-JS has a relatively low LAI in most of the tip vortex trajectories. Because numerical dissipation is continuously added, WENO-JS cannot simulate the interaction with the blade by dissipating the vortices with weak vorticity. Therefore, it can be inferred that load fluctuation and aeroacoustic noise will be predicted less accurately due to the dissipated vortex.

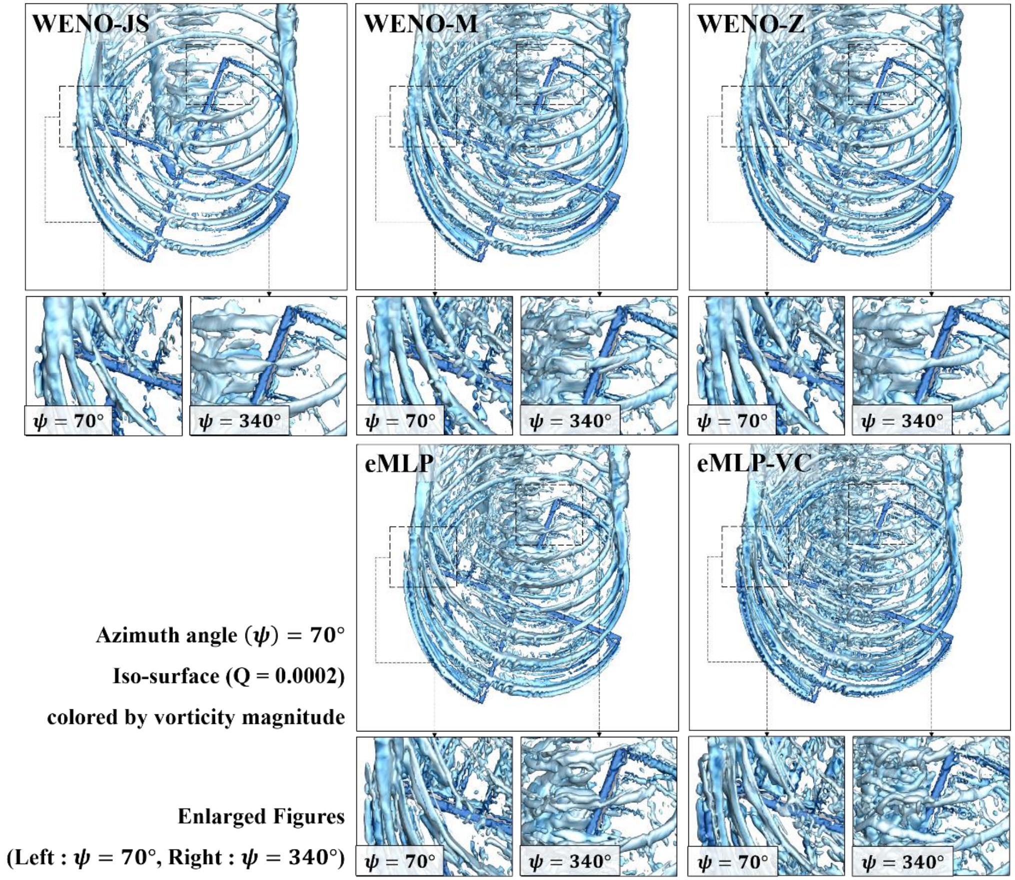

Fig. 5.11 Comparison of the HART-II flowfields using the iso-surface method (Q-criterion).

Figure 5.12 shows the aerodynamic load prediction in the 87% radial section according to the blade azimuth angle. Figure 5.12a shows the normal force distribution, $\mathrm{C_N M^2}$, and Fig. 5.12b shows the mean removed normal force distribution. The experimental values and CFD results were compared across the three schemes. The load fluctuations in the first ($0° \leq \psi \leq 90°$) and fourth ($270° \leq \psi \leq 360°$) quadrants of the experimental values show that the blade and vortex interact. The tip vortices of the preceding blade and the following blade interact to generate fluctuations in the airload. Comparing the enlarged parts of the first and fourth quadrants of Fig. 5.12, it can be observed that the BVI in the first quadrant is relatively weaker than the BVI in the fourth quadrant. This is because the vortex of the first quadrant is relatively old and is generated at a small angle of attack [70]. All three schemes capture BVI in the fourth-quadrant but demonstrate limitations in first-quadrant BVI capture. In WENO-JS, most first-quadrant BVI cannot be simulated, and fourth-quadrant BVI is captured with weak intensity. Improved versions of WENO-JS, which are WENO-M and WENO-Z, show much enhanced predictability of BVI. Also, eMLP and eMLP-VC capture most of the BVI.

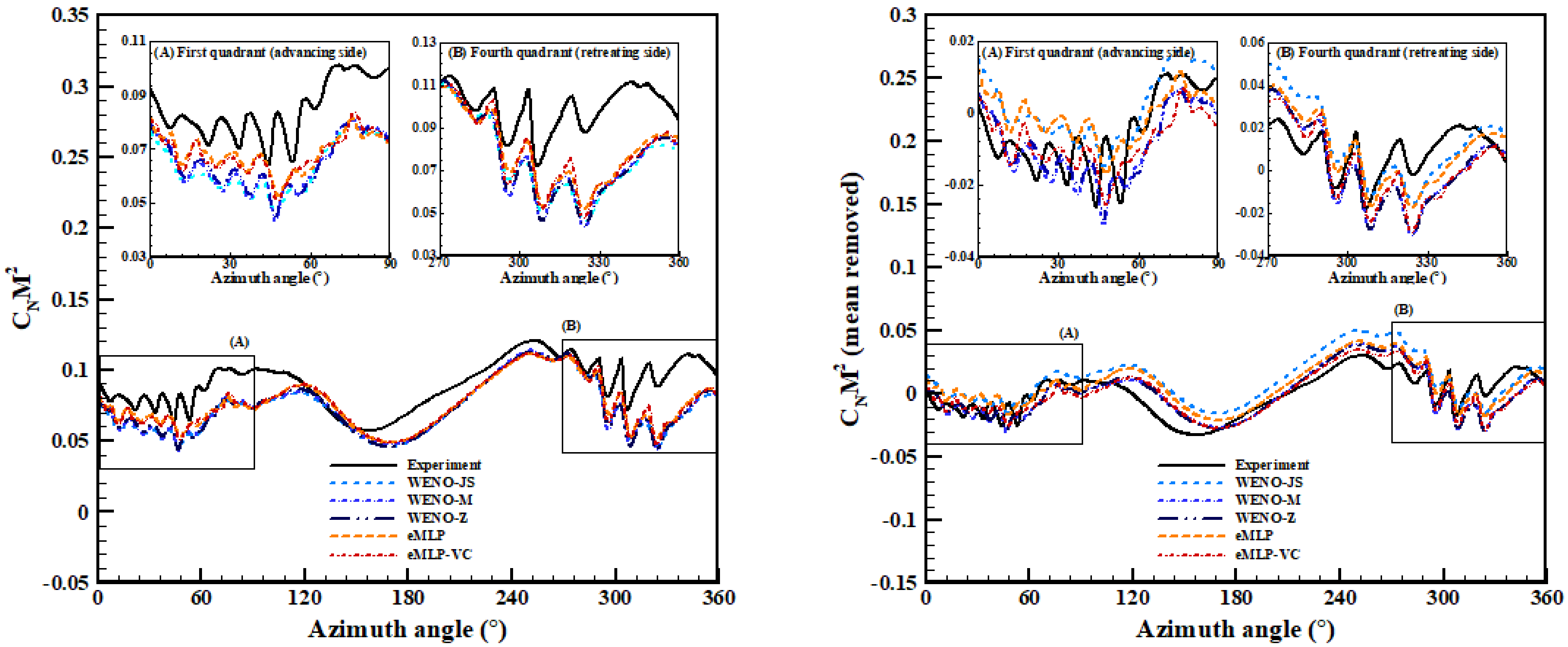

a) Normal force distribution ($C_N M^2$)

b) Mean removed normal force distribution

Fig. 5.12 Comparison of load predictions in the 87% radial section.

5.2.4 Aeroacoustic Results

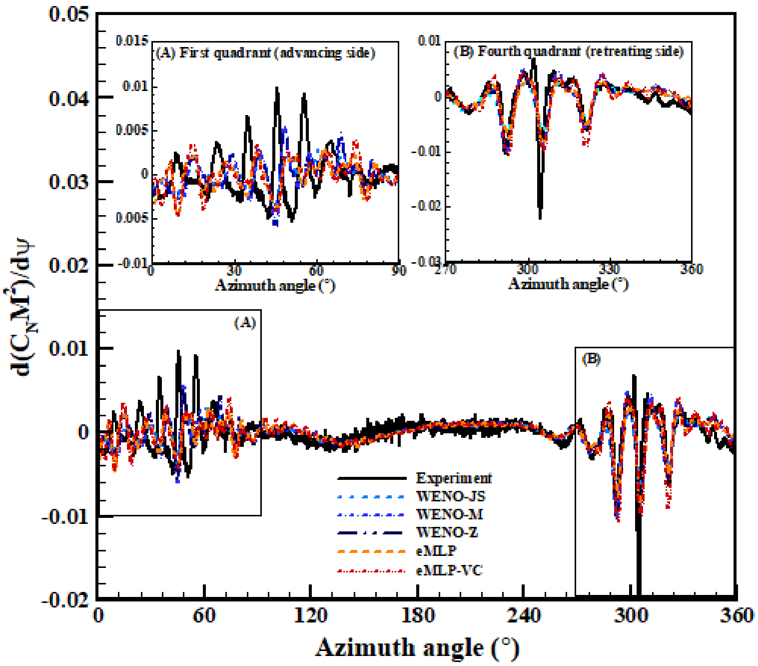

Fig. 5.13 Derivative of the normal force in the 87% radial section.

The azimuthal derivative of the normal force coefficient $\left(\frac{d(C_N M^2)}{d\Psi}\right)$ in the 87% blade radial section is shown in Fig. 5.13. Experimental values vary significantly in the first and fourth quadrants where BVI occurs. The fluctuation value in the derivative of all schemes is smaller than the experimental value, implying that all schemes simulate first-quadrant BVI with a small amplitude. Phase lag is also shown in all schemes. On the other hand, in the case of the fourth-quadrant, although there is a difference in intensity, most schemes capture load fluctuations properly. WENO-M and WENO-Z capture the strength better than WENO-JS, and eMLP-VC also shows better predictability than eMLP. These results are consistent with the LAI analysis of the flowfield performed the previous section.

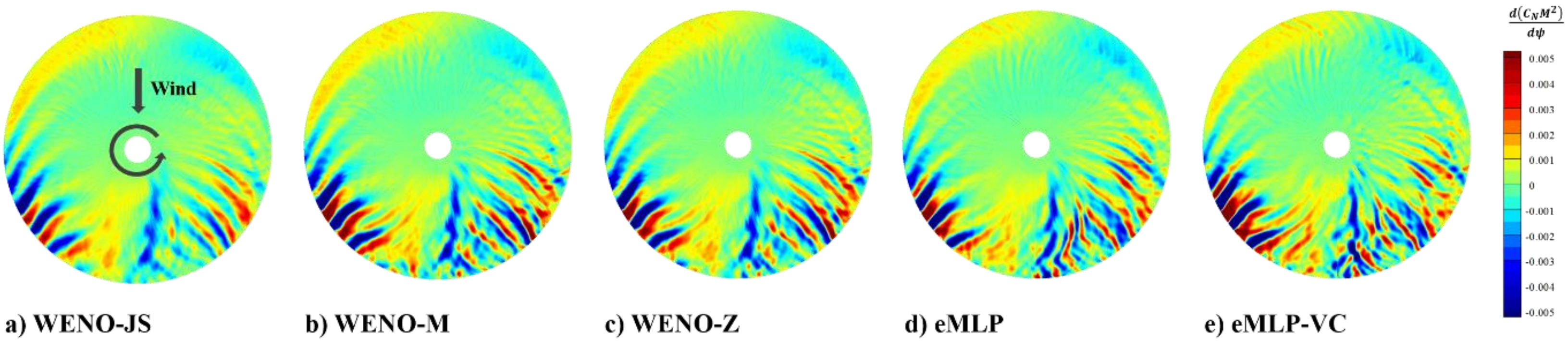

Fig. 5.14 Comparison of the azimuthal derivatives of the normal force (counter-clockwise).

The azimuthal derivative of the normal force for the entire rotor surface is represented in Fig. 5.14. In addition to the 87% radial section shown above, the vortex wake and four blades interact, and the normal force fluctuates throughout the rotor surface. Furthermore, Figs. 5.12 and 5.13 show that BVI mainly occurs on the advancing and retreating sides. The high BVI intensity on the retreating side is clearly visible. Differences in each numerical scheme can be clearly identified. Except for WENO-JS, all four schemes show similar fluctuations. Not only interactions with strong vortices but also interactions with relatively weak vortices.

The noise of the HART-II blade was measured 2.215 m below the rotor with a total of 17×13 microphones. The mid-frequency, the band where the aerodynamic noise caused by BVI is dominant, is in the range of 6 to 40 blade passing frequency. Figure 5.15 shows the mid-frequency sound pressure level (SPL) contours. The experimental values and noise results based on the five spatial discretization schemes were compared.

According to the experiments, the SPL on the advancing and retreating sides is 20 dB or higher than that of the surrounding regions due to BVI. All five schemes capture the directionality of noise well. Both the retreating side and the advancing side, where BVI noise is intense, have high predicted noise values. As indicated by LAI analysis and aerodynamic load prediction, improved versions of each type of scheme show much enhanced predictability of noise. Among the five schemes, eMLP-VC produced results most similar to the experimental results.

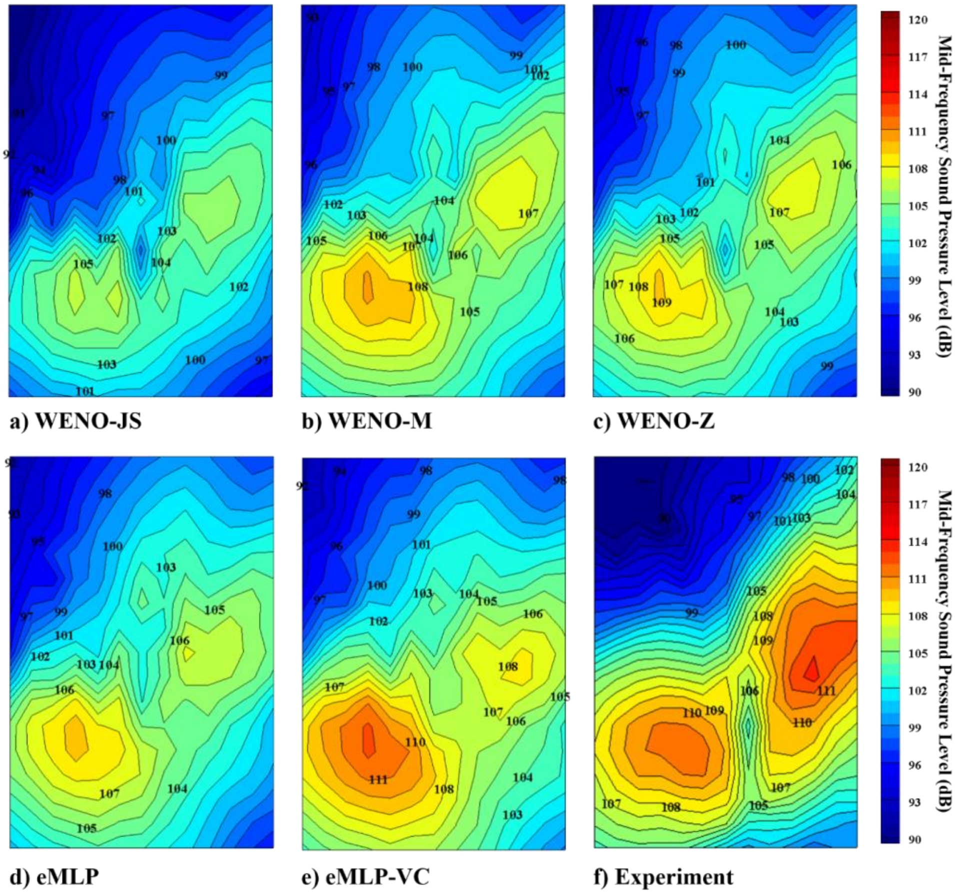

Fig. 5.15 Comparison of the noise maps at 2.215 m below the rotor plane (mid-frequency sound pressure level contours).

On the retreating side, the eMLP-VC results were very similar to the experimental results regarding aeroacoustic directivity and SPL. However, a difference in the advancing side exists. The strength of the vortex interacting with the blade is relatively weak; thus, the load fluctuation caused by BVI is described inadequately. Consequently, the calculated noise is different from the experimental noise. WENO-M and WENO-Z showed a difference of about 2-3dB from the experimental value on the retreating side. In eMLP and WENO-JS, which do not predict airloads relatively satisfactorily, the differences in SPL are more significant. eMLP and WENO-JS demonstrate a difference of approximately 5-7 dB. The limitations shown in the 1D and 2D benchmark tests are clearly shown in the noise prediction of the 3D application.

To get an accurate solution in aeroacoustic prediction using eMLP and WENO-JS, a denser grid system that can preserve the vortex by supplementing the numerical dissipation of the scheme is required. Also, in order to capture the BVI noise on the advancing side accurately where the weak vortex is dominant, all schemes need fine grids enough to preserve the vortex well. In the grid system, where previous researchers have successfully conducted noise analysis, the spacing between the fine background grids is 0.1chord or less. Considering that the current grid system has a spacing of 0.15chord, the computational cost will increase by approximately 1.5^3 times.

As predicted in the LAI analysis, the schemes which continuously add the numerical dissipation during vortex advection have limitations in predicting load fluctuations and noise with a coarse grid system. eMLP-VC can adequately preserve a vortex by minimizing numerical dissipation, except in the blade tip region, delivering excellent performance in predicting aerodynamic noise. According to the assessment based on the flow distinguishing step in eMLP-VC, most parts of the vortex trajectory are smooth; thus, numerical dissipation can be minimized. In addition, because of low Mach number adjustment, eMLP-VC can conduct a central-type reconstruction in most subsonic regions, which reduces the dissipation error.

5.3 Design exploration of co-rotating coaxial rotor

Newly proposed UAM eVTOL aircraft of various configurations use multiple propulsors in common. Due to the requirement for compactness and high thrust at the same time, research on coaxial rotor systems has been actively conducted recently. Unlike conventional helicopters, interests in co-rotating coaxial rotors (also called as stacked rotors), which are coaxial rotors rotating in the same direction, has also been increased because torque balance does not have to be considered within one rotor system. Stacked rotors have two potential advantages over counter-rotating coaxial rotors; First, the pitch angles of the upper and lower rotors can be optimized only for aerodynamic efficiency without considering torque balance. Second, the BVI condition can be avoided by adjusting the angular spacing of the upper and lower rotors.

According to previous studies [71–76], the index angle, which is the angle between the upper and lower rotors, can have a substantial impact on aerodynamic efficiency. Especially when the index angle is small (about -10° to 10°), the aerodynamic efficiency is optimized. The exact cause of index angle effect has not been clearly identified so far. Also, previous researches had been conducted on a small design space, such as a small spacing between rotors or no consideration of pitch angle. Therefore, in this part, a high-accuracy numerical experiment was carried out using the spatial discretization scheme developed earlier in order to discover the applicability of the stacked rotor and the underlying physics.

T-motor CFprop 20inch was used as the baseline propeller. With three design variables, a total of 450 cases were calculated. In addition, the underlying physics, which can only be achieved by using a higher-order accuracy scheme, was identified, and a more detailed analysis was performed on the optimal case. Details will be discussed in the following sections.

5.3.1 Design Problem

Three design parameters are considered as stacked rotor designs. The first parameter is the difference in pitch angle between upper and lower rotors, $\delta\theta$. If $\delta\theta$ is $x°$, it means that the pitch angle of an upper rotor decreases by $(x/2)°$ and the pitch angle of a lower rotor increases by $(x/2)°$. The range of pitch angle difference is set to 0° to 4° The second parameter is a vertical spacing between upper and lower rotors, δz. δz is normalized by the blade diameter, D. The range of the vertical spacing is set as 0.1D to 0.5D. The last parameter is an index angle, $\delta\phi$. The positive index angle means that the lower rotor leads. The range of index angles is set as -90° to 90°. To observe the abrupt fluctuation in aerodynamic performance near $\delta\phi = 0°$ shown in previous studies [71,72], the interval of $5°$ was set near 0°. The schematic of each variable is shown in Fig. 5.16. The range of each variable is shown in Table 5.1.

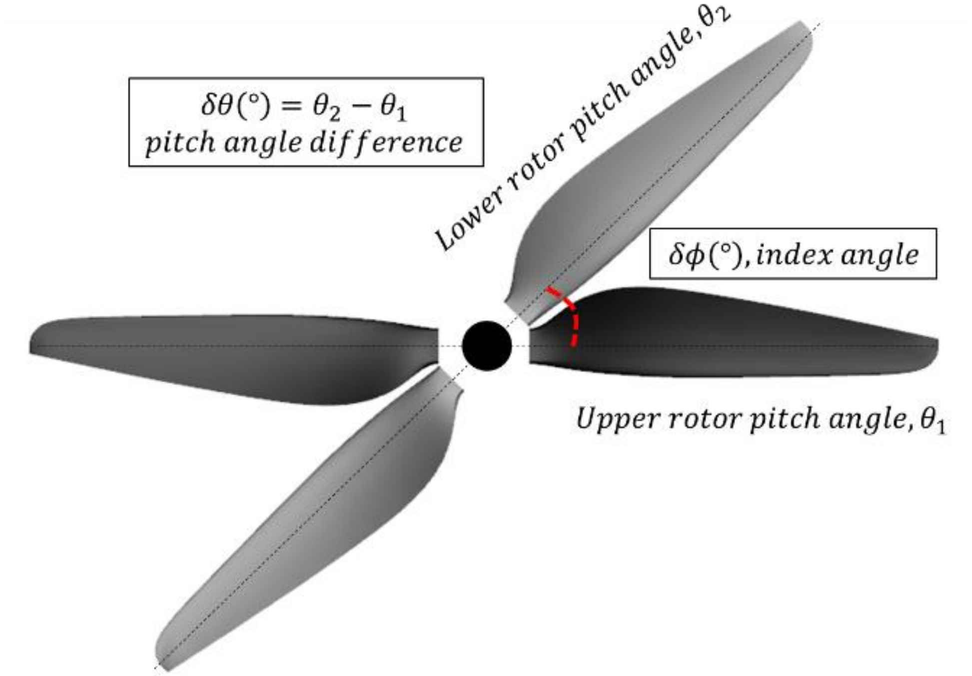

a) Top view

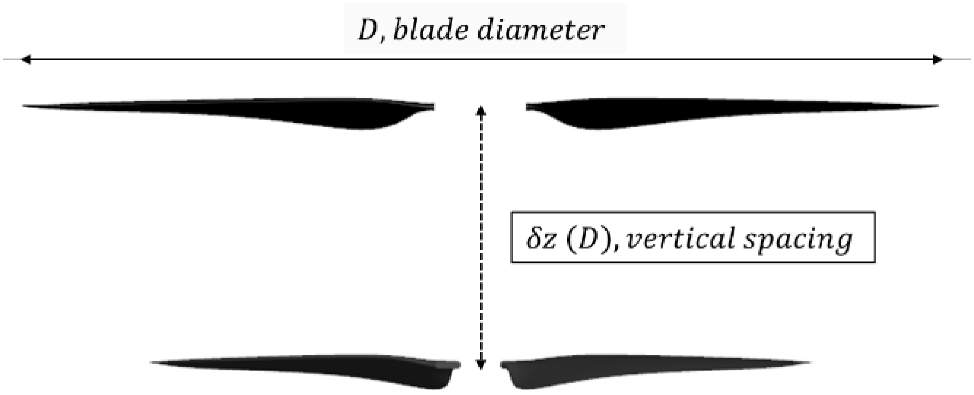

b) Side view

Fig. 5.16 Schematic of design variables.

Table 5.1 Definitions and ranges of design variables.

Variables	Definition	Range
$\boldsymbol{\delta\theta}$ (°)	Pitch angle difference	0, 1, 2, 3, 4
$\boldsymbol{\delta z}$ ($\boldsymbol{D}$)	Vertical spacing (D = blade diameter)	0.1, 0.15, 0.2, 0.3, 0.4, 0.5
$\boldsymbol{\delta\phi}$ (°)	Index angle ((+) means lower rotor leading, and (-) means upper rotor leading)	-90, -60, -45, -30, -20, -10, -5, 0, 5, 10, 20, 30, 45, 60, 90

Aerodynamic analyses were performed for 450 design of experiment (DOE) cases. The full-factorial method is used as DOE. The rotation speed is 3000 rpm for both the upper and lower rotors. The Mach number of the blade's tip is 0.45, and the corresponding Reynolds number is 988,000. The objective function of the stacked rotor design problem is the non-dimensional power loading (C_T/C_P), a hovering performance index. The non-dimensional power loading can be defined as follows:

$$\frac{C_T}{C_P} = \frac{\left(C_{T,upper} + C_{T,lower}\right)}{\left(C_{P,upper} + C_{P,lower}\right)}$$

where C_T and C_P represent thrust and power coefficient, respectively.

5.3.2 Overall Results

All cases were calculated assuming steady-state, and converged through 14,000 iterations. The converged flowfields are the same as shown in Fig. 5.17. The vortices are visualized through the iso-surface method based on the Q-criterion. The tip vortices and vortex sheets of each rotor are well-resolved. Fig. 5.17d shows the vortex contour in the plane sliced with respect to the upper rotor. The strength and trajectory of each vortex can be figured out.

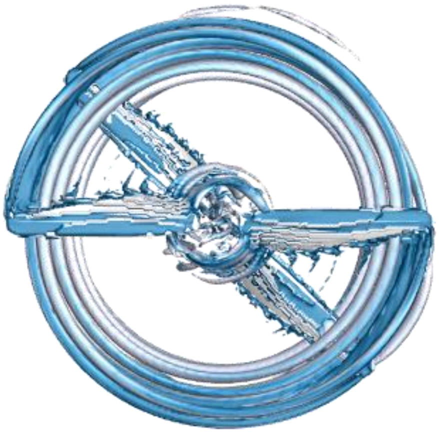

a) Iso-surface, top-view

b) Iso-surface, perspective-view

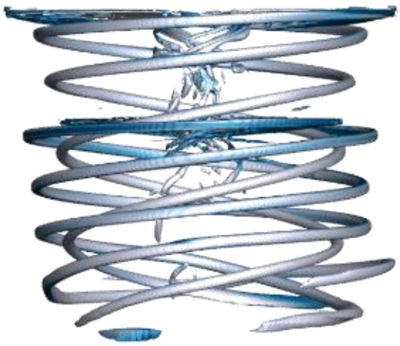

c) Iso-surface, side-view

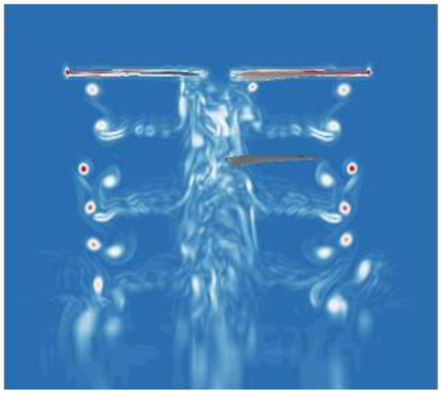

d) Slice, vortex contour

Fig. 5.17 Flowfields of a stacked rotor configuration.

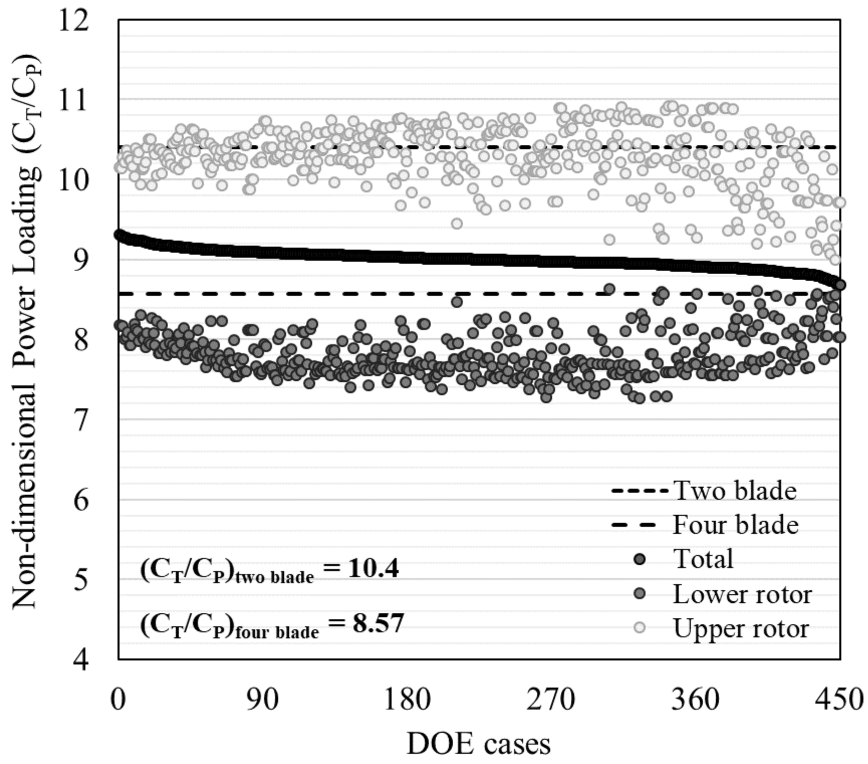

Fig. 5.18 Non-dimensional power loading of DOE cases.

The results of numerical calculations are shown in Fig. 5.18. The non-dimensional power loadings for a total of 450 cases are represented. Maximum and minimum non-dimensional power loadings are 9.31 and 8.68, respectively. The non-dimensional power loading of the four-blade single-rotor with the same solidity is 8.57, which confirms that the performance of the four-blade single-rotor is lower than that of the stacked rotor with the lowest performance. Figure 5.18 also shows the performances of the isolated upper and lower blade. The isolated two-blade single-rotor has a non-dimensional power loading of 10.4. All lower rotors have lower performance than an isolated two-blade, which is mainly due to the wake effect of the upper rotor.

5.3.3 Underlying Physics

Flowfield and performance analysis according to design variables were conducted for 450 cases. For detailed analysis, the effective angle of attack (α_{eff}) for each section of the blade was calculated. It was calculated in the same way as Jung et al. [77]. 2D CFD simulation was also performed to get the zero-lift angle. Sectional thrust and power distributions and vortex dynamics were analysed. As a result, two dominant underlying physics in the stacked rotor system were discovered: 1) inflow effect and 2) wake interference effect.

- ***Inflow effect***

The inflow effect refers to the effect of the upper rotor on the inflow of the lower rotor and the effect of the lower rotor on the inflow of the upper rotor. In the case of the lower rotor, the upper rotor's wake induces the downward flow to the lower rotor directly. The inflow of the lower rotor greatly increases due to the downwash of the upper rotor. As a result, the effective angle of attack of the lower blade is reduced, which can be found in Fig. 5.19. The effect of downwash is very strong at r/R $\leq$ 0.9. On the other way, the lower rotor affects the inflow of the upper rotor. The lower rotor accelerates the wake of the upper rotor, making the wake downward speed faster. Consequently, the lower rotor makes the upper rotor inflow faster. This effect lowers the effective angle of attack of the upper rotor. Compared with the isolated single blade, the effective angle of attack distributions for both the upper and lower rotors are low in all sections.

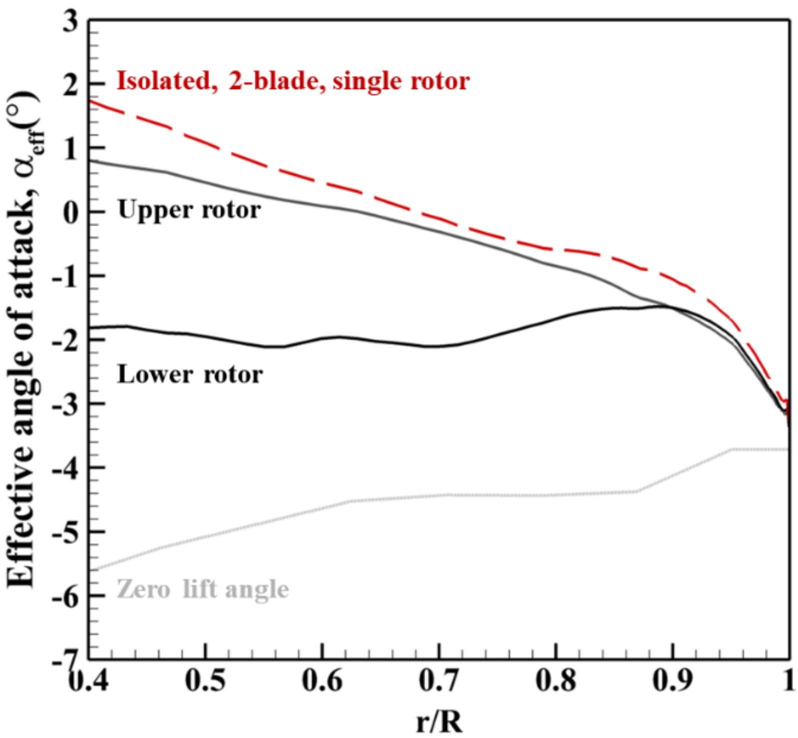

Fig. 5.19 Effective angle of attack distribution along the blade ($\delta z = 0.1, \delta\theta = 0°, \delta\phi = 90°$).

Figure 5.20 compares the flowfields of an isolated single rotor with two blades and a stacked rotor. The design variables of the stacked rotor in Fig. 5.20 are as follows: $\delta z = 0.1, \delta\theta = 0°, \delta\phi = 90°$. Vortex dynamics show the inflow effect directly. In the case of the stacked rotor, the miss distance is about twice that of the single rotor. The miss distances of other stacked rotor cases are also larger than that of the single rotor.

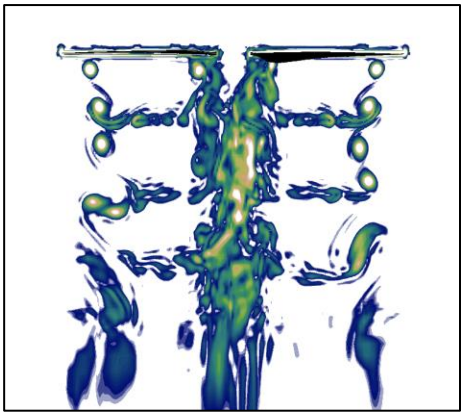

a) Isolated, two-blade, single rotor

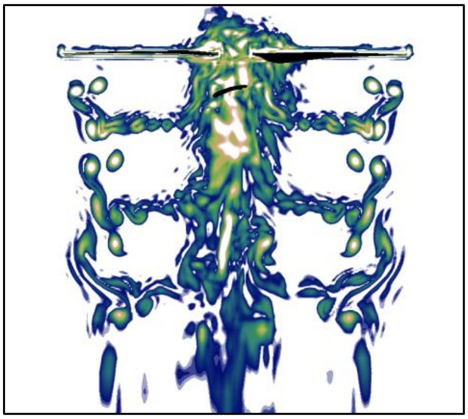

b) stacked rotor
($\boldsymbol{\delta z = 0.1D, \delta\theta = 0°, \delta\phi = 90°}$)

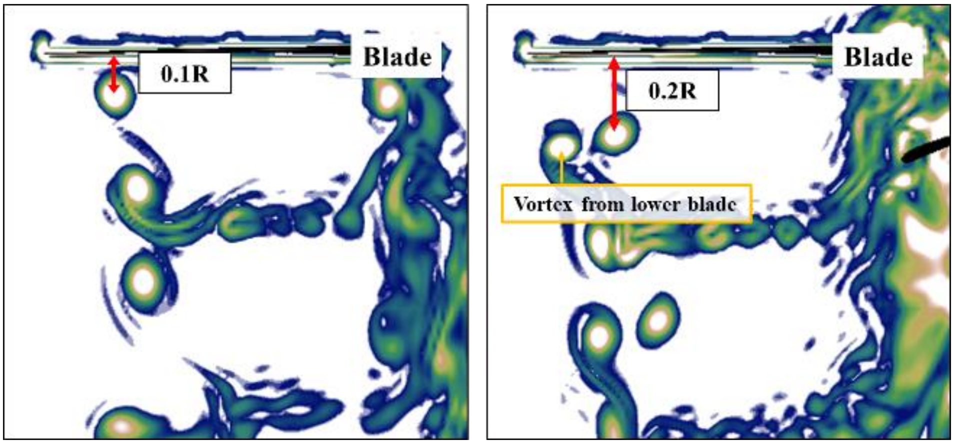

c) Comparison of the miss distance

Fig. 5.20 Flowfields comparison of single-rotor and stacked-rotor.

The non-dimensional power loading according to vertical spacing is shown in Fig. 5.21. The best performance is obtained when the vertical spacing is 0.3D.

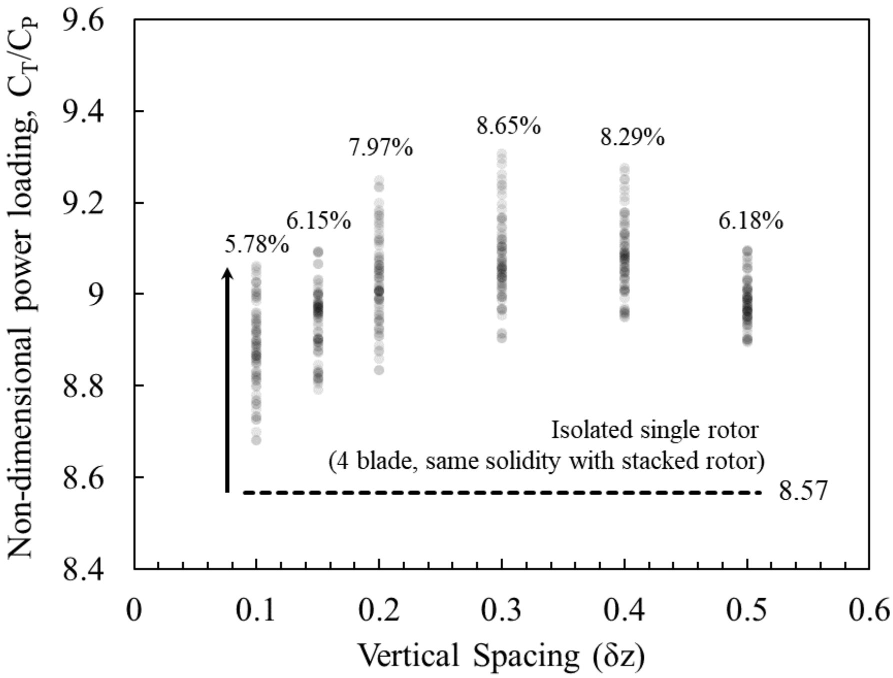

Fig. 5.21 Non-dimensional power loading along the vertical spacing (δz).

- ***Wake interference effect***

The wake interference effect stands for the effect on the aerodynamic performance change of the lower rotor due to the wake of the upper rotor. In Fig. 5.22, the peak of non-dimensional power loading appears differently depending on the phase angle. This difference is mainly due to the change in the performance of the lower rotor. When δz is $0.1D$, the peak appears when the upper rotor is leading. When δz is $0.3D$, the peak appears when the lower rotor is leading.

Figure 5.23 visualizes the flowfields of the best performance cases shown in Fig. 5.22. BVI occur in the flowfields. The tip vortex of the upper rotor interacts with the lower rotor blade. This interaction makes a huge change in aerodynamic performances, especially the power loading. The change in aerodynamic performance according to the phase angle shown in Fig. 5.22 is highly related to the BVI. At the phase angle where BVI occurs, the aerodynamic performance increases. At the phase angle avoiding the BVI, the aerodynamic performance decreases. The position of the peak is changed according to δz and $\delta\theta$, which affect the tip vortex dynamics.

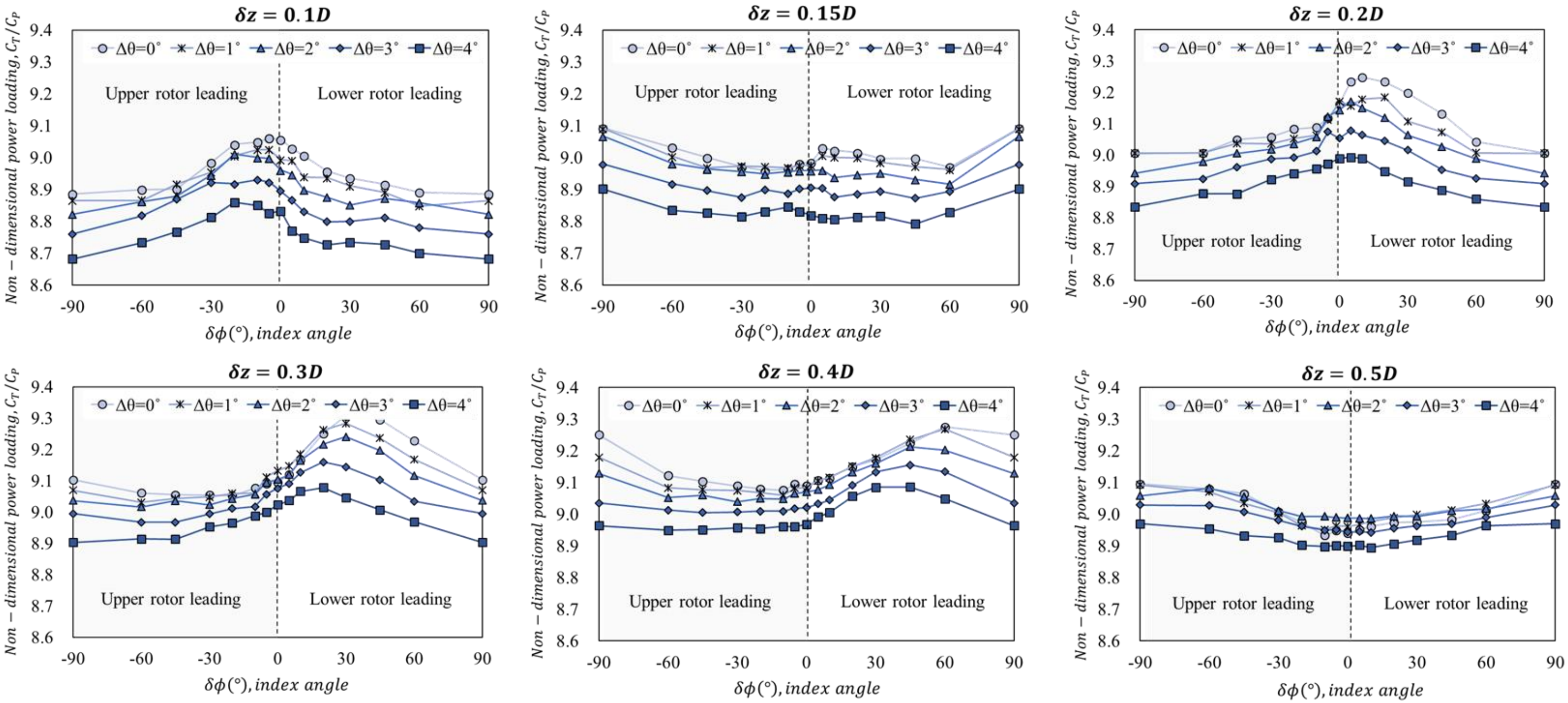

Fig. 5.22 Non-dimensional power loading along the phase angle ($\delta\phi$).

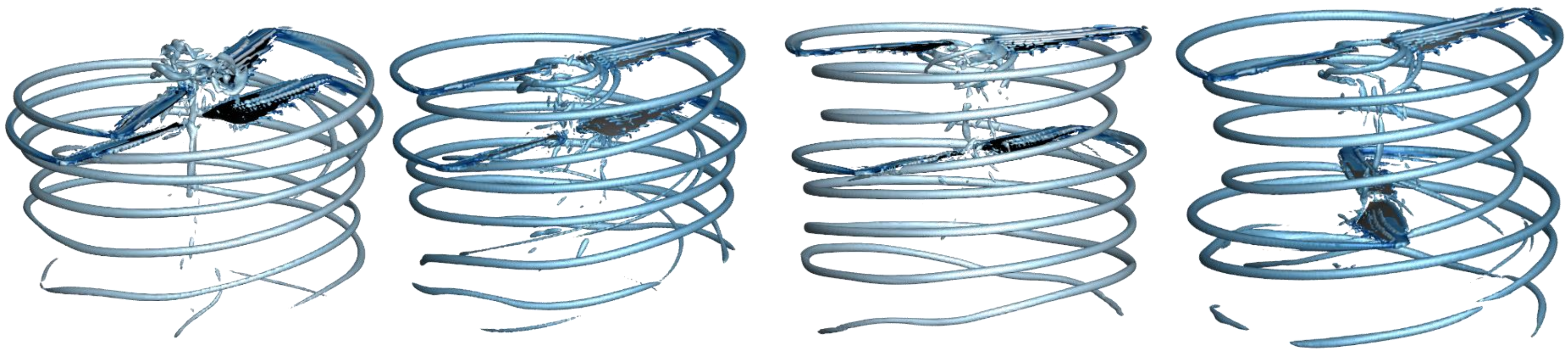

$\delta z = 0.1D, \delta\phi = -20°$, $\delta\theta = -10°$ $\delta z = 0.2D, \delta\phi = 10°$, $\delta\theta = 10°$ $\delta z = 0.3D, \delta\phi = 30°$, $\delta\theta = 30°$ $\delta z = 0.4D, \delta\phi = 60°$, $\delta\theta = 60°$

Fig. 5.23 Flowfields of BVI cases (Iso-surface using Q-criterion, colored by vorticity magnitude).

Figure 5.24 shows the effective angle of attack distributions of stacked rotors. The cases of ($\delta\theta = 2°, \delta z = 0.3D, \delta\phi = -90{\sim}90°$) are shown. The case in red stands for the upper rotor leading cases. The blue lines stand for the cases of the lower rotor leading. The effective angle of attacks of upper rotors have little fluctuation according to $\delta\phi$. However, in the cases when the lower blade is leading, the effective angle of attack of the lower rotor changes significantly at r/R=0.7. This is the fluctuation caused by blade-vortex interaction, as seen in Fig. 5.23. The vortex of the upper rotor interacts with the lower rotor blade, which increases the effective angle of attack of the outboard and reduces the effective angle of attack of the inboard. Increased effective angle of attack produces high aerodynamic performance. Since the angle of attack with the highest lift-to-drag ratio in 2D airfoil is 4 to 5°, increasing the effective angle of attack induces high aerodynamic performance. Also, an increase in the effective angle of attack on the outboard side, which has faster freestream velocity, has a noticeable effect on overall aerodynamic efficiency.

Figure 5.25 shows the non-dimensional coefficients for the same case as in Fig. 5.24. When the lower blade is leading, the sectional C_T/C_P changes significantly. The overall aerodynamic efficiency is maximized as the C_T/C_P increases on the outboard side.

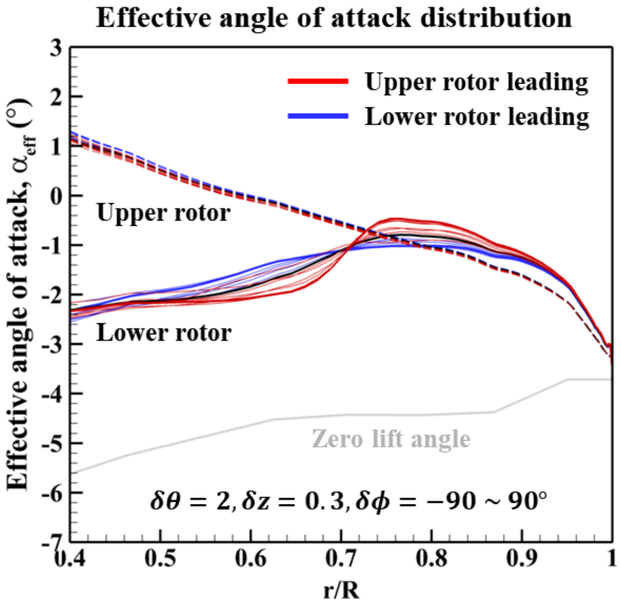

Fig. 5.24 Effective angle of attack distribution of stacked rotors ($\delta\theta = 2°, \delta z = 0.3D, \delta\phi = -90{\sim}90°$).

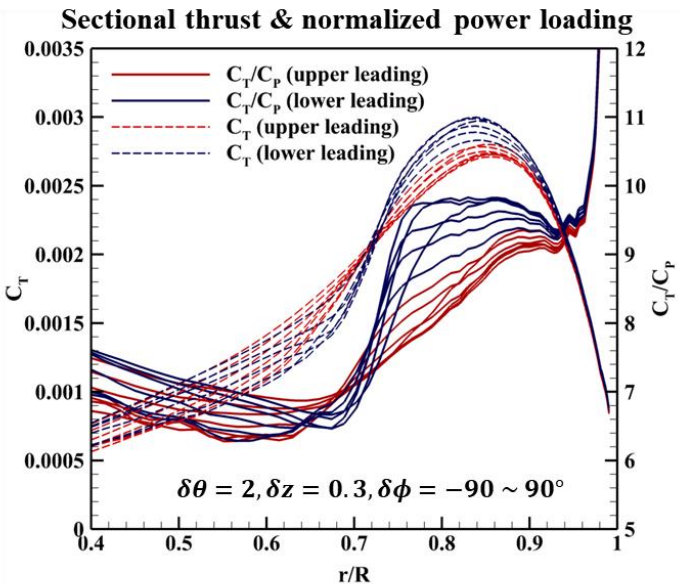

Fig. 5.25 Non-dimensional coefficients distribution of stacked rotors ($\delta\theta = 2°, \delta z = 0.3D, \delta\phi = -90{\sim}90°$).

5.3.4 Detail analysis of best DOE configuration

The configuration with the best aerodynamic efficiency has a variable combination of $(\delta\theta, \delta Z, \delta\phi) = (0°, 0.3D, 20°)$. Detail analysis was conducted for best DOE configuration. In the parameter study, a steady assumption and the relatively coarse grids were constructed for computational efficiency. There may be physical phenomena that did not appear in the parameter study results. To investigate detail physics, extremely high-fidelity computations were performed using a dense grids and advanced turbulence models. Computational settings are as presented in Table 5.2.

Table 5.2 Comparison of computational setting information

	Parameter study	**Detail analysis**
Grids Information (Overset grid)		
Background (near body)	24 million ($\Delta x = 10\%c$)	160 million ($\Delta x = 5\%c$)
Rotor blade	2.4 million / 1 blade, y+ = 1	
Solver Information (KFLOW)		
Spatial discretization	Reconstruction: eMLP-VC Flux function: AUSMPW+	
Temporal integration	Steady calculation	Unsteady calculation (2^{nd} order accurate BDF)
Turbulence model	$k-\omega$ SST	SA-DDES

Through the unsteady analysis, it is possible to analyze the instability caused by the vortex dynamics. For the fast elimination of the non-physical starting vortex that occurs at the beginning of the calculation, a large time step (2.5°) was applied for 10 revolutions from the start. Then additional 10 revolutions of calculations were performed by applying a sufficiently small time-step of 0.25°. It was confirmed that the deviation of the aerodynamic coefficient was less than 1%, and it was concluded that the flow converges.

For the turbulence model, delayed detached eddy simulation model was added to the SA equation. The delayed detached eddy simulation (DDES) model [78] is one of the hybrid RANS/LES models. It is a method of calculating RANS near a wall where very small eddies exist, and calculating with LES in outer regions. It is known that using the SA-DDES model suppresses the non-physical increase of turbulent eddy viscosity, enabling more detailed turbulent wake simulation. In addition to primary tip vortices, secondary vortices generated during wake development and vortex breakdown are easily captured. In addition, a more realistic distribution of turbulent eddy viscosity helps in fast convergence of the rotorcraft flow field.

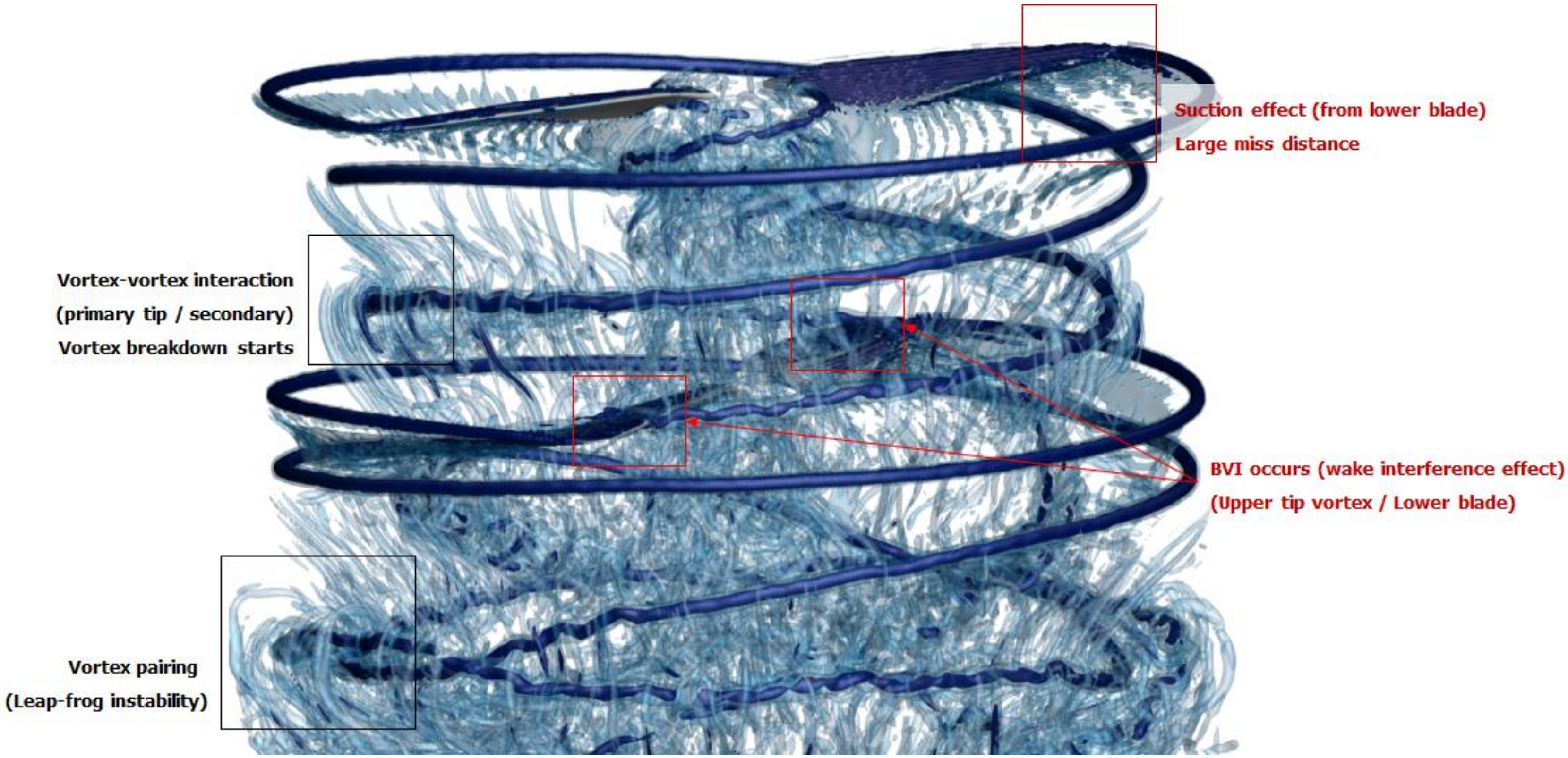

Fig. 5.26 Flowfield of best DOE configuration.

Figure 5.26 is a flow field that visualizes the calculation results. The iso-surface method was used with Q-criterion. As a result, a much higher resolution result was obtained than that shown in the parameter study presented earlier. The underlying physics revealed in previous section appear the same in detailed analysis. The large miss distance of the upper rotor proves that there is a suction effect from the lower blade. Also, the tip vortex generated by the upper rotor interacts on the suction side of the lower rotor. This results in an increase in aerodynamic performance.

There are also physics that can only be seen in high resolution detail analysis. The tip vortex, vortex sheets, and shed vortices generated by the upper and lower rotors were all well resolved. Secondary vortices survive and form a vortex warm, which interacts with the tip vortex, resulting in vortex breakdown. The weakened tip vortex interacts with the lower rotor. Also, the tip vortex generated from the lower rotor descends and causes vortex pairing.

Chapter 6. Conclusions

6.1 Summary and originality of the thesis

For the successful developments of the upcoming next-generation rotorcraft, the fidelity of the numerical solver for analyzing the rotorcraft performance was enhanced while retaining its robustness and efficiency. Several issues about high-order spatial discretization schemes for the numerical solver were addressed with deep consideration of the numerical characteristics of the rotorcraft flowfield and local degradation of order-of-accuracy. In this study, a new high-order accurate spatial discretization scheme, eMLP-VC, was proposed. eMLP-VC was compared and analyzed with conventional high-order accurate schemes mainly used for rotorcraft flow fields. The accuracy and efficiency of eMLP-VC were compared and verified with conventional high-order accurate schemes mainly used in rotorcraft flow fields. Also, this study newly proposes the index called LAI that allows comparison of different types of schemes quantitatively. Since the limiting function or shock sensing mechanism used to maintain robustness in the compressible flow field reduces local accuracy, the LAI can quantitatively compare the reduced local accuracy. As a result of the analysis through LAI, the characteristics that a numerical scheme should have for precise prediction of aerodynamic performance were identified. Finally, by adopting eMLP-VC to the complex and highly unsteady flow field, the superiority of the scheme was demonstrated. The conclusions of the thesis are as follows.

1) An improved high-order accurate spatial discretization scheme, targeting the vortex-dominated and compressible flowfields such as rotorcraft flowfield, was developed in this study. Through the analysis of vortex characteristics, shock sensing algorithm was modified to achieve enhanced vortex preservability. The illness in zero velocity field that conventional eMLP scheme had was also cured through the modification of sensing function. Considering that the rotorcraft flow field is mostly subsonic, a low Mach number adjustment step was added to compensate for the loss of accuracy. A one-order-of-magnitude increase in order-of-accuracy could be achieved by only using the computational cost of TVD limiting. As a result, the accuracy of the suggested spatial scheme, eMLP-VC, was highly advanced with maintaining the robustness and efficiency of original base scheme, eMLP. eMLP-VC showed the robustness not only in the rotorcraft flow field but also in the problem of hypersonic shock discontinuity.
2) Local-order-of-accuracy index (LAI) indicating the local order-of-accuracy of the scheme in the local discretized domain was newly developed to quantitatively analyze the spatial scheme characteristics at the rotorcraft flow field. The LAI quantifies the difference between the truncation error that each scheme should ideally have and the truncation error in the local discretized domain. The LAI can clearly show why even high-order accurate spatial discretization schemes with same theoretical accuracy show different performance in actual engineering problems. The results of the analysis using

the LAI indicates that an advanced shock-sensing mechanism and hybrid central-upwind characteristics are key factors for spatial schemes to achieve high resolution of rotorcraft flow field.

3) Suggested high-order accurate scheme, eMLP-VC, was applied to 3D actual rotorcraft flow field, showing the superiority of the scheme. Precise analysis was performed on PROWIM and HART-II models, which have propeller-wing interaction and blade-vortex interaction respectively. eMLP-VC predicted detailed aerodynamic interference even with a relatively small number of grids, and also showed efficiency than conventional schemes. Phenomena that can only be seen in a precise grid system, such as secondary vortices or vortex breakdown, were also shown in the results. The design exploration was conducted for optimizing the aerodynamic efficiency of co-rotating coaxial rotor, which is considered for high thrust of the UAM eVTOL aircraft. Steady simulations of DOE points with eMLP-VC scheme, two underlying physics, inflow and wake interference effects, were identified. Also, detailed analysis the configuration of best performance was performed using 170 million grid points. The vortex warm and its interactions, which were previously observable only by using billions of grids, could be captured.

The originality and contributions of this study are as follows.

Originality 1. The proposed scheme, eMLP-VC, provides the maximum accuracy that can be achieved using the same number of stencils explicitly in a vortex-dominated and compressible flow field such as a rotorcraft flow field. Two main algorithms make eMLP-VC provide the maximum accuracy: low Mach number adjustment and flow distinguishing mechanism. The degradation of accuracy in subsonic flow, which is a disadvantage of upwind biased interpolation, can be easily solved using the low Mach number adjustment without compromising the robustness. Also, the main algorithms of eMLP-VC are relatively easy to implement numerically and available to be applied easily other-type of upwind schemes. These algorithms can be adopted any other FVM solvers such as NASA's OVERFLOW and ONERA's elsA, which are mainly used for rotorcraft flow field analysis. eMLP-VC is verified its accuracy, robustness, and efficiency not only in relatively simple 1D or 2D numerical benchmark tests but also in 3D engineering problems using complex grid systems.

Originality 2. An index that can quantitatively compare the performance of schemes developed with different concepts is proposed. The LAI presented in Part 4 indicates the difference between the truncation error that each scheme should ideally have and the truncation error in the local discretized domain. Since the discontinuity in compressible flow often makes the solver unstable, a spatial discretization scheme with limiting algorithms is usually used for compressible flow. However, the limiting algorithms usually result in the degradation of local accuracy for incompressible and continuous flows. The LAI can quantify the local order-of-accuracy and clearly show the degradation of local order-of-accuracy. Any explicit spatial discretization scheme can be analyzed. In addition, it is possible to apply the LAI analysis in any flow field that needs high accuracy, not just in the rotorcraft flow field. Especially in vortex-dominated flowfield such as near wall region or stall region, several vortex interactions occur, and engineers are unable to determine whether the vortex interactions are caused by physical phenomena or merely numerical errors. LAI analysis can help to identify the numerical error distributions in local discretized domain. Also, LAI can be easily used as the indicator for grid evaluation or refinement. The implementation of LAI is simple and generic to any explicit spatial scheme.

Originality 3. Detailed analysis of the rotorcraft flow field can be efficiently performed through the developed scheme. Furthermore, even the design optimization can be sufficiently conducted. The PROWIM or HART-II flow applied in this study showed more accurate results than the scheme used in the existing rotor flow field. In the case of design optimization, a low or mid-fidelity solver that can produce calculation results more quickly was used in the past. However, if we use well developed high-order accurate spatial scheme, we can use the high-fidelity solver to conduct the design optimization. This study proved that the design exploration can be conducted efficiently and more deeply when using eMLP-VC scheme. The underlying physics of the co-rotating rotor could be identified. Detail vortex dynamics can be simulated. These findings allow the advanced design of co-rotating coaxial rotor and even in UAM eVTOL aircraft.

6.2 Recommendations for the future work

A major objective of this study is to enhance the fidelity of the numerical solver, particularly through the development of high-order spatial discretization schemes that will improve the accuracy of rotorcraft aerodynamic performance prediction. The newly proposed spatial discretization scheme, eMLP-VC, produces the maximum accuracy that can be achieved with the same number of stencils, and produces much more efficient and accurate results than conventional high-order methods. There are, however, some limitations of eMLP-VC, and further research should be conducted to supplement these findings.

■ Limitations of eMLP-VC and future research works

First, expanding eMLP-VC to unstructured-grid based solver is needed in consideration of application in engineering fields. A research aiming to extend MLP to unstructured grid-based solvers is currently being conducted[53,79], eMLP-VC can be expanded in similar manner. To successfully expand eMLP-VC to unstructured grid solver, sensing algorithm should be efficiently modified for unstructured grid version.

The second issue is to minimize the influence of the user-defined factor of the eMLP-VC. eMLP-VC has a user-defined factor like the existing scheme eMLP and other high-order accurate schemes used for compressible flow. Within eMLP-VC, epsilon(ϵ) in flow distinguishing step plays its role. In the rotor flow field, $\epsilon = 0.01$ is suggested empirically. But when it is used in other flow fields, it is necessary to modify this factor. Since this user-defined factor reduces the expandability of the scheme, the influence of the user-defined factor should be minimized.

Thirdly, the stability of the part where r becomes negative in the TVD limiter needs to be examined. There is a possibility that the error in the negative r region could be amplified when the CFL number increases, so it is necessary to conduct a study that takes this into account.

Lastly, there are still opportunities for minimizing the numerical dissipation error. The simplest way is to use more stencils. Although the fundamental structure of the solver, such as the amount of information exchanged in parallelization, needs to be modified, nevertheless increasing the stencil is the most accurate and fastest way to increase spatial accuracy. Also, it is possible to use the spatial discretization scheme with an implicit method, even though it requires a heavy computational cost. The compact scheme in continuous flow will produce a much higher spatial accuracy.

As well as considering the spatial discretization method, to get higher fidelity of the aerodynamic solver for rotorcraft, several numerical techniques should be advanced. Next-generation rotorcraft will operate under certain operating conditions such as relatively low Reynolds number, which require the advancement of two essential numerical techniques: turbulence modeling technique and temporal integration method.

■ **Turbulence modeling technique**

The turbulence models used in this study assume a fully turbulent flow. However, the flow conditions of actual UAM eVTOL aircraft or conventional helicopters are not fully turbulent. Laminar flow enters to the lifting surface and transitions to turbulent flow occur. These transition process makes considerable change in aerodynamic performance. To deal with these phenomena properly, it is necessary to develop enhanced turbulence modeling methods such as turbulence transition models, detached eddy simulation models, and a wall modeled LES (WMLES) model. Recently, American institute of aeronautics and astronautics (AIAA) is conducting a high lift prediction workshop (HLPW) that predicts the transition point, separation point, and stall angle against a fixed wing model [80]. The results indicate that accurate prediction of the separation point and stall angle was made only through WMLES. RANS and URANS have limitations in predicting the separation point. Also, hover prediction workshop held at AIAA recently emphasized the importance of the transition model by predicting the transition point [43]. In the case of a UAM eVTOL aircraft, since it has a relatively low Reynolds number and Mach number range, it is necessary to further upgrade the turbulence model.

■ **Temporal integration method**

Due to the increasing spatial accuracy of numerical solvers, as well as the increasing sophistication of turbulence models and flow unsteadiness, the accuracy of the temporal integration method becomes increasingly important. The currently used BDF2 is robust but lacks the accuracy. The results of the HART-II prediction workshop demonstrate that the temporal error becomes increasingly dominant as the time step increases [28]. As a result of a large CFL number near the wall where the grid spacing is extremely small, the time step currently applied produces considerable temporal error. There are some efforts to substitute BDF2 to other high accurate methods such as DIRKs or Rosenbrock-type [49,81]. However, those candidates have robustness and efficiency issues. The development of efficient and robust high-order accurate temporal integration methods should therefore be actively pursued.

Appendix

A. Concepts of WENO-type schemes

Since the WENO-type scheme was first developed by Jiang and Shu [7] in 1996, it has been widely used in compressible flowfield analysis that requires high accuracy and robustness, such as in shock-capturing. The WENO-type scheme reconstructs a cell interface quantity using the smoothness of local polynomials. High-order accuracy can be maintained in discontinuous flow because the flowfield is reconstructed using multiple stencils, avoiding the discontinuous region. Representative compressible CFD solvers such as the NASA OVERFLOW [82] and DLR FLOWer [83] also adopt WENO-type schemes and produce valuable results for various flows. However, if the shock wave occurs across several cells, WENO-type schemes tend to cause oscillations and diminish the robustness of the solver. Furthermore, in local extrema, the WENO-type scheme has relatively poor accuracy owing to the incompleteness of local smoothness indicators. Accordingly, there have been many follow-up studies to overcome these shortcomings [13,16,17,84–86].

$(2r-1)^{th}$ order accuracy WENO-type reconstruction is performed as follows:

$$q_{\frac{1}{2}} = \sum_{i=0}^{r-1} w_i^r a_i^r (\bar{q}_{i-r+1}, \cdots, \bar{q}_i) \tag{A-1}$$

The cell quantity at 1/2 interface, $q_{\frac{1}{2}}$, can be reconstructed using the sum and product of the r local polynomial, $b_i^r(\bar{q}_{i-r+1}, \cdots, \bar{q}_i)$ and the polynomial weight, w_i^r. Equation (A-1) shows the left state of the cell interface quantity. The right state of the cell interface can be obtained by moving the stencil by one grid to the right and applying the polynomial weight symmetrically. For conciseness, the cell interface quantity in this paper is defined as the left state of the cell interface, unless otherwise specified. A local polynomial, $b_i^r(\bar{q}_{i-r+1},\cdots,\bar{q}_i)$, can be expressed as follows:

$$a_i^r(\bar{q}_{i-r+1},\cdots,\bar{q}_i) = \sum_{i=0}^{r-1} \alpha_{ij}^r \bar{q}_{-r+i+j+1} \qquad \text{(A-2)}$$

where α_{ij}^r stands for the coefficient of the local polynomial. The polynomial weight, w_i^r, of eq. (A-1) can be obtained using eq. (A-3).

$$w_i^r = \frac{\bar{w}_i^r}{\sum_{i=0}^{r-1} \bar{w}_i^r},\ \bar{w}_i^r = \frac{\gamma_i^r}{(\epsilon+\beta_i^r)^2} \qquad \text{(A-3)}$$

where γ_i^r is an ideal weight for each local polynomial. ϵ is a small positive number that prevents the occurrence of a singularity and weight biasing on one side when the flow is extremely smooth. In this study, $\epsilon = 10^{-6}$. β_i^r is a smoothness indicator of each local polynomial and can be expressed as follows:

$$\beta_i^r = \sum_{m=0}^{r-1}\left(\sum_{j=0}^{r-1} d_{imj}^r\, \bar{q}_{-r+i+j+1}\right)^2 \qquad \text{(A-4)}$$

where s_{imj}^r, α_{ij}^r, and γ_i^r can be obtained using the work of Jiang and Shu [7] and Martin et al. [13]. The original WENO scheme (WENO-JS) can be implemented in the same manner using eqs. (A-1-4). Figure A1 shows a schematic diagram of the fifth-order $(r = 3)$ accurate upwind WENO-type scheme. The process of obtaining polynomial weights in Eqs. (A-3) and (A-4) constitutes the shock-sensing mechanism of WENO-JS. This shock-sensing mechanism can also be called a function of smoothness (FoS) whose role is to assess the smoothness of the flow, adjust the weight, and deal with discontinuities. A well-defined FoS can distinguish smooth regions from discontinuous regions properly so that local accuracy does not decrease. Simultaneously, it can deal with discontinuities in a robust manner.

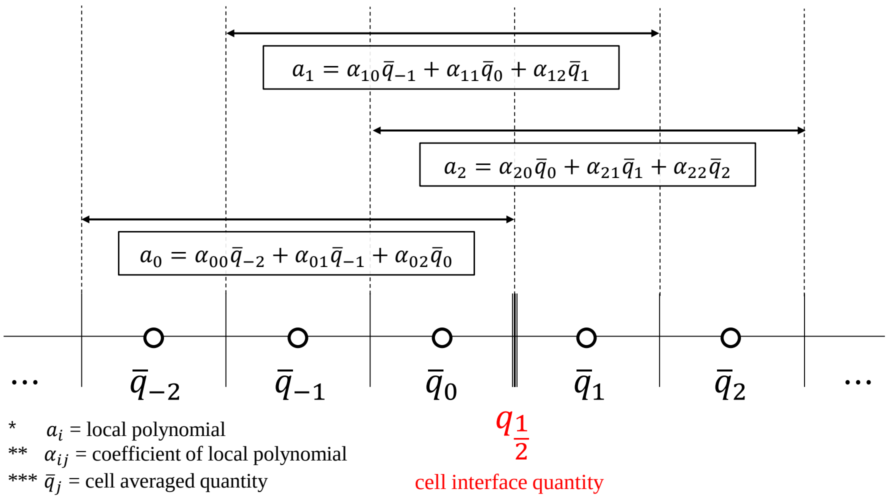

Fig. A1 Schematic of fifth order upwind WENO-type reconstruction.

The method of obtaining polynomial weights in WENO-JS is a favorable approach in addressing discontinuities but has the disadvantage of lowering the local accuracy in local extrema. Because the polynomial weight, w_i^r, depends on the smoothness of the local polynomial, even if all polynomials are smooth, the weight can be biased according to the degree of smoothness. WENO-M and WENO-Z modify the weights of eq. (A-3) differently to solve this problem.

First, WENO-M uses a new mapping method to increase the equivalence of the weight to the ideal weight, γ_j^r. The mapped weights can be expressed as eq. (A-5). Ideal weights are applied in more areas when weights are mapped. Mapped weights reduce the variation in the calculated weight in the smooth local maxima, and consequently, reduce local accuracy degradation.

$$w_{i,WENO-M}^{r} = \frac{w_i^r\left\{\gamma_i^r + (\gamma_i^r)^2 - 3\gamma_i^r w_i^r + (w_i^r)^2\right\}}{(\gamma_i^r)^2 + w_i^r(1-2\gamma_i^r)} \tag{A-5}$$

Second, WENO-Z uses a global smoothness indicator to adjust the weight of eq. (A-3). The global smoothness indicator, τ_{2r-1}, uses a $(2r-1)$-point stencil, expressed as eq. (A-6a). A new weight is expressed as eq. (A-6b). The global smoothness indicator of WENO-Z reduces the influence of the local smoothness indicator. The optimal weight is enforced when the domain is globally smooth. This modification effectively reduces local accuracy degradation in the local extrema.

$$\tau_{2r-1} = \begin{cases} |\beta_0^r - \beta_{r-1}^r|, \; mod(r,2) = 1 \\ |\beta_0^r - \beta_1^r - \beta_{r-2}^r + \beta_{r-1}^r|, \; mod(r,2) = 0 \end{cases} \tag{A-6a}$$

$$w_{i,WENO-Z}^{r} = \frac{\overline{w}_{i,WENO-Z}^{r}}{\sum_{i=0}^{r-1} \overline{w}_{i,WENO-Z}^{r}}, \quad \overline{w}_{i,WENO-Z}^{r} = \gamma_i^r\left(1 + \frac{\tau_{2r-1}}{\beta_i^r + \varepsilon}\right) \tag{A-6b}$$

According to the developers of WENO-M [16] and WENO-Z [17], the advanced algorithms in eqs. (A-5) and (A-6) ensure optimal order convergence near critical points. Modified weights can supplement the loss of order convergence of the original WENO, and performs as an improved FoS for WENO-M and WENO-Z.

B. Global-order-of-accuracy of spatial schemes on benchmark tests

In this Appendix B, global-order-of-accuracy of benchmark tests are presented. For 1D benchmark tests, details of the sine wave and gaussian pulse advection problem are represented in Table B1~2 and Table B3~4, respectively. For the 2D benchmark test, the results of the isentropic vortex advection problem are shown in Table B5.

Table B1 Error and global-order-of-accuracy of low amplitude sine wave advection problem (1D)

Low amplitude sine wave advection problem $\left[q = 6 + 0.1\sin\left(\frac{x}{2.5}\pi\right)\right]$										
Grids	WENO-JS		WENO-M		WENO-Z		eMLP		eMLP-VC	
	L_2 error	order	L_2 error	order	L_2 error	order	L_2 error	order	L_2 error	order
11 × 1	3.93.E-02		3.76.E-02		2.05.E-02		2.03.E-02		1.09.E-02	
13 × 1	2.22.E-02	3.412	1.86.E-02	4.206	1.12.E-02	3.604	1.01.E-02	4.200	4.34.E-03	5.517
15 × 1	1.22.E-02	4.214	9.06.E-03	5.036	6.03.E-03	4.336	5.27.E-03	4.511	1.93.E-03	5.644
17 × 1	6.70.E-03	4.758	4.60.E-03	5.416	3.29.E-03	4.828	2.94.E-03	4.676	9.45.E-04	5.719
19 × 1	3.80.E-03	5.104	2.48.E-03	5.556	1.89.E-03	4.981	1.73.E-03	4.771	4.98.E-04	5.766
21 × 1	2.23.E-03	5.308	1.42.E-03	5.577	1.15.E-03	5.016	1.07.E-03	4.829	2.79.E-04	5.796
25 × 1	8.68.E-04	5.422	5.44.E-04	5.502	4.77.E-04	5.027	4.55.E-04	4.880	1.01.E-04	5.819

29 × 1	3.86.E-04	5.451	2.45.E-04	5.369	2.26.E-04	5.029	2.19.E-04	4.920	4.25.E-05	5.831
33 × 1	1.90.E-04	5.500	1.24.E-04	5.255	1.18.E-04	5.023	1.16.E-04	4.942	2.00.E-05	5.829
37 × 1	1.01.E-04	5.544	6.88.E-05	5.169	6.65.E-05	5.014	6.57.E-05	4.956	1.03.E-05	5.817
41 × 1	5.70.E-05	5.550	4.07.E-05	5.111	3.98.E-05	5.007	3.95.E-05	4.965	5.67.E-06	5.800
51 × 1	1.72.E-05	5.494	1.35.E-05	5.057	1.34.E-05	4.999	1.33.E-05	4.975	1.61.E-06	5.763
61 × 1	6.55.E-06	5.382	5.49.E-06	5.022	5.47.E-06	4.995	5.46.E-06	4.984	5.81.E-07	5.700
71 × 1	2.93.E-06	5.291	2.57.E-06	5.008	2.56.E-06	4.993	2.56.E-06	4.988	2.47.E-07	5.635
81 × 1	1.47.E-06	5.225	1.33.E-06	5.002	1.33.E-06	4.994	1.33.E-06	4.991	1.19.E-07	5.570
121 × 1	1.87.E-07	5.139	1.79.E-07	4.999	1.79.E-07	4.996	1.79.E-07	4.995	1.33.E-08	5.444
161 × 1	4.41.E-08	5.070	4.29.E-08	4.998	4.29.E-08	4.997	4.29.E-08	4.997	2.95.E-09	5.282
241 × 1	5.79.E-09	5.033	5.72.E-09	4.996	5.71.E-09	4.995	5.71.E-09	4.995	3.77.E-10	5.098

Table B2 Error and global-order-of-accuracy of high amplitude sine wave advection problem (1D)

High amplitude sine wave advection problem $\left[q = 6 + 5\sin\left(\frac{x}{2.5}\pi\right)\right]$										
Grids	WENO-JS		WENO-M		WENO-Z		eMLP		eMLP-VC	
	L_2 error	order	L_2 error	order	L_2 error	order	L_2 error	order	L_2 error	order

11 × 1	2.42.E+00		1.88.E+00		1.02.E+00		3.02.E+00		2.54.E+00	
13 × 1	1.49.E+00	2.903	9.31.E-01	4.206	5.60.E-01	3.604	2.23.E+00	1.799	2.02.E+00	1.360
15 × 1	9.13.E-01	3.411	4.53.E-01	5.036	3.01.E-01	4.336	1.63.E+00	2.219	1.40.E+00	2.542
17 × 1	5.72.E-01	3.735	2.30.E-01	5.416	1.65.E-01	4.828	1.10.E+00	3.110	1.25.E+00	0.960
19 × 1	3.69.E-01	3.945	1.24.E-01	5.556	9.46.E-02	4.981	7.50.E-01	3.460	2.52.E-02	35.072
21 × 1	2.45.E-01	4.077	7.10.E-02	5.576	5.73.E-02	5.016	6.31.E-01	1.722	1.41.E-02	5.762
25 × 1	1.19.E-01	4.134	2.72.E-02	5.502	2.38.E-02	5.027	4.36.E-01	2.122	5.17.E-03	5.779
29 × 1	6.49.E-02	4.105	1.23.E-02	5.369	1.13.E-02	5.029	3.12.E-01	2.259	2.19.E-03	5.780
33 × 1	3.77.E-02	4.213	6.22.E-03	5.255	5.91.E-03	5.023	5.79.E-03	30.848	1.04.E-03	5.766
37 × 1	2.26.E-02	4.450	3.44.E-03	5.169	3.33.E-03	5.014	3.28.E-03	4.956	5.39.E-04	5.743
41 × 1	1.40.E-02	4.678	2.04.E-03	5.111	1.99.E-03	5.007	1.97.E-03	4.965	3.00.E-04	5.716
51 × 1	4.82.E-03	4.888	6.75.E-04	5.057	6.68.E-04	4.999	6.66.E-04	4.975	8.71.E-05	5.663
61 × 1	1.97.E-03	4.982	2.75.E-04	5.022	2.73.E-04	4.995	2.73.E-04	4.984	3.21.E-05	5.583
71 × 1	9.22.E-04	5.019	1.28.E-04	5.008	1.28.E-04	4.993	1.28.E-04	4.988	1.39.E-05	5.507
81 × 1	4.74.E-04	5.041	6.64.E-05	5.002	6.63.E-05	4.994	6.63.E-05	4.991	6.79.E-06	5.439
121 × 1	6.22.E-05	5.062	8.93.E-06	4.999	8.93.E-06	4.996	8.93.E-06	4.995	8.02.E-07	5.322
161 × 1	1.45.E-05	5.093	2.14.E-06	4.998	2.14.E-06	4.997	2.14.E-06	4.997	1.82.E-07	5.193
241 × 1	1.80.E-06	5.170	2.85.E-07	4.999	2.85.E-07	4.999	2.85.E-07	4.999	2.32.E-08	5.107

Table B3 Error and global-order-of-accuracy of subsonic gaussian pulse advection problem (1D)

Subsonic gaussian pulse advection problem $\left[q = 0.05\exp\left(-(\ln 2)\left(\frac{x}{30}\right)^2\right)\right],\ a_{SCL} = 0.1$										
Grids	WENO-JS		WENO-M		WENO-Z		eMLP		eMLP-VC	
	L_2 error	order	L_2 error	order	L_2 error	order	L_2 error	order	L_2 error	order
11 × 1	1.29.E-02		1.24.E-02		1.24.E-02		1.20.E-02		1.21.E-02	
13 × 1	1.19.E-02	0.496	1.14.E-02	0.490	1.14.E-02	0.493	1.10.E-02	0.520	1.08.E-02	0.702
15 × 1	1.09.E-02	0.580	1.05.E-02	0.607	1.04.E-02	0.611	1.00.E-02	0.607	1.01.E-02	0.462
17 × 1	1.01.E-02	0.658	9.59.E-03	0.696	9.56.E-03	0.702	9.17.E-03	0.736	8.96.E-03	0.948
19 × 1	9.28.E-03	0.727	8.77.E-03	0.803	8.74.E-03	0.810	8.33.E-03	0.854	8.30.E-03	0.688
21 × 1	8.60.E-03	0.760	8.04.E-03	0.860	8.01.E-03	0.869	7.59.E-03	0.936	7.48.E-03	1.044
25 × 1	7.56.E-03	0.741	6.90.E-03	0.883	6.85.E-03	0.893	6.42.E-03	0.963	6.33.E-03	0.954
29 × 1	6.83.E-03	0.683	6.06.E-03	0.868	6.02.E-03	0.880	5.55.E-03	0.978	5.45.E-03	1.008
33 × 1	6.25.E-03	0.681	5.39.E-03	0.910	5.34.E-03	0.920	4.90.E-03	0.961	4.90.E-03	0.824
37 × 1	5.74.E-03	0.753	4.79.E-03	1.038	4.74.E-03	1.047	4.31.E-03	1.115	4.37.E-03	0.990
41 × 1	5.24.E-03	0.876	4.22.E-03	1.222	4.18.E-03	1.229	3.79.E-03	1.264	3.89.E-03	1.137
51 × 1	4.08.E-03	1.147	2.96.E-03	1.629	2.92.E-03	1.633	2.66.E-03	1.623	2.83.E-03	1.463
61 × 1	3.08.E-03	1.581	1.95.E-03	2.323	1.89.E-03	2.436	1.81.E-03	2.158	1.83.E-03	2.435

71 × 1	2.25.E-03	2.059	1.25.E-03	2.940	1.15.E-03	3.250	1.27.E-03	2.300	1.13.E-03	3.177
81 × 1	1.61.E-03	2.531	8.20.E-04	3.198	7.14.E-04	3.652	8.95.E-04	2.684	6.83.E-04	3.817
121 × 1	4.50.E-04	3.179	2.32.E-04	3.144	2.21.E-04	2.917	2.25.E-04	3.442	9.48.E-05	4.920
161 × 1	1.68.E-04	3.456	6.78.E-05	4.310	6.69.E-05	4.189	6.61.E-05	4.287	1.86.E-05	5.700
241 × 1	3.15.E-05	4.146	9.80.E-06	4.793	9.77.E-06	4.770	9.74.E-06	4.746	1.74.E-06	5.875

Table B4 Error and global-order-of-accuracy of supersonic gaussian pulse advection problem (1D)

Supersonic gaussian pulse advection problem $\left[q = 0.05\exp\left(-(\ln 2)\left(\frac{x}{30}\right)^2\right)\right]$, $a_{SCL} = 1.0$										
Grids	WENO-JS		WENO-M		WENO-Z		eMLP		eMLP-VC	
	L_2 error	order	L_2 error	order	L_2 error	order	L_2 error	order	L_2 error	order
11 × 1	1.35.E-02		1.24.E-02		1.24.E-02		1.20.E-02		1.18.E-02	
13 × 1	1.25.E-02	0.459	1.14.E-02	0.490	1.14.E-02	0.493	1.10.E-02	0.520	1.08.E-02	0.523
15 × 1	1.15.E-02	0.541	1.05.E-02	0.607	1.04.E-02	0.611	1.01.E-02	0.607	9.95.E-03	0.606
17 × 1	1.07.E-02	0.613	9.59.E-03	0.696	9.56.E-03	0.702	9.17.E-03	0.736	9.06.E-03	0.745
19 × 1	9.98.E-03	0.621	8.77.E-03	0.803	8.74.E-03	0.810	8.34.E-03	0.853	8.23.E-03	0.869
21 × 1	9.42.E-03	0.582	8.04.E-03	0.860	8.01.E-03	0.869	7.59.E-03	0.937	7.47.E-03	0.958

25 × 1	8.60.E-03	0.518	6.90.E-03	0.883	6.85.E-03	0.893	6.42.E-03	0.962	6.31.E-03	0.969
29 × 1	8.09.E-03	0.413	6.06.E-03	0.868	6.02.E-03	0.880	5.55.E-03	0.976	5.42.E-03	1.020
33 × 1	7.71.E-03	0.375	5.39.E-03	0.910	5.34.E-03	0.920	4.90.E-03	0.963	4.74.E-03	1.044
37 × 1	7.37.E-03	0.393	4.79.E-03	1.038	4.74.E-03	1.047	4.32.E-03	1.111	4.18.E-03	1.108
41 × 1	7.04.E-03	0.444	4.22.E-03	1.222	4.18.E-03	1.229	3.79.E-03	1.262	3.62.E-03	1.381
51 × 1	6.24.E-03	0.556	2.96.E-03	1.628	2.93.E-03	1.633	2.66.E-03	1.622	2.54.E-03	1.631
61 × 1	5.47.E-03	0.736	1.95.E-03	2.322	1.89.E-03	2.435	1.81.E-03	2.163	1.81.E-03	1.897
71 × 1	4.74.E-03	0.941	1.25.E-03	2.937	1.16.E-03	3.247	1.27.E-03	2.297	1.27.E-03	2.298
81 × 1	4.06.E-03	1.174	8.21.E-04	3.192	7.15.E-04	3.645	8.96.E-04	2.680	8.96.E-04	2.680
121 × 1	1.97.E-03	1.802	2.34.E-04	3.129	2.23.E-04	2.901	2.27.E-04	3.425	2.27.E-04	3.425
161 × 1	8.75.E-04	2.840	6.99.E-05	4.227	6.91.E-05	4.106	6.82.E-05	4.202	6.82.E-05	4.202
241 × 1	2.34.E-04	3.266	9.81.E-06	4.870	9.77.E-06	4.847	9.74.E-06	4.825	9.74.E-06	4.825

Table B5 Error and global-order-of-accuracy of isentropic vortex advection problem (2D)

Isentropic vortex advection problem ($M_\infty = 0.25$)										
Grids	WENO-JS		WENO-M		WENO-Z		eMLP		eMLP-VC	
	L_2 error	order	L_2 error	order	L_2 error	order	L_2 error	order	L_2 error	order

11 × 1	1.98.E-02		1.87.E-02		1.90.E-02		1.98.E-02		1.66.E-02	
13 × 1	1.80.E-02	0.567	1.60.E-02	0.935	1.68.E-02	0.754	1.83.E-02	0.464	1.29.E-02	1.497
15 × 1	1.63.E-02	0.704	1.37.E-02	1.072	1.44.E-02	1.063	1.65.E-02	0.739	1.12.E-02	1.000
17 × 1	1.45.E-02	0.933	1.14.E-02	1.479	1.22.E-02	1.346	1.45.E-02	1.013	7.64.E-03	3.069
19 × 1	1.30.E-02	1.003	9.23.E-03	1.910	1.00.E-02	1.718	1.27.E-02	1.186	6.37.E-03	1.637
21 × 1	1.12.E-02	1.449	7.20.E-03	2.479	8.04.E-03	2.219	1.07.E-02	1.727	2.27.E-03	10.292
25 × 1	7.75.E-03	2.122	4.18.E-03	3.119	4.53.E-03	3.295	7.39.E-03	2.118	6.25.E-04	7.406
29 × 1	4.97.E-03	2.993	1.99.E-03	5.001	2.17.E-03	4.964	3.72.E-03	4.628	2.38.E-04	6.511
33 × 1	3.30.E-03	3.178	1.29.E-03	3.334	1.31.E-03	3.889	2.37.E-03	3.497	1.08.E-04	6.126
37 × 1	2.12.E-03	3.848	8.00.E-04	4.193	8.09.E-04	4.224	1.36.E-03	4.830	5.80.E-05	5.418
41 × 1	1.37.E-03	4.256	4.47.E-04	5.681	4.58.E-04	5.541	7.19.E-04	6.219	3.40.E-05	5.206
51 × 1	5.30.E-04	4.362	1.31.E-04	5.616	1.46.E-04	5.252	3.23.E-04	3.671	1.08.E-05	5.270
61 × 1	2.18.E-04	4.950	4.84.E-05	5.563	5.01.E-05	5.953	4.70.E-05	10.760	4.12.E-06	5.362
71 × 1	9.97.E-05	5.161	2.26.E-05	5.006	2.14.E-05	5.601	2.28.E-05	4.761	1.84.E-06	5.300
81 × 1	5.03.E-05	5.188	1.22.E-05	4.697	1.13.E-05	4.855	1.21.E-05	4.814	9.21.E-07	5.261
121 × 1	6.51.E-06	5.097	1.67.E-06	4.951	1.66.E-06	4.775	1.66.E-06	4.948	1.16.E-07	5.157
161 × 1	1.52.E-06	5.085	3.98.E-07	5.024	3.98.E-07	5.006	3.98.E-07	5.007	2.97.E-08	4.772

References

[1] Holden, J., and Goel, N. *Fast-Forwarding to a Future of On-Demand Urban Air Transportation*. San Francisco, CA, 2016.

[2] "eVTOL Aircraft Directory," Electric VTOL News™ by the Vertical Flight Society, https://evtol.news/aircraft/

[3] "OPPAV, Optionally Piloted Personal Air Vehicle Technology Demonstrator," Korea Aerospace Research Institute, https://www.kari.re.kr/eng/sub03_01_01.do.

[4] Leishman, J. G. *Principles of Helicopter Aerodynamics*. New York, 2000.

[5] Lele, S. K. "Compact Finite Difference Schemes with Spectral-like Resolution." *Journal of Computational Physics*, Vol. 103, No. 1, 1992, pp. 16–42. https://doi.org/10.1016/0021-9991(92)90324-R.

[6] Tam, C. K. W., and Webb, J. C. Dispersion-Relation-Preserving Finite Difference Schemes for Computational Acoustics. *Journal of Computational Physics*. Vol. 107, pp. 262–281.

[7] G.S.Jiang, and C.W. Shu. "Efficient Implementation of Weighted ENO Schemes." *Journal of Computational Physics*, Vol. 126, No. 126, 1996, pp. 202–228. https://doi.org/10.1006/jcph.1996.0130.

[8] Pulliam, T. H. "High Order Accurate Finite-Difference Methods: As Seen in OVERFLOW." *20th AIAA Computational Fluid Dynamics Conference 2011*, 2011, pp. 1–14. https://doi.org/10.2514/6.2011-3851.

[9] Sweby, P. K. "High Resolution Schemes Using Flux Limiters for Hyperbolic Conservation Laws." *SIAM Journal on Numerical Analysis*, Vol. 21, No. 5, 1984, pp. 995–1011. https://doi.org/10.1137/0721062.

[10] Kim, K. H., and Kim, C. "Accurate, Efficient and Monotonic Numerical Methods for Multi-Dimensional Compressible Flows. Part II: Multi-Dimensional Limiting Process." *Journal of Computational Physics*, Vol. 208, No. 2, 2005, pp. 570–615. https://doi.org/10.1016/j.jcp.2005.02.022.

[11] Visbal, M. R., and Rizzetta, D. P. "Large-Eddy Simulation on Curvilinear Grids Using Compact Differencing and Filtering Schemes." *Journal of*

Fluids Engineering, Vol. 124, No. 4, 2002, pp. 836–847. https://doi.org/10.1115/1.1517564.

[12] Deng, X., and Zhang, H. "Developing High-Order Weighted Compact Nonlinear Schemes." *Journal of Computational Physics*, Vol. 165, No. 1, 2000, pp. 22–44. https://doi.org/10.1006/jcph.2000.6594.

[13] Martín, M. P., Taylor, E. M., Wu, M., and Weirs, V. G. "A Bandwidth-Optimized WENO Scheme for the Effective Direct Numerical Simulation of Compressible Turbulence." *Journal of Computational Physics*, Vol. 220, No. 1, 2006, pp. 270–289. https://doi.org/10.1016/j.jcp.2006.05.009.

[14] Kim, S., Lee, S., and Kim, K. H. "Wavenumber-Extended High-Order Oscillation Control Finite Volume Schemes for Multi-Dimensional Aeroacoustic Computations." *Journal of Computational Physics*, Vol. 227, No. 8, 2008, pp. 4089–4122. https://doi.org/10.1016/j.jcp.2007.12.013.

[15] Jameson, A. "Origins and Further Development of the Jameson-Schmidt-Turkel Scheme." *AIAA Journal*, Vol. 55, No. 5, 2017, pp. 1487–1510. https://doi.org/10.2514/1.J055493.

[16] Henrick, A. K., Aslam, T. D., and Powers, J. M. "Mapped Weighted Essentially Non-Oscillatory Schemes: Achieving Optimal Order near Critical Points." *Journal of Computational Physics*, Vol. 207, No. 2, 2005, pp. 542–567. https://doi.org/10.1016/j.jcp.2005.01.023.

[17] Borges, R., Carmona, M., Costa, B., and Don, W. S. "An Improved Weighted Essentially Non-Oscillatory Scheme for Hyperbolic Conservation Laws." *Journal of Computational Physics*, Vol. 227, No. 6, 2008, pp. 3191–3211. https://doi.org/10.1016/j.jcp.2007.11.038.

[18] Park, S. H., Kwon, O. J., and Lee, S. "Improved High-Order High-Resolution Energy Stable Weighted Essentially Non-Oscillatory plus Scheme for Shock/Vortex Problems." *AIP Advances*, Vol. 12, No. 4, 2022. https://doi.org/10.1063/5.0083675.

[19] Kang, H. M., Kim, K. H., and Lee, D. H. "A New Approach of a Limiting Process for Multi-Dimensional Flows." *Journal of Computational Physics*, Vol. 229, No. 19, 2010, pp. 7102–7128. https://doi.org/10.1016/j.jcp.2010.06.001.

[20] Hong, Y., Lee, D., Yee, K., and Park, S. H. "Enhanced High-Order Scheme for High-Resolution Rotorcraft Flowfield Analysis." *AIAA Journal*, Vol. 60, No. 1, 2022, pp. 144–159. https://doi.org/10.2514/1.J060803.

[21] Houim, R. W., and Kuo, K. K. "A Low-Dissipation and Time-Accurate Method for Compressible Multi-Component Flow with Variable Specific Heat Ratios." *Journal of Computational Physics*, Vol. 230, No. 23, 2011, pp. 8527–8553. https://doi.org/10.1016/j.jcp.2011.07.031.

[22] Ko, J., and Lee, S. "Numerical Investigation of Inter-Rotor Spacing Effects on Wake Dynamics of Coaxial Rotors." *Journal of Aircraft*, Vol. 58, No. 2, 2021, pp. 363–373. https://doi.org/10.2514/1.C035857.

[23] Choi, J. Y., Unnikrishnan, U., Hwang, W. S., Jeong, S. M., Han, S. H., Kim, K. H., and Yang, V. "Effect of Fuel Temperature on Flame Characteristics of Supersonic Turbulent Combustion." *Fuel*, Vol. 329, 2022, 125310. https://doi.org/10.1016/j.fuel.2022.125310.

[24] Boyd, D. D. "HART-II Acoustic Predictions Using a Coupled CFD/CSD Method." *American Helicopter Society 65th Annual Forum Proceedings,* 2009.

[25] Jia, Z., Lee, S., Sharma, K., and Brentner, K. S. "Effect of Pitch Attitude on the Performance and Acoustics of a Lift-Offset Coaxial Rotor Based on High-Fidelity CFD/CSD Simulations." *The Vertical Flight Society - Forum 75: The Future of Vertical Flight - Proceedings of the 75th Annual Forum and Technology Display*, 2019.

[26] Jia, Z., and Lee, S. "Aeroacoustic Analysis of a Side-by-Side Hybrid VTOL Aircraft." *Vertical Flight Society's 76th Annual Forum and Technology Display,* 2020.

[27] Chaderjian, N. M. "Quantitative Approach for the Accurate CFD Simulation of Hover in Turbulent Flow." *International Conference on Computational Fluid Dynamics (ICCFD11),* Maui, Hawaii, 2022.

[28] Smith, M. J., Lim, J. W., van der Wall, B. G., Baeder, J. D., Biedron, R. T., Boyd, D. D., Jayaraman, B., Jung, S. N., and Min, B.-Y. "The HART II International Workshop: An Assessment of the State of the Art in CFD/CSD Prediction." *CEAS Aeronautical Journal,* Vol. 4, No. 4, 2013, pp. 345–372. https://doi.org/10.1007/s13272-013-0078-8.

[29] Pirozzoli, S. "On the Spectral Properties of Shock-Capturing Schemes." *Journal of Computational Physics,* Vol. 219, No. 2, 2006, pp. 489–497. https://doi.org/10.1016/j.jcp.2006.07.009.

[30] Lozano-Durán, A., and Bae, H. J. "Error Scaling of Large-Eddy Simulation in the Outer Region of Wall-Bounded Turbulence." *Journal of Computational Physics,* Vol. 392, 2019, pp. 532–555. https://doi.org/10.1016/j.jcp.2019.04.063.

[31] Brown, R. E. "Rotor Wake Modeling for Flight Dynamic Simulation of Helicopters." *AIAA journal,* Vol. 38, No. 1, 2000, pp. 57–63. https://doi.org/10.2514/2.922.

[32] Brown, R. E., and Line, A. J. "Efficient High-Resolution Wake Modeling Using the Vorticity Transport Equation." *AIAA Journal,* Vol. 43, No. 7, 2005, pp. 1434–1443. https://doi.org/10.2514/1.13679.

[33] Caros, L., Buxton, O., Shigeta, T., Nagata, T., Nonomura, T., Asai, K., and Vincent, P. "Direct Numerical Simulation of Flow over a Triangular Airfoil Under Martian Conditions." *AIAA Journal,* Vol. 60, No. 7, 2022, pp. 3961–3972. https://doi.org/10.2514/1.J061454.

[34] Koch, R., Sanjosé, M., and Moreau, S. "Large-Eddy Simulation and Acoustic Prediction of a Helicopter Rotor in Hover." *28th AIAA/CEAS Aeroacoustics Conference,* 2022, pp. 1–17. https://doi.org/10.2514/6.2022-2915.

[35] Cho, K. W., Kwon, J. H., and Lee, S. "Development of a Fully Systemized Chimera Methodology for Steady/Unsteady Problems." *Journal of Aircraft,* Vol. 36, No. 6, 1999, pp. 973–980. https://doi.org/10.2514/2.2538.

[36] Hong, Y., Park, S. H., and Yee, K. "Comparative Assessment of Local Accuracy of High-Order Spatial Schemes for Rotorcraft Aeroacoustics." *AIAA Journal,* Vol. 61, No. 1, 2023, pp. 355–377. https://doi.org/10.2514/1.J062008.

[37] Seo, Y., Hong, Y., and Yee, K. "Numerical Investigation of Wing–Multiple Propeller Aerodynamic Interaction Using Actuator Disk Method." *International Journal of Aeronautical and Space Sciences*, Vol. 23, 2022, pp. 805-822, https://doi.org/10.1007/s42405-022-00446-7.

[38] Kwon, S., Hong, Y., Kang, Y. E., and Yee, K. "An Improved Reduced Order Model for Prediction of Rotor Aerodynamic Force and Noise." *AIAA AVIATION 2022 Forum*, 2022, pp. 1–16. https://doi.org/10.2514/6.2022-3489.

[39] Shon, S., Kang, Y.-E., Hong, Y., Yee, K., and Myong, R. S. "Design of Hybrid Airfoils for Icing Tunnel Tests Based on Reduced-Order Modeling Methods." *Journal of Aircraft*, Vol. 59, No. 4, 2022, pp. 847–860. https://doi.org/10.2514/1.C036435.

[40] Yang, S., and Yee, K. "Design Rule Extraction Using Multi-Fidelity Surrogate Model for Unmanned Combat Aerial Vehicles." *Journal of Aircraft*, Vol. 59, No. 4, 2022, pp. 977–991. https://doi.org/10.2514/1.C036489.

[41] Sa, J. H., You, Y. H., Park, J. S., Jung, S. N., Park, S. H., and Yu, Y. H. "Assessment of CFD/CSD Coupled Aeroelastic Analysis Solution for HART II Rotor Incorporating Fuselage Effects." *American Helicopter Society 67th Annual Forum Proceedings*, 2011, pp. 736–748.

[42] Blazek, J. *Computational Fluid Dynamics: Principles and Applications*. Elsevier, New York, 2001.

[43] Jain, R. "CFD Hover Performance and Transition Predictions on the PSP and HVAB Rotors Using CREATETM-AV Helios." *AIAA Science and Technology Forum and Exposition, AIAA SciTech Forum 2022*, 2022, pp. 1–27. https://doi.org/10.2514/6.2022-1549.

[44] Spalart, P. R., and Allmaras, S. R. "One-Equation Turbulence Model for Aerodynamic Flows." AIAA Paper 1992-0439, 1992. https://doi.org/10.2514/6.1992-439.

[45] Wilcox, D. C. "Reassessment of the Scale-Determining Equation for Advanced Turbulence Models." *AIAA Journal*, Vol. 26, No. 11, 1988, pp. 1299–1310. https://doi.org/10.2514/3.10041.

[46] Park, S. H., and Kwon, J. H. "Implementation of K-ω Turbulence Models in an Implicit Multigrid Method." *AIAA Journal*, Vol. 42, No. 7, 2004, pp. 1348–1357. https://doi.org/10.2514/1.2461.

[47] Nichols, R. H., Tramel, R. W., and Buning, P. G. "Evaluation of Two High-Order Weighted Essentially Nonoscillatory Schemes." *AIAA Journal*, Vol. 46, No. 12, 2008, pp. 3090–3102. https://doi.org/10.2514/1.36849.

[48] Kim, K. H., Kim, C., and Rho, O. H. "Methods for the Accurate Computations of Hypersonic Flows. I. AUSMPW+ Scheme." *Journal of Computational Physics*, Vol. 174, No. 1, 2001, pp. 38–80. https://doi.org/10.1006/jcph.2001.6873.

[49] Kennedy, C. A., and Carpenter, M. H. "Diagonally Implicit Runge-Kutta Methods for Ordinary Differential Equations. A Review." NASA Langley Research Center, NASA TM-2016-219173, Hampton, VA, 2016.

[50] Pulliam, T. H., and Chaussee, D. S. "A Diagonal Form of an Implicit Approximate-Factorization Algorithm." *Journal of Computational Physics*, Vol. 39, No. 2, 1981, pp. 347–363. https://doi.org/10.1016/0021-9991(81)90156-X.

[51] Yoon, S. H., Kim, C., and Kim, K. H. "Multi-Dimensional Limiting Process for Three-Dimensional Flow Physics Analyses." *Journal of Computational Physics*, Vol. 227, No. 12, 2008, pp. 6001–6043. https://doi.org/10.1016/j.jcp.2008.02.012.

[52] Norman, M. L., and Winkler, K.-H. A. "Supersonic Jets." *Los Alamos Sci.*, No. 12, 1985, pp. 38-71.

[53] Park, J. S., Yoon, S. H., and Kim, C. "Multi-Dimensional Limiting Process for Hyperbolic Conservation Laws on Unstructured Grids." *Journal of Computational Physics*, Vol. 229, No. 3, 2010, pp. 788–812. https://doi.org/10.1016/j.jcp.2009.10.011.

[54] Kim, K. H., and Kim, C. "Accurate, Efficient and Monotonic Numerical Methods for Multi-Dimensional Compressible Flows. Part I: Spatial Discretization." *Journal of Computational Physics*, Vol. 208, No. 2, 2005, pp. 527–569. https://doi.org/10.1016/j.jcp.2005.02.021.

[55] P. L. Roe. "Approximate Riemann Solvers, Parameter Vectors, and Difference Schemes." *Journal of Computational Physics*, Vol. 43, 1981, pp. 357–372. https://doi.org/10.1016/0021-9991(81)90128-5.

[56] Park, S. H., and Kwon, J. H. “On the Dissipation Mechanism of Godunov-Type Schemes.” *Journal of Computational Physics*, Vol. 188, No. 2, 2003, pp. 524–542. https://doi.org/10.1016/S0021-9991(03)00191-8.

[57] Kemm, F. “On the Proper Setup of the Double Mach Reflection as a Test Case for the Resolution of Gas Dynamics Codes.” *Computers and Fluids*, Vol. 132, 2016, pp. 72–75. https://doi.org/10.1016/j.compfluid.2016.04.008.

[58] Vichnevetsky, R., and Bowles, J. B. *Fourier Analysis of Numerical Approximations of Hyperbolic Equations*, Soc. for Applied and Industrial Mathematics, Philadelphia, PA, 1982, Chap. 8.

[59] Hardin, J. C., Ristorcelli, J. R., and Tam, C. K., “ICASE/LaRC Work- shop on Benchmark Problems in Computational Aeroacoustics,”NASA CP-3300, 1995.

[60] Tavelli, M., and Dumbser, M. “A Pressure-Based Semi-Implicit Space–Time Discontinuous Galerkin Method on Staggered Unstructured Meshes for the Solution of the Compressible Navier–Stokes Equations at All Mach Numbers.” *Journal of Computational Physics*, Vol. 341, 2017, pp. 341–376. https://doi.org/10.1016/j.jcp.2017.03.030.

[61] Feng, Y., Boivin, P., Jacob, J., and Sagaut, P. “Hybrid Recursive Regularized Thermal Lattice Boltzmann Model for High Subsonic Compressible Flows.” *Journal of Computational Physics*, Vol. 394, 2019, pp. 82–99. https://doi.org/10.1016/j.jcp.2019.05.031.

[62] Veldhuis, L. L. M., “Propeller Wing Aerodynamic Interference,” Ph.D. Dissertation, Faculty of Aerospace Engineering, Delft Univ. of Technology, Delft, The Netherlands, 2005.

[63] Hartman, E. P., and Biermann, D., “The Aerodynamic Characteristics of Full-Scale Propellers Having 2, 3 and 4 Blades of Clark Yand R.A.F 6 Airfoil Sections,” NACA TR 640, 1938.

[64] Dong, X., Gao, Y., and Liu, C. “New Normalized Rortex/Vortex Identification Method.” *Physics of Fluids*, Vol. 31, No. 1, 2019. https://doi.org/10.1063/1.5066016.

[65] Liu, C., Gao, Y., Tian, S., and Dong, X. “Rortex - A New Vortex Vector Definition and Vorticity Tensor and Vector Decompositions.” *Physics of Fluids*, Vol. 30, No. 3, 2018. https://doi.org/10.1063/1.5023001.

[66] Johnson, W., “Technology Drivers in the Development of CAMRAD II,” Proceedings oftheAmericanHelicopterSocietyAeromechanicsSpecialist Meeting, American Helicopter Soc., Alexandria, VA, Jan. 1994.

[67] Wie, S.-Y., Kang, H. J., Kim, T., Kee, Y.-J., and Song, J. “High-Efficiency Propeller Development for Multicopter Type UAV.” *Journal of the Korean Society for Aeronautical & Space Sciences*, Vol. 45, No. 7, 2017, pp. 581–593. https://doi.org/10.5139/jksas.2017.45.7.581.

[68] Farassat, F. *Derivation of Formulations 1 and 1A of Farassat*. NASA TM 2007-214853, 2007.

[69] Chaderjian, N. M. “Navier-Stokes Simulation of UH-60A Rotor/Wake Interaction Using Adaptive Mesh Refinement.” *Annual Forum Proceedings - AHS International*, 2017, pp. 556–575.

[70] Biedron, R. T., and Lee-Rausche, E. M. “Rotor Airloads Prediction Using Unstructured Meshes and Loose CFD/CSD Coupling.” *AIAA Applied Aerodynamics Conference*, 2008, pp. 1–18. https://doi.org/10.2514/6.2008-7341.

[71] Tinney, C. E., and Valdez, J. “Thrust and Acoustic Performance of Small-Scale, Coaxial, Corotating Rotors in Hover.” *AIAA Journal*, Vol. 58, No. 4, 2020, pp. 1657–1667. https://doi.org/10.2514/1.J058489.

[72] Valdez, J. A., and Tinney, C. E. “Wake of a Coaxial Corotating Rotor in Hover.” *AIAA Journal*, Vol. 60, No. 8, 2022, pp. 4829–4839. https://doi.org/10.2514/1.J061651.

[73] Uehara, D., and Sirohi, J. “Quantification of Swirl Recovery in a Coaxial Rotor System.” *Annual Forum Proceedings - AHS International*, No. May 2017, pp. 2828–2840.

[74] Uehara, D., Sirohi, J., and Bhagwat, M. J. “Hover Performance of Corotating and Counterrotating Coaxial Rotors.” *Journal of the American Helicopter Society*, Vol. 65, No. 1, 2020, pp. 1–8. https://doi.org/10.4050/JAHS.65.012006.

[75] Rubio, R. C., Diaz, P. V., and Yoon, S. “High-Fidelity Computational Analysis of Ducted and Coaxial Rotors for Urban Air Mobility.” *The Vertical Flight Society - Forum 75: The Future of Vertical Flight - Proceedings of the 75th Annual Forum and Technology Display*, 2019.

[76] Whiteside, S. K. S., Zawodny, N. S., Fei, X., Pettingill, N. A., Patterson, M. D., and Rothhaar, M., “An Exploration of the Performance and Acoustic Characteristics of UAV-Scale Stacked Rotor Configurations,” AIAA Paper 2019-1071, 2019.

[77] Jung, Y. S., Baeder, J., and He, C. “Investigation of Empirical Rotor Broadband Prediction Using CFD Boundary Layer Parameters Extraction.” *77th Annual Vertical Flight Society Forum and Technology Display, FORUM 2021: The Future of Vertical Flight*, 2021. https://doi.org/10.4050/f-0077-2021-16692.

[78] Spalart, P. R., Deck, S., Shur, M. L., Squires, K. D., Strelets, M. K., and Travin, A. “A New Version of Detached-Eddy Simulation, Resistant to Ambiguous Grid Densities.” *Theoretical and Computational Fluid Dynamics*, Vol. 20, No. 3, 2006, pp. 181–195. https://doi.org/10.1007/s00162-006-0015-0.

[79] Huh, J. Y., and Kim, K. H. "Development of Low Diffusive Mlp Limiter for Meshless Method." *AIAA Aviation 2019 Forum*, 2019. https://doi.org/10.2514/6.2019-3637.

[80] Rumsey, C. L., Slotnick, J. P., and Woeber, C. D. “Hlpw-4/Gmgw-3: Overview and Workshop Summary.” *AIAA Aviation 2022 Forum*, 2022, https://doi.org/10.2514/6.2022-3295.

[81] Blom, D. S., Birken, P., Bijl, H., Kessels, F., Meister, A., and van Zuijlen, A. H. “A Comparison of Rosenbrock and ESDIRK Methods Combined with Iterative Solvers for Unsteady Compressible Flows.” *Advances in Computational Mathematics*, Vol. 42, No. 6, 2016, pp. 1401–1426. https://doi.org/10.1007/s10444-016-9468-x.

[82] Coder, J. G. “OVERFLOW Rotor Hover Simulations Using Advanced Turbulence and Transition Modeling.” *AIAA SciTech Forum - 55th AIAA Aerospace Sciences Meeting*, January, 2017, https://doi.org/10.2514/6.2017-1432.

[83] Öhrle, C., Frey, F., Thiemeier, J., Keßler, M., Krämer, E., Embacher, M., Cranga, P., and Eglin, P. “Compound Helicopter X3 in High-Speed Flight: Correlation of Simulation and Flight Test.” *Vertical Flight Society - Forum*

75: The Future of Vertical Flight, 2019, pp. 1–14. https://doi.org/10.4050/jahs.66.012011.

[84] Acker, F., Borges, R. B. R., and Costa, B. “An Improved WENO-Z Scheme.” *Journal of Computational Physics*, Vol. 313, 2016, pp. 726–753. https://doi.org/10.1016/j.jcp.2016.01.038.

[85] Castro, M., Costa, B., and Don, W. S. “High Order Weighted Essentially Non-Oscillatory WENO-Z Schemes for Hyperbolic Conservation Laws.” *Journal of Computational Physics*, Vol. 230, No. 5, 2011, pp. 1766–1792. https://doi.org/10.1016/j.jcp.2010.11.028.

[86] Yamaleev, N. K., and Carpenter, M. H. “Third-Order Energy Stable WENO Scheme.” *Journal of Computational Physics*, Vol. 228, No. 8, 2009, pp. 3025–3047. https://doi.org/10.1016/j.jcp.2009.01.011.

국문 초록

도심항공교통을 위한 새로운 컨셉의 수직 이착륙기에 대한 연구가 증가하며, 새로운 형상에 대한 정확한 공력 및 공력 소음 성능 해석에 대한 수요가 증가하고 있다. 기존에 제시되었던 여러 컨셉의 고차 정확도 공간 차분법은 비교적 간단한 형태의 헬리콥터 성능 해석에 활용된 바 있으며, 많은 수의 격자가 동반될 때 만족할 만한 수준의 결과를 낸 바 있다. 그러나 다중 로터를 공통적으로 사용하는 새로운 컨셉의 수직 이착륙기는 기존에 헬리콥터 해석에 사용되던 격자 수준의 몇 배를 필요로 하기 때문에, 공간 차분법의 해석 정확도를 더욱 높게 개발할 필요가 있다.

본 연구에서는 기존의 고차 정확도 스킴인 eMLP 를 수직 이착륙기 유동장 특징에 맞춰 개선하였다. 비정상적인 와류가 지배적이며, 아음속부터 초음속까지 전 마하수를 아우르는 유속의 존재 등을 고려하여 정확도와 강건성, 그리고 효율성을 개선한 eMLP-VC 를 제시하였다. 일, 이차원의 벤치마크 테스트를 통해 새롭게 제시된 eMLP-VC 의 우수성을 보였으며, 특히 로터 유동장 뿐만 아니라 극초음속의 충각파가 지배적인 유동에서도 강건함을 유지하는 것을 보였다.

개발된 eMLP-VC 와 타 고차 정확도 스킴의 정량적인 비교를 위해 새로운 국부 공간 정확도 지수인 local-order-of-accuracy index (LAI)를 제시하였다. 압축성 유동에서 사용되는 고차 정확도 스킴들이 아음속의 연속성을 갖는 유동에서 정확도가 감소되기 때문에, 스킴의

정확도 차이가 생긴다. 차분된 공간에서 국부적으로 감소되는 정확도가 결과적으로 유동 해석 충실도를 감소시키기 때문에, 이를 분석하여 정확도 감소를 최소화할 필요가 있다. 본 연구에서 새롭게 제시된 LAI 은 외재적으로 보간하는 모든 공간 차분 방법에 대해 적용할 수 있으며, 이를 통해 유동장의 어떤 부분에서 정확도 감소가 일어나는 지 확인할 수 있다. 일, 이차원 벤치마크 테스트를 통해, 본 연구에서 제시한 스킴을 포함한 여러 고차 정확도 스킴들을 비교하였고, 결과적으로 수직 이착륙기 고정확도 해석에 있어 반드시 필요한 수치적 특성을 밝혀낼 수 있었다. 우선, 적은 격자 수준에서 와류가 충격파와 비슷한 수치적 특성을 보이기 때문에, 이를 충격파로 잘못 인지하여 수치 소산을 가하지 않아야 한다. 즉, 이를 위해 충격파 센싱 기법이 고도화되어야 할 필요가 있다. 두번째로, 아음속 영역에서 중앙 차분을 이용함으로써 풍상 차분법의 낮은 정확도를 보완할 필요가 있다. 초음속 영역에서는 강건한 풍상 차분법을 유지하고, 아음속 영역에서는 정확도가 높은 중앙 차분을 혼합하여 이용함으로써, 해석자의 정확도와 강건성을 모두 보장할 수 있다.

마지막으로 세 가지 수직 이착륙기 유동장에 eMLP-VC 를 이용하여 해석을 진행하고, 최적 설계를 고정밀도 해석자를 이용하여 진행함으로써, 새로운 형상의 수직 이착륙기 개발에 본 연구에서 제시된 스킴이 충분히 활용될 수 있음을 보였다. PROWIM 모델과 HART-II 로터에서 적은 격자를 가지고도 충분히 와류를 보존하고 와류의 비정상적인 거동을 포착할 수 있음을 보였다. 특히, HART-II 로터에서 발생하는 공력 소음까지도 정확한 수준으로 예측할 수 있음을 보였다. 실제 도심항공교통 수직 이착륙기에 적용 가능한 적층 로터

형상 최적 설계에도 활용하였다. 최적 설계된 형상에 대해 초정밀 해석을 진행하고, 이를 통해 최적 설계가 제대로 이루어졌음을 확인하였다. 결과적으로 개발된 스킴, eMLP-VC 가 성공적으로 수직 이착륙기 개발에 사용될 수 있음을 확인하였다.

주요어: 고차 정확도 공간 차분법, 국부 공간 정확도 지수, 수직 이착륙기, 공력 간섭 현상, 공력 소음, 최적 설계, 도심항공교통

학번: 2019-31839

성명: 홍윤표